Crystalline topological phases

From corner charge to hinge state

Sander Kooi

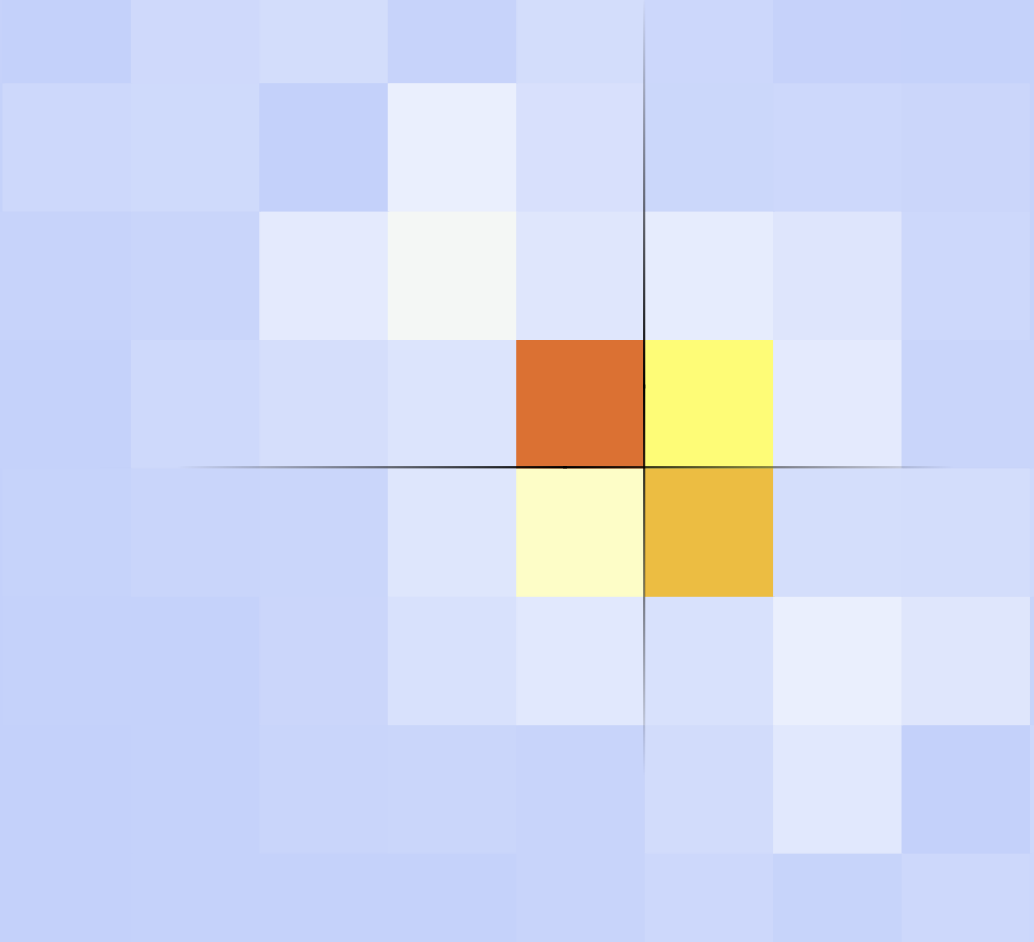

Crystalline topological phases: From corner charge to hinge state

S.H. Kooi

PhD thesis, Utrecht University, July 2020

ISBN: 978-94-6380-881-1

DOI: 10.33540/70

Crystalline topological phases: From corner charge to hinge state

Kristallijne topologische fases: Van hoeklading tot ribbe toestand

(met een samenvatting in het Nederlands)

Proefschrift

ter verkrijging van de graad van doctor aan de Universiteit Utrecht op gezag van de rector magnificus, prof. dr. H.R.B.M. Kummeling, ingevolge het besluit van het college voor promoties in het openbaar te verdedigen op woensdag 2 september 2020 des middags te 2.30 uur

door

Sander Hein Kooi

geboren op 10 maart 1992 te Groningen

Promotor: Prof. dr. C. de Morais Smith
Copromotor: Dr. C. Ortix

Contents

Preface

This thesis is the result of four years of research, done at the Institute for Theoretical Physics of Utrecht University under the supervision of prof. dr. Cristiane de Morais Smith and prof. Carmine Ortix.

In Chapter 1, a brief introduction to some key concepts that will appear throughout this thesis as well as an outline for the rest of the thesis are given. Chapters 2-5 contain original research based on the articles found in the list of publications. Chapter 6 contains the conclusions, after which a Dutch summary, a brief CV and the bibliography can be found.

I wish the reader much enjoyment reading this thesis.

Sander Kooi
July 2020, Utrecht

List of publications

This thesis is based on the following publications:

- ◇ Chapter 2 is based on S.H. Kooi, G. van Miert, and C. Ortix. "Inversion-symmetry protected chiral hinge states in stacks of doped quantum Hall layers."
  Physical Review B, 98(24), 245102 (2018).

- ◇ Chapter 3 is based on S.H. Kooi, G. van Miert, and C. Ortix. "Classification of crystalline insulators without symmetry indicators: Atomic and fragile topological phases in twofold rotation symmetric systems."
  Physical Review B, 100(11), 115160 (2019).

- ◇ Chapter 4 is based on S.H. Kooi, G. van Miert, and C. Ortix. "The hybrid-order topology of weak topological insulators."
  Physical Review B, 102(4), 041122(R) (2020).

- ◇ Chapter 5 is based on S.H. Kooi, A. Quelle, W. Beugeling, and C. Morais Smith. "Genesis of the Floquet Hofstadter butterfly."
  Physical Review B, 98(11), 115124 (2018).

These publications, presented in this thesis, are a result of collaborations with the respective co-authors.

1 Introduction

This thesis is concerned with the electronic properties of insulating crystals. In a conventional insulating crystal, the electrons are trapped in a deep potential well, usually created by the atom to which they are bound. These electrons cannot tunnel to the next potential well, since all states are already occupied, and thus no electrons can move through the material, and no conduction is possible. Why then would one devote an entire thesis to this topic? The answer is that there exists a class of peculiar insulators, which are insulating in the interior of the material, but conducting at the edges.

Dubbed topological insulators, the first of these remarkable phases of matter was discovered in 1980 by Klaus von Klitzing when he applied a strong perpendicular magnetic field to a very thin piece of semiconductor. This turned the interior of the metal into an insulator, but Von Klitzing nevertheless measured a conductance perpendicular to an applied current, coming from conducting edge states [1]. This so-called Hall conductance showed a remarkable quantization. It exhibited plateaus very clearly at an integer times e^2/h, where e is the electron charge and h is the Planck constant, suggesting that by performing this experiment on an ordinary semiconductor, one can determine the Planck constant (assuming we know the value of e). This quantization of the Hall conductance is known as the integer quantum Hall effect.

The appearance of integers, together with the fact that this effect has been seen in many materials, suggests that the origin of this effect is topological. In contrast to the geometry, the topology of the system does not change under small perturbations. Changing the strength of the magnetic field slightly, applying small uniform strain, or taking a sample with a different shape: all this does not alter the Hall conductance. The quantum Hall effect comes from a material in the quantum Hall phase, and this phase is very stable.

While the bulk of the quantum Hall phase is insulating, it is completely different from that of a conventional insulator. In a conventional insulator the electrons can be essentially viewed as charged point particles. In topo-

logical insulators, this picture breaks down, and the wave-like nature of the electron is necessary to describe the electronic properties of the insulator, a hint that these phases are quantum mechanical in nature.

In 2005, another important topological insulator was discovered [2–4]: the quantum spin Hall insulator, which features two counter-propagating conducting edge states, of opposite spin. The spin-up electron propagating in one direction cannot scatter into the spin-down electron coming its way, as long as the system has time-reversal symmetry. Playing a movie of the system backwards is indistinguishable from playing it forward. Each edge state then propagates in the other direction, but the spin also changes, such that the entire system remains the same. The nature of this topological phase is thus different from the quantum Hall phase as here a symmetry is responsible for the protection of the edge states.

Many different symmetries exist in nature, and after the quantum spin Hall phase, many topological phases protected by many different symmetries have been discovered and continue to be discovered to this day. In this thesis, the focus will lie on crystalline symmetries, which are symmetries of the underlying lattice, such as a rotation or mirror symmetry. Our aim is broadly to answer two questions. First, given a crystalline symmetry, what are the possible topological phases protected by this symmetry? Second, given a system with a crystalline symmetry, how can we determine its topology?

In the remainder of this introductory chapter, we give a brief introduction to crystalline topology and an overview of a few important concepts that will be expanded on in later chapters. We end this chapter with a detailed outline of this thesis.

1.1 The atomic insulator

To understand topology in crystals, it is instructive to introduce the concept of the atomic insulator. An atomic insulator is an insulator in the atomic limit, where the wavefunction of each electron is completely localized at a point. Put differently, the electrons can be thought of as charged point particles. The electronic properties of such an insulator are then known once we know the set of points where the electrons are localized. While an ideal limit, such a situation is approached if electrons are very strongly bound to an atom.

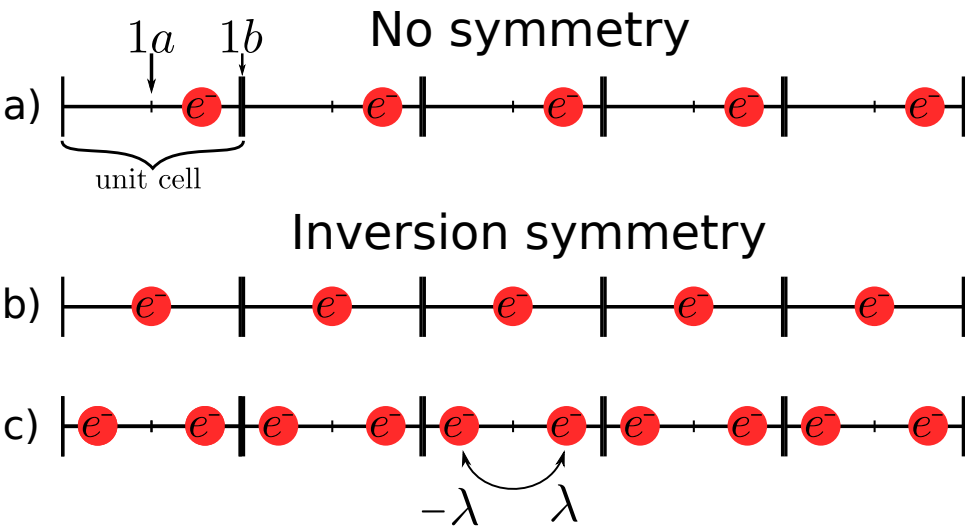

Figure 1.1: One-dimensional chains with (a) one electron at a non-symmetric point, (b) one electron at $1a$ and (c) two electrons at λ and $-\lambda$ per unit cell, that transform into each other under inversion symmetry.

A question to which we will return many times throughout this thesis, is whether two atomic insulators are topologically equivalent. We say that two atomic insulators are topologically equivalent if we can slowly (adiabatically) go from one to the other while (i) preserving all symmetries of the system and (ii) not closing the bandgap in the bulk of the system.

To make this clearer, consider a one-dimensional atomic insulator, where we find exactly one point-like electron within each unit cell, as shown in Fig. 1.1(a). Since we have imposed no symmetries whatsoever on this crystal yet, apart from translation symmetry, we can move the electron slowly to anywhere within this unit cell without breaking the symmetry of the crystal (there are none to break!). This leads us to conclude that with no symmetries, all atomic insulators are topologically equivalent.

This situation changes when we impose a symmetry on the crystal. Take for example a one-dimensional atomic insulator with inversion symmetry. This symmetry sends the coordinate $x \to -x$ and there are now two special positions in the unit cell, namely the middle and the edge of the unit cell, which we will refer to as Wyckoff positions $1a$ and $1b$. These positions are

special because they are mapped onto themselves under inversion symmetry, up to a translation by an integer number of unit cells.

Consider again placing a point-like electron in this crystal. We must now take care to not break the inversion symmetry of the crystal. Therefore, we can only place this point-like electron at a position that is invariant under the symmetry: the middle or the edge of the unit cell. Any other position is not invariant under inversion symmetry, and hence would break the symmetry of the crystal. Furthermore, if we have a point-like electron at say the middle of the unit cell [1.1(b)], we cannot slowly move it away from its position while preserving inversion symmetry. In particular, we cannot move the electron from $1a$ to $1b$ without breaking the symmetry, and thus these two atomic insulators are topologically distinct.

Adding a second localized electron to the system, its wavefunction again must be centered at $1a$ or $1b$. There is however a third option now. The wavefunction of the electron must, by inversion symmetry, either be even or odd. If an even *and* an odd electron wavefunction are localized at say $1a$, they can move away pairwise [1.1(c)]. This means that we will have one electron localized $+\lambda$ away from $1a$, while the other will be localized at $-\lambda$. Inversion symmetry is now still respected, since the two electrons will transform *into each other* under inversion.

This also means that we can take the two electrons at $1a$, and move them away (in opposite directions) until they are now localized at $1b$. Hence, two electrons localized at $1a$, one with an even and one with an odd wavefunction, correspond to the same atomic limit as two electrons localized at $1b$. Even in this simple case of a one-dimensional crystal with inversion symmetry, there are thus already topologically distinct phases to be found.

The above analysis in terms of atomic limits (and thus completely localized electrons), may seem to have little applicability to real materials. In reality, electrons are described by wavefunctions and are not localized at a single point. Even in such systems, however, one can often reach an atomic limit by slowly deforming the system without breaking any symmetries. In other words, many insulators are topologically equivalent to an atomic limit. For convenience, we will broaden our definition of atomic insulator a bit and refer to all insulators that are topologically equivalent to an atomic insulator as atomic insulators.

It turns out that in one dimension all insulators are atomic insulators. By a Fourier transformation, we are always able to construct localized and

symmetric wavefunctions (Wannier functions), that can then be deformed to an atomic limit. In two and three dimensions, this is not always possible.

This forms the basis of the definition non-trivial topology that we will use throughout this thesis: a phase is topologically non-trivial if it is not deformable to any atomic limit [5]. This means that for a topologically non-trivial phase, one cannot construct Wannier functions that are exponentially localized and respect the symmetry of the system. Put another way, atomic insulators are topologically trivial, while non-atomic insulators are topologically non-trivial.

Returning to our example of the one-dimensional crystal with inversion symmetry, we saw that putting an electron at $1a$ or $1b$ results in two topologically different phases. However, both phases are deformable to (different) atomic limits, and hence both are topologically trivial. Two phases might thus be topologically distinct, while still being topologically trivial.

We can also look at this distinction between trivial and non-trivial phases by noting that topologically trivial phases (atomic insulators) are essentially classical phases. Their electronic properties can be described in terms of localized charged point particles. For non-trivial topological phases, this picture breaks down. They require extended electronic wavefunctions to describe them, and hence are truly quantum phases.

1.2 Edge charges

In the previous section, we have seen that crystalline symmetries lead to topologically different phases. A natural question to then ask is: how can we probe this topology? In other words, what are the physical consequences of crystalline topology? One such class of observables are edge and corner charges. While they are in principle measurable, this is very difficult to do in actual materials. Yet, they are still very useful in determining the topology of a phase and provide an intuitive understanding of the appearance of protected edge and surface states, as we will see in the next sections.

To understand what edge charges are, let us return to the one-dimensional crystal with inversion symmetry, and imagine a chain of finite length. Clearly, the total number of electrons in the finite chain is an integer. If we divide the chain precisely in half, and sum the charge density in one half of the chain, this must then add up to either an integer, or half-integer. This is

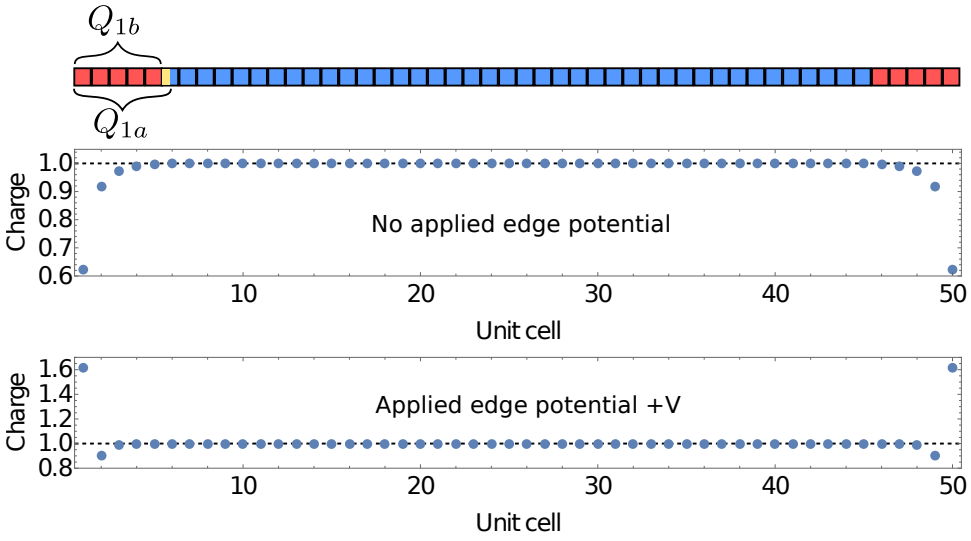

Figure 1.2: Schematic drawing of a one-dimensional inversion symmetric chain with a length of 50 unit cells. Below is a plot of the charge density per unit cell with no applied edge potential, and with an applied edge potential.

because the left-half of the chain must be exactly equal to the right-half in order to respect the inversion symmetry, under which $x \to -x$. Inside the bulk of the chain, far enough from the edges, there will be an integer amount of electron charge per unit cell. Near the edges however, this charge density may fluctuate, and it follows that a possible excess of charge can only be localized at the edge.

In Fig. 1.2, we show the charge density for a simple tight-binding model of a finite one-dimensional inversion symmetric chain with a length of 50 unit cells, and we see indeed that the charge per unit cell deviates from 1 near the edges. Taking the sum of the charge in the leftmost 5 unit cells, we find a charge of 4.50, and thus $Q_{edge} = 0.50 \mod 1$. Instead we could have summed over the leftmost 7 or 10 unit cells, but this would not have changed value of the edge charge modulo 1. If we pick the region to be too small, for example 2, we will not exactly find an edge charge of 0.5, since we are then not terminating the region in the bulk. The charge fluctuations will fall off exponentially, but how quickly it decays is determined by the microscopic details of the model.

What makes these edge charges interesting, is that they are related to the bulk topology. This means that they are determined by the bulk, and not dependent on the details at the edge. Picking an edge region terminated at the edge or middle of a unit cell, the charge in this region cannot change by symmetric perturbations at the edge. Returning to the chain, we can for example turn on a potential $-V$ just at the edges of the chain. This will lower the energy of the states at the edge of the chain, and two additional states will be occupied. Summing again the charge in the first five unit cells, we now find 5.5. We see that the charge distribution has changed, but the value $Q_{edge} \mod 1$ has not. As long as we do not change the symmetry in the bulk, or close the bandgap, the edge charge cannot change.

By choosing to sum the charge in an integer number of unit cells, we have picked a region that terminates at the edge of the unit cell, Wyckoff position $1b$. Now suppose that we pick a region that terminates in the middle of the unit cell, Wyckoff position $1a$, what would the charge in this region be? The difference between these two regions is half a bulk unit cell. In the bulk, each unit cell contains an integer amount of charge, and the charge density within a bulk unit cell is inversion symmetric around Wyckoff position $1a$. Hence, in the left half of a bulk unit cell there will be either an integer of half-integer charge.

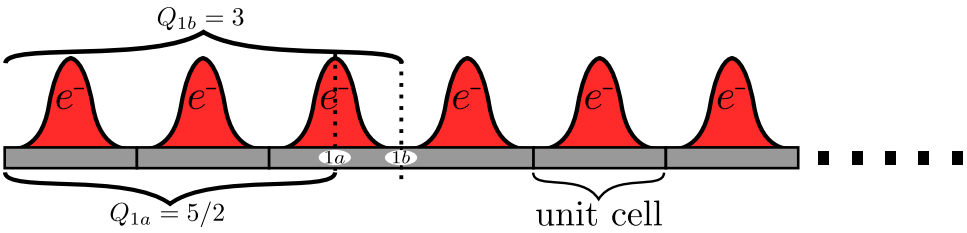

Figure 1.3: Schematic drawing of the left edge of a one-dimensional inversion symmetric chain. The chain features one occupied electron per unit cell, with a wavefunction centered around the middle of the unit cell ($1a$). Summing the charge in an edge region terminated $1b$ will yield an integer edge charge Q_{1b}, while summing the charge in a region terminated in $1a$ will yield an edge charge Q_{1a} that is half-integer.

It follows from this observation that the difference in charge between the two regions is either 0 or 1/2 mod 1. Hence, also the charge in the region that terminates at $1a$ is quantized. Let us call this edge charge Q_{1a}, and the edge charge with respect to $1b$, Q_{1b}.

Now that we have two bulk quantities, Q_{1a} and Q_{1b}, we would like to relate them to the topology of the crystal. Let us again consider a one-dimensional crystal with an electron localized at Wyckoff position $1a$, the middle of the unit cell (Fig. 1.3). What will the edge charges be of such a crystal? Let us start by picking an edge region that terminates at $1b$, thus containing an integer number of unit cells. Looking at the electron wavefunctions, we see that this region contains an integer number of electrons, and hence $Q_{1b} = 3 = 0 \mod 1$. If instead we consider a region terminated at $1a$, we see that the region terminates exactly where an electron is localized, which will contribute half an electron charge and thus $Q_{1a} = 5/2 = 1/2 \mod 1$.

Hence, the localized electron at position $1a$ contributes a charge of 1/2 to Q_{1a}. This correspondence between localized electrons and edge charge is general, and for one-dimensional chains with inversion symmetry we have

$$Q_{1a} = \frac{1}{2} \times \#\,\text{electrons localized at } 1a \mod 1,$$
$$Q_{1b} = \frac{1}{2} \times \#\,\text{electrons localized at } 1b \mod 1.$$

Thus, the edge charges are directly determined by the topology of the system.

Vice versa, if we know the corner charges, we know if there are an even or odd amount of electrons localized at the corresponding Wyckoff position.

1.3 Corner charges

In one-dimensional insulators, the edge charges thus provide physical observables that are directly related to the topology of the crystal. How does this compare to two-dimensional insulators? Analogous to one dimension, edge charges can be quantized by rotation, mirror or inversion symmetry in two dimensions. But are there any new probes of topology in two dimensions?

The answer is yes, corner charges are precisely such a new probe of topology, not found in one dimension. To understand this quantity, let us consider a fourfold-rotation ($\mathcal{C}_4$) symmetric crystal, meaning the crystal is invariant under quarter rotations. A $\mathcal{C}_4$ symmetric unit cell has four symmetric Wyckoff positions [Fig. 1.4(a)], in contrast to the two for the one-dimensional inversion symmetric chain. The origin ($1a$) and the corner ($1b$) are $\mathcal{C}_4$ symmetric points. There are two other points ($2c$), located at the middle of the edges of the unit cell, that are not $\mathcal{C}_4$ symmetric, but they do transform into each other under a quarter rotation.

A finite sample of such a crystal can now be divided into three regions, the bulk, the edges and the corners [Fig. 1.4(b)], where we terminate the corner regions in the corners of the unit cells. In the bulk, each unit cell will again contain an integer number of electrons, and hence the total bulk region will contain an integer number of electrons. Following similar reasoning as for the one-dimensional inversion symmetric chain, by fourfold rotation symmetry the edge charge is quantized to be 0 or $1/2 \mod 1$. This means that the total charge in the two opposite edge regions will be an integer. Since the total charge is integer and the bulk plus edge charge is integer, the sum of the charge in the corner regions must also be integer. Furthermore, all corner regions must contain an equal amount of charge, since the crystal is $\mathcal{C}_4$ symmetric. Four times the charge in one corner must thus be an integer, and thus the charge in one corner must be a multiple of $1/4$.

Again following the example of the one-dimensional inversion symmetric chain, we can apply a potential to all four corners. In this way, four additional states can be occupied at the corners, and the corner charge in one corner changes by 1. Therefore, as with the edge charge, the corner charge is

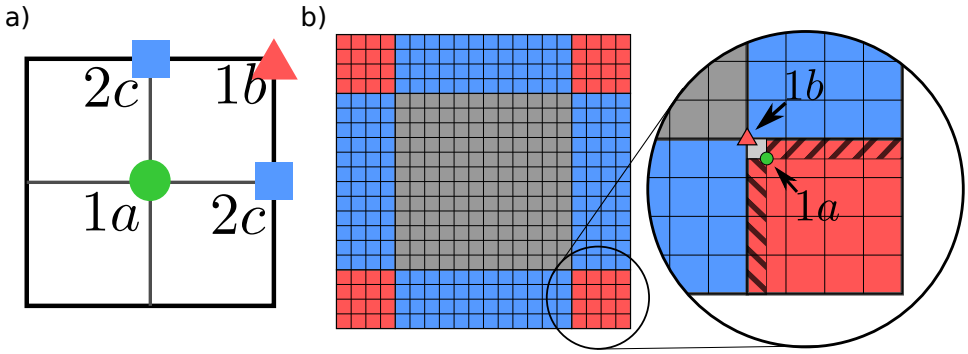

Figure 1.4: (a) Unit cell of a fourfold rotation symmetric unit cell, containing two $\mathcal{C}_4$-symmetric ($1a$ and $1b$), and two $\mathcal{C}_2$-symmetric ($2c$) Wyckoff positions. (b) Schematic drawing of a finite geometry of such a crystal, divided into three regions: the bulk (gray), the edges (blue) and the corners (red). In the zoom in, we see that the corner region is terminated at Wyckoff position $1b$ (the red triangle). To calculate the charge with respect to $1a$, we should instead sum the charge in a corner region terminated at the green circle ($1a$). The difference between these two charges will be a quarter of a bulk unit cell (the gray square), and one strip from the edge to the bulk (the two striped regions together).

only well defined modulo 1. So far, we have considered a region terminated at the corner of the unit cell, Wyckoff position $1b$. We could also terminate the corner region in the center of the unit cell $1a$, the other $\mathcal{C}_4$ symmetric point. This will give the corner charge Q_{1a} with respect to position $1a$.

A closer look at the difference between the two regions shows that the difference between Q_{1a} and Q_{1b} is one quarter of a bulk unit cell, and one strip of the edge region terminated at $1b$ [Fig. 1.4(b)]. The charge in the edge strip is quantized by the rotation symmetry, and the charge in a quarter of the bulk unit cell will be an integer divided by four. In this way we see that the charge with respect to $1a$ is also quantized to a multiple of $1/4$.

For atomic insulators, a non-trivial corner charge is due to localized electrons at the corresponding Wyckoff position. Looking at the zoom-in of Fig. 1.4(b), imagine an electron localized at $1b$. The red corner region will include a quarter of the electron localized at the red triangle. Along the edge, it will cut electrons in half, but this is compensated by the electrons cut by the other edge. Any non-integer part of the corner charge, for an atomic insulator, must thus come from electrons localized at $1b$. Hence, for fourfold rotation symmetry, we again find a relation between the corner charges and atomic insulators

$$\begin{aligned} Q_{1a} &= \frac{1}{4} \times \#\,\text{electrons localized at } 1a \mod 1, \\ Q_{1b} &= \frac{1}{4} \times \#\,\text{electrons localized at } 1b \mod 1, \end{aligned} \tag{1.1}$$

where Q_{1a} is now the corner charge with respect to $1a$.

This provides us with a relation between the corner charges and the topology of atomic insulators. But as already alluded to above, in two dimensions there are not just additional physical observables, but also additional topological phases of matter. In two dimensions, it is no longer true that every insulator is deformable to an atomic limit, and there exist also non-atomic insulators.

The relations between corner charges and the number of localized electrons of Eq. (1.1) are derived under the assumption that the insulator is atomic and for non-atomic insulators these relations thus do not necessarily hold. This allows us to combine the two relations into an inequality that is always

satisfied for atomic insulators, namely

$$4(Q_{1a} + Q_{1b}) \leq N_F,$$

where N_F is the number of electrons per unit cell in the bulk. Suppose, for example, that we have a crystal with a corner charge Q_{1b} of 1. If the crystal is an atomic insulator, this corner charge must be due to two localized electrons at $1b$, and thus N_F must be at least two.

If this inequality is not satisfied, we are sure that the insulator for which this is the case is non-atomic, and hence a topologically non-trivial insulator. Such phases are called fragile topological phases [6, 7], since they can become an atomic insulator when additional atomic bands are occupied. We will investigate fragile topological phases in more detail in Chapters 3, and 4.

1.4 Edge and hinge states

We have found that in two dimensions, the corner charge can not only tell us something about the topology of atomic insulators, but sometimes also diagnose an insulator as non-atomic. While it is interesting that these corner charges, being physical observables, reflect the bulk topology, they are very difficult to measure. We are therefore left wondering if crystalline topological phases can protect something more interesting.

Conducting edge states are an obvious candidate, as the very first topological insulator that we discussed, the quantum Hall phase, protects exactly such states. In this section, we will show that the quantum Hall phase can be understood by considering the two-dimensional system as a collection of one-dimensional systems. By analyzing the edge charges of the one-dimensional systems, we can predict the existence of protected edge states. We then show that we can similarly consider a three-dimensional system as a collection of two-dimensional systems, and by analyzing their corner charges we can predict one-dimensional conducting hinge states in three-dimensional systems.

To start, consider a two-dimensional insulating crystal with inversion symmetry. In two dimensions, inversion symmetry changes the sign of the coordinates, $x \to -x$ and $y \to -y$. Instead of a finite square sample, we now consider a ribbon geometry, which is finite in the x direction, but infinite in the y direction. Since this direction is infinite, we can apply a Fourier

transformation to the y coordinate, which yields the periodic momentum coordinate k_y. Under inversion, the momentum also changes sign $k_y \to -k_y$. We now have a crystal described by the coordinate and momentum (x, k_y). This can be viewed as a collection of finite 1D crystals, one for each k_y. Only two of these one-dimensional chains are inversion symmetric however, the ones at $k_y = 0$ and at $k_y = \pi$ (since k_y is 2π-periodic). These two inversion-symmetric chains have, as we have seen in the previous section, quantized edge charges.

Suppose now that at $k_y = 0$ the 1D chain has an edge charge of $Q_{1b} = 0$, while the one-dimensional chain at $k_y = \pi$ has $Q_{1b} = 1/2$ [Figs. 1.5(a)-(b)]. Away from $k_y = 0, \pi$, the one-dimensional chains will not have inversion symmetry, and hence the edge charge will not be quantized. We now consider the left edge charge of such a system as a function of k_y, as plotted in Fig. 1.5(c). The edge charge will also not be equal in both ends of the chain, but the sum will still be integer. By inversion, the chain at k_y will be equal to the one at $-k_y$, but reversed (since $x \to -x$). Therefore, the corner charges are related, $Q(k_y) = -Q(-k_y)$. Following a cycle of k_y from 0 to 2π, one unit of charge has been added to the left edge of the chain.

Hence, as a function of k_y, this system realizes a charge pump. At $k_y = 2\pi$ the charge at the left edge has increased by 1, and the charge at the right edge has decreased by 1. However, the momentum k_y is 2π-periodic. This means that the system at $k_y = 0$ and $k_y = 2\pi$ must have the same edge charge. Yet we saw that the edge charge increased by 1, how is this possible? The explanation is that somewhere the edge charge made a jump of 1. Note that since we are plotting the edge charge modulo 1, this jump does not show up in Fig. 1.5(c).

Such a jump in the edge charge can only come from a state, localized at the edge, crossing the Fermi energy (the energy below which all states are occupied). This can be seen by plotting the energy spectrum of the ribbon as a function of k_y [Fig. 1.5(d)]. We see that indeed two states cross the gap, one right-moving and one left-moving. Each of these states is localized at a different edge. If we consider a finite square geometry, there will be one edge state moving around the edge of the system. This is an example of a Chern insulator, which falls into the same class as the quantum Hall phase.

We repeat this construction, but now with corner charges instead of edge charges. Hence, we take a three-dimensional system, infinitely extended in the z direction, and consider it as a collection of $\mathcal{C}_4$-symmetric 2D systems

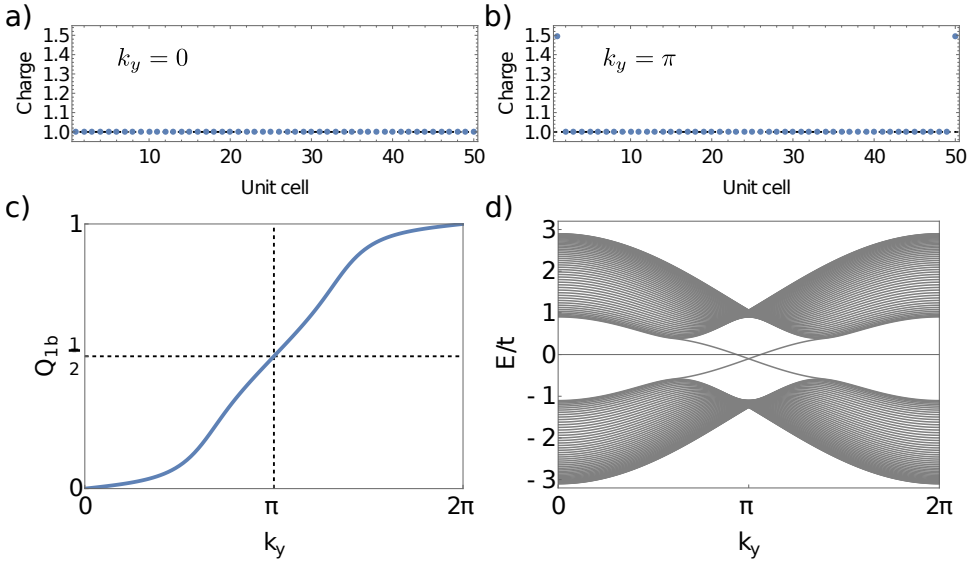

Figure 1.5: (a) Charge density per unit cell of the 1D chain at $k_y = 0$. (b) Charge density per unit cell of the 1D chain at $k_y = \pi$. (c) The edge charge modulo 1 of the bottom five unit cells as a function of k_y. Between 0 and 2π the edge charge increases by 1. (d) Energy spectrum for a ribbon geometry with a width of 50 unit cells. Two bands cross the gap of the spectrum, each localized at opposite edges of the ribbon.

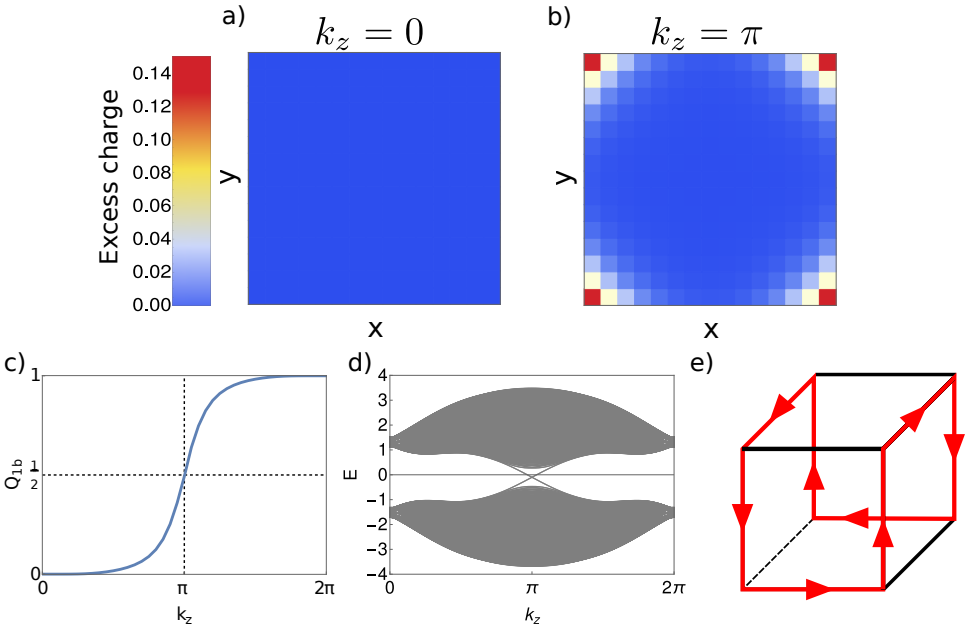

Figure 1.6: Charge density per unit cell of the two-dimensional system at (a) $k_z = 0$ and (b) $k_z = \pi$. (b) The corner charge of the bottom-left corner as a function of k_z. (d) Energy spectrum as a function of k_z, with the x and y directions finite. (e) Schematic of the hinge states present in a finite geometry of the system.

parametrized by k_z. For each k_z, we then have a $\mathcal{C}_4$ symmetric crystal, and at $k_z = 0$ we take a crystal with $Q_{1b} = 0$ [Fig. 1.6(a)], while at $k_z = \pi$ we take $Q_{1b} = 1/2$ [Fig. 1.6(b)]. If we plot the corner charge in the lower-left corner Q_{1b} as a function of k_z, it will flow from 0 at $k_z = 0$ to 1/2 at $k_z = \pi$.

In order to realize a corner charge pump, we want the corner charge to go to 1 as a function of k_z, and to guarantee this we need the relation $Q_{1b}(k_z) = -Q_{1b}(-k_z)$. We can get this relation if we alter the symmetry slightly: instead of considering a crystal with $\mathcal{C}_4$ symmetry, we consider $\mathcal{C}_4 \times \mathcal{M}_z$ symmetry [8]. $\mathcal{M}_z$ is a mirror symmetry in the z direction, which sends $z \to -z$ and $k_z \to -k_z$. This does not affect the $k_z = 0, \pi$ planes, but now relates the two-dimensional crystal at k_z to the one at $-k_z$, and leads to the corner charge flow in Fig. 1.6(c).

This corner charge then leads to four states that cross the Fermi energy,

as can be seen in Fig. 1.6(d). These states are localized at the corners of the two-dimensional systems. If we consider this system in a cube geometry (finite in all directions), we will find hinge states in the configuration as seen in Fig. 1.6(e). Note that this pattern of hinge states also respects $\mathcal{C}_4 \times \mathcal{M}_z$ symmetry. In order for these hinge states to be protected, the geometry of the system should respect the symmetry of the crystal.

This is an example of a higher-order topological insulator [9], since it features one-dimensional protected edge states in a three-dimensional system. In contrast, first-order topological insulators (such as the quantum spin Hall phase), feature protected edge states in a dimension only one lower than the bulk (one-dimensional protected edge states in a two-dimensional system). Higher-order topological insulators will be extensively discussed in Chapters 2 and 4.

1.5 Outline

This introductory Chapter has been purely theoretical, and has made little reference to actual materials. Indeed, one of the challenges is to find material platforms where protected hinge states can be measured. In Chapter 2, we propose a model of a higher-order topological insulator featuring inversion symmetric chiral hinge states consisting of a coupled layer construction. In particular, we show that a homogeneous external magnetic field slightly tilted away from the stacking direction drives alternating p- and n-doped honeycomb sheets into a higher-order topological phase, characterized by a nontrivial three-dimensional $\mathbb{Z}_2$ invariant. We identify graphene, silicene, and phosphorene multilayers as potential material platforms for the experimental detection of this second-order topological insulating phase.

Another challenge is classifying topological phases, and especially finding a bulk formulation of the topological invariants for systems with time-reversal symmetry. In Chapter 3, we give such a classification for 2D crystalline insulators that are twofold-rotation and time-reversal symmetric. These systems cannot be classified using symmetry indicators, and we instead identify a set of three $\mathbb{Z}_2$ topological invariants, which correspond to nested quantized partial Berry phases. By considering which phases correspond to atomic insulators, we infer the existence of new fragile topological insulating phases that are diagnosed as trivial by symmetry indicators, and construct a num-

ber of microscopic models exhibiting this phase.

In Chapter 4, we ask the question whether crystalline symmetries can lead to new topological phases in quantum spin Hall phases. We show that indeed two-fold rotation symmetry protects a novel crystalline topological invariant that can neither be revealed by symmetry indicators, nor by Wilson loop invariants. By exploiting this invariant, we are able to construct a three-dimensional hybrid-order topological insulator, which features Dirac cones on the side surfaces protected by time-reversal symmetry and translation symmetry, and cones on the top and bottom surfaces protected by two-fold rotation and time-reversal symmetry.

Finally, in Chapter 5 we investigate theoretically the spectrum of a graphene-like sample (honeycomb lattice) subjected to a perpendicular magnetic field and irradiated by circularly polarized light. This system is studied using the Floquet formalism, and the resulting Hofstadter spectrum is analyzed for different regimes of the driving frequency.

2 Chiral hinge states in stacks of doped quantum Hall layers

A free-fermion symmetry protected topological (SPT) insulator is a quantum state of matter that cannot be adiabatically deformed to a trivial atomic insulator without either closing the insulating bulk band gap or breaking the protecting symmetry [5, 10]. Its topological nature is reflected in the general appearance of gapless boundary modes in one dimension lower [11, 12]. However, when the protecting symmetry is a crystalline symmetry the gapless boundary modes appear only on surfaces which are left invariant under the protecting symmetry operation [13, 14]. Most importantly, these gapless boundary modes are "anomalous": on a single surface the number of fermion flavors explicitly violates the fermion doubling theorem [15] or stronger versions of it [16].

Very recently, it has been shown that point-group symmetries can stabilize insulating states of matter in bulk crystals with conventional gapped surfaces, but with gapless modes at the hinges connecting two surfaces related by the protecting crystalline symmetry [9, 16–31]. For systems of spinless electrons (negligible spin-orbit coupling) the hinge modes are chiral. Hence, they represent anomalous one-dimensional (1D) modes – they cannot be encountered in any conventional 1D atomic chain – but now embedded in a three-dimensional crystal. These novel topological crystalline insulators, which have been dubbed higher-order topological insulators, have started to be classified in systems possessing different crystalline symmetries, including rotational and rotoinversion symmetries [8, 17, 18, 27, 29].

In inversion-symmetric crystals, higher-order topological insulators can also exist [25]. However, in this case, inversion symmetry-related surfaces are connected via two hinges, one of which will host a chiral gapless mode. This, in turn, gives rise to an additional modulo two ambiguity in the microscopic hinge location of the chiral modes, reminiscent of the ambiguity in the Fermi arcs connectivity of Weyl semimetals [32].

The aim of this chapter is to show that such an inversion-symmetry pro-

tected higher-order topological insulator can be in principle obtained in stacks of doped honeycomb layers (e.g. graphene, silicene, and phosphorene) subject to an external magnetic field tilted away from the stacking direction. Two factors conspire to render this possible. First, the quantum Hall states in p- and n-doped layers generally have opposite sign of the Hall conductance and hence are characterized by opposite Chern numbers $\mathcal{C}$ [33]. Second, a finite component of the magnetic field in the layer planes intrinsically breaks both the reflection symmetry in the stacking direction and the twofold rotation about the stacking direction, but still preserves the three-dimensional bulk inversion symmetry. We first give an intuitive argument for the existence of an inversion- symmetric higher-order topological insulator in stacks of Chern insulators with alternating $\mathcal{C} = \pm 1$ integer invariants, and show that this insulating phase can be derived from a parent mirror Chern insulator [34] by adding crystalline symmetry-breaking terms. Then, we introduce a corresponding minimal tight-binding model consisting of quantum anomalous Hall layer stacks [35], and verify its topological nature by computing the corresponding bulk $\mathbb{Z}_2$ invariant [8]. Finally, we perform a full Hofstadter [36] calculation in three-dimensions [37] for honeycomb layers doped in an alternating fashion to show the existence of topologically protected chiral hinge states.

2.1 Effective surface theory

Let us start out with an effective low-energy approach for stacks of Chern insulating layers of alternating $\mathcal{C} = \pm 1$ integer topological invariant [c.f. Fig. 4.2(a)]. At any edge perpendicular to the stacking direction, each Chern insulating layer is characterized by an anomalous chiral edge mode whose dispersion can be considered to be linear. For completely uncoupled layers, the effective surface Hamiltonian in the primitive two-layer surface unit cell then reads $\mathcal{H}_0 = k_x \sigma_z$, where the Pauli matrix acts in the layer space and we explicitly considered a (010) surface. We next introduce an interlayer coupling between consecutive layers with a coupling strength, which, for simplicity, we assume to be real. The effective surface Hamiltonian is then modified accordingly to $\mathcal{H}_S = \mathcal{H}_0 + t\left[1 + \cos\left(k_z\right)\right]\sigma_x - t \sin\left(k_z\right)\sigma_y$. It preserves mirror symmetry in the stacking direction around one layer [34] with the reflection operator that acquires an explicit momentum depen-

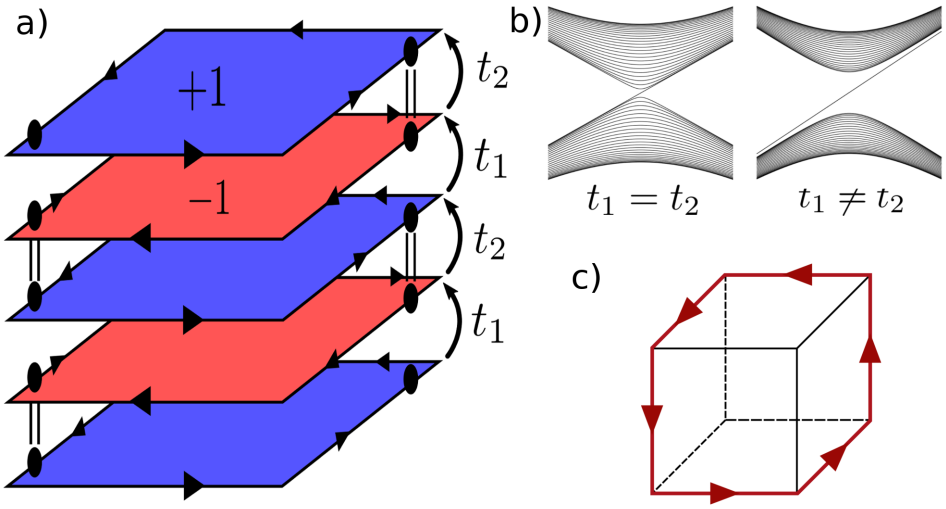

Figure 2.1: a) Sketch of stacked Chern insulators with alternating Chern numbers. We also indicate the effective inversion-symmetric coupling between the chiral edge states. b) Corresponding surface energy spectrum for mirror symmetric couplings ($t_1 = t_2$) and inversion-symmetric couplings ($t_1 \neq t_2$). c) Schematic figure of the inversion symmetric hinge states in a cube geometry.

dence and reads $\mathcal{M}(k_z) = \mathrm{diag}\left(1, \mathrm{e}^{-ik_z}\right)$. The mirror symmetry constraint $\mathcal{M}(k_z)\mathcal{H}_S\mathcal{M}(k_z)^{-1} \equiv \mathcal{H}_S\left(k_z \to -k_z\right)$ implies a decoupling of the chiral modes on the $k_z = \pi$ line. Hence, the three-dimensional system is characterized by gapless surfaces with a mirror-symmetry protected single Dirac cone with the Dirac point at $\{k_x, k_z\} = \{0, \pi\}$.

The presence of this single surface Dirac cone can also be seen as a consequence of the fact that the bulk three-dimensional Hamiltonian is characterized by a non-zero mirror Chern number [38] $\mathcal{C}_\mathcal{M} = 1$ at $k_z = \pi$. When considering systems with a finite number of layers still preserving reflection symmetry in the stacking direction – this constraint is fulfilled for stacks with an odd number of layers – the surface spectrum in the remaining translational invariant k_x direction will therefore display a single uncoupled chiral mode as schematically shown in Fig. 4.2(b). We emphasize that this chiral anomaly is regularized by the presence of a chiral mode partner with opposite chirality at the opposite $(0\bar{1}0)$ surface.

We next "trivialize" our system by introducing a perturbation that explicitly breaks the mirror symmetry along the stacking direction. To this end, we consider a dimerization pattern in the interlayer coupling which further modifies the effective surface Hamiltonian as $\mathcal{H}_S = \mathcal{H}_0 + [t_1 + t_2 \cos(k_z)]\,\sigma_x - t_2 \sin(k_z)\sigma_y$ [c.f. Fig. 4.2(a)]. This, in turn, implies that the single surface Dirac cone acquires a mass $\propto t_1 - t_2$ and the surface becomes a conventional gapped one. When considering, as before, a finite system with an odd number of layers there will be a single chiral mode traversing the full surface gap [c.f. Fig. 4.2(c)] localized at one of the two boundary layers depending upon the specific dimerization pattern. The existence of this chiral hinge mode can be understood by considering the effective surface Hamiltonian as a collection of one-dimensional Rice-Mele models [39, 40], parametrized by k_x. For a chain with an odd number of sites, the latter displays an in-gap boundary state at an energy corresponding precisely to the staggered chemical potential $\equiv k_x$. If we assume the dimerization pattern to be equivalent at all the four surfaces perpendicular to the layer planes, the hinge modes at the boundary layer will be connected to create a circulating planar current, which is in agreement with the fact that a dimerized stack of an odd number of layers defines a (thicker) two-dimensional Chern insulating state [41].

Let us now instead assume that the dimerization patterns at the two opposite surfaces (010) and $(0\bar{1}0)$ are designed to be opposite to each other as shown in Fig. 4.2(a). Although still breaking mirror symmetry along

the stacking direction, this configuration preserves bulk inversion symmetry with the inversion center lying at the center of one layer. The presence of inversion symmetry also implies that the chiral hinge modes related to the (010) and $(0\bar{1}0)$ surfaces will be localized on opposite boundary layers. The same clearly holds true at the (100) and $(\bar{1}00)$ surfaces. Moreover, the Jackiw-Rebbi mechanism [42] guarantees the existence of an additional chiral hinge mode at two inversion- symmetry related hinges between the x and y planes, and thus the configuration of in-gap hinge states schematically shown in Fig. 4.2(c) is realized. The latter represents nothing but the hallmark of a second-order topological insulator in three-dimensions protected by inversion symmetry.

2.2 Quantum anomalous Hall stacks

Having presented our coupled-layer low-energy approach, we next introduce a microscopic model that features an inversion-symmetric higher-order topological insulating state. Specifically, we consider stacks of honeycomb layers, each of which possesses chiral orbital currents leading to a quantum anomalous Hall (QAH) insulating state [35]. In order to have alternating Chern numbers on the honeycomb layers, we further assume the direction of the orbital currents to be opposite in two consecutive layers. For uncoupled layers, the corresponding tight-binding Hamiltonian reads

$$\mathcal{H}_{\parallel} = -t \sum_{\langle i,j\rangle,\alpha} c^{\dagger}_{i\alpha} c_{j\alpha} - it_2 \sum_{\langle\langle i,j\rangle\rangle,\alpha} (-1)^{\alpha} \nu_{ij} c^{\dagger}_{i\alpha} c_{j\alpha},$$

where $c^{\dagger}_{i\alpha}$ ($c_{i\alpha}$) creates (annihilates) an electron on site i in layer α, t is the intralayer nearest-neighbor hopping amplitude and t_2 is the next-nearest neighbor hopping amplitude. As usual, the factor $\nu_{ij} = 1$ if the next-nearest neighbor hopping path rotates counterclockwise, and -1 if it rotates clockwise. We next introduce an interlayer coupling that explicitly breaks the mirror symmetry in the stacking direction but still preserves bulk inversion symmetry with the inversion center in one layer at the center of the bond between the two A and B honeycomb sublattices. In its simplest form the

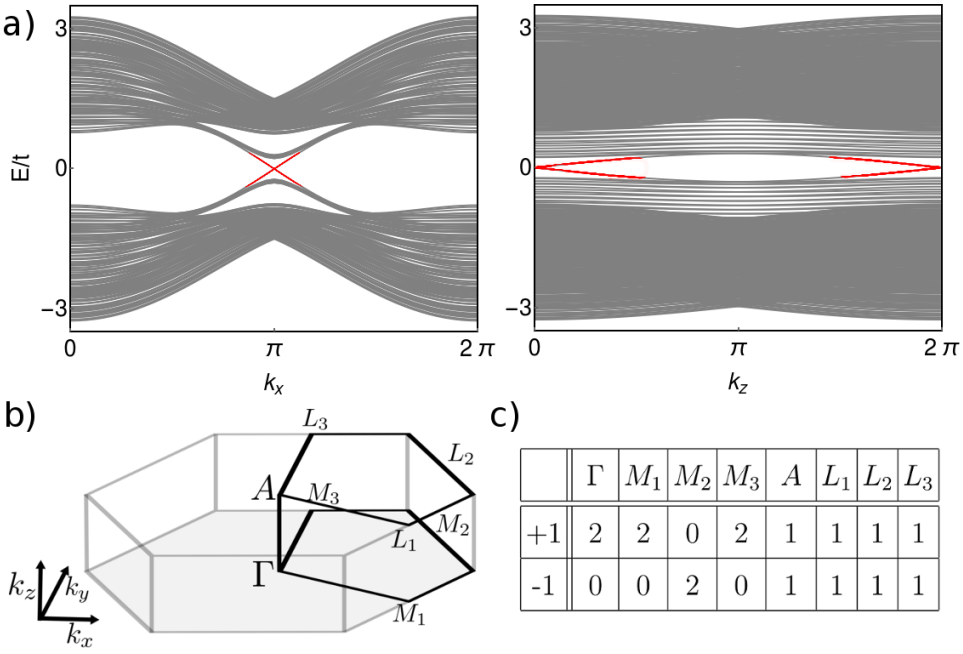

	Γ	M_1	M_2	M_3	A	L_1	L_2	L_3
+1	2	2	0	2	1	1	1	1
-1	0	0	2	0	1	1	1	1

Figure 2.2: a) Edge spectra of the QAH model with periodic boundary conditions in the x- and z-direction for stacks of zigzag-terminated honeycomb flakes. The tight-binding Hamiltonian parameters have been chosen as $t_2/t = 0.2$ and $t_z/t = 0.3$. b) The hexagonal 3D Brillouin zone with the inversion symmetric points labeled. c) Table specifying the number of bands with inversion eigenvalue +1 and -1 at the inversion symmetric points in the Brillouin zone.

interlayer Hamiltonian is then

$$\mathcal{H}_\perp = -\frac{t_z}{2}\sum_{i\in A,\alpha}\left[1-\mathrm{e}^{i\pi\alpha}\right]c^\dagger_{i\alpha}c_{i\alpha+1} - \frac{t_z}{2}\sum_{i\in B,\alpha}\left[1+\mathrm{e}^{i\pi\alpha}\right]c^\dagger_{i\alpha}c_{i\alpha+1} + h.c. \quad (2.1)$$

As discussed in Appendices B and C, this interlayer Hamiltonian is naturally realized assuming buckled honeycomb layers. Fig. 2.2(a) shows the edge energy spectrum as obtained by diagonalizing the full Hamiltonian $\mathcal{H} = \mathcal{H}_\parallel + \mathcal{H}_\perp$ for stacks of zigzag terminated ribbons with an odd number of layers. It agrees perfectly with the foregoing low-energy description. Inside the gapped bulk energy bands, we clearly observe conventional surface states, corresponding to a massive surface Dirac cone, in the gap of which two chiral hinge modes localized on opposite layers appear. Precisely the same features occur considering periodic boundary conditions in the stacking direction and zigzag terminations in the other two directions. We point out that we excluded from our analysis ribbons with armchair terminations since the latter would yield an unprotected single massless surface Dirac cone. This is due to the fundamental difference between the chiral edge states of a QAH insulator for zigzag and armchair terminated ribbons [43]. For the latter, the chiral edge states have an equal amplitude on both the two honeycomb sublattices. The interlayer coupling Hamiltonian introduced above thus yields an effective mirror-symmetric coupling between the QAH chiral edge states. However, additional symmetry- allowed terms in the bulk Hamiltonian, *e.g.* intralayer real next- nearest-neighbor hopping amplitudes, will gap the surface Dirac cone leading to the observation of chiral hinge modes even for stacks of armchair terminated ribbons.

To prove the topological origin of these chiral hinge states, we have calculated the bulk $\mathbb{Z}_2$ topological invariant for a second-order topological insulator with inversion symmetry [8]. It can be derived using the bulk formulation of the quantized corner charges for the effective two-dimensional inversion-symmetric Hamiltonians at $k_z = 0, \pi$, and thereafter considering the corresponding corner charge flow. When expressing the corner charges in terms of the multiplicities of the inversion symmetry eigenvalues ± 1 of the occupied bands at the inversion-symmetric momenta of the 3D Brillouin zone [c.f. Fig. 2.2(b)], we then find the following expression for the bulk $\mathbb{Z}_2$ invariant:

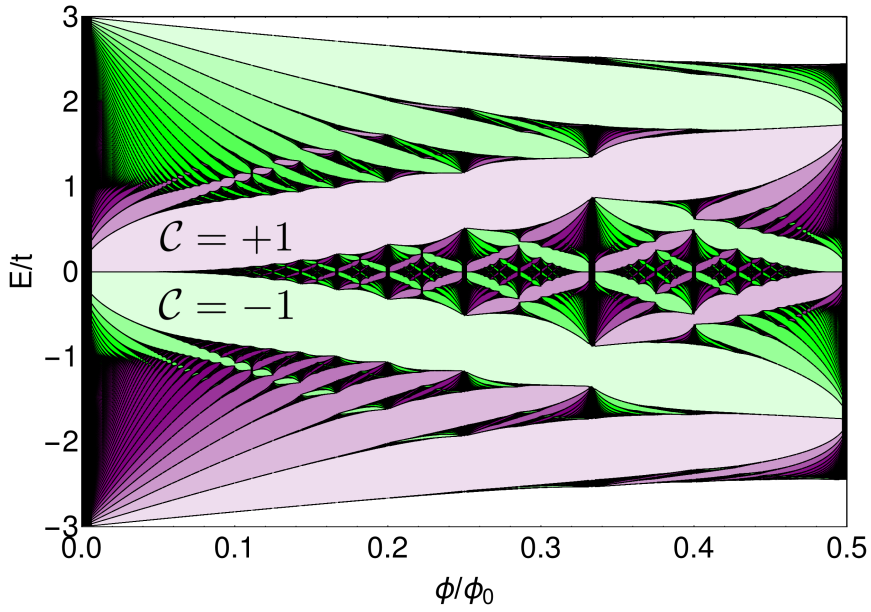

Figure 2.3: Energy versus magnetic flux ϕ (measured in units of the magnetic flux quantum ϕ_0) for the Hofstadter model on a honeycomb lattice. The gaps are coloured according to their Chern number. The two largest gaps have $\mathcal{C} = \pm 1$.

$$\nu = \Big[-\Gamma_1 - \frac{1}{2}\Gamma_{-1} + \frac{1}{2}\left[(M_1)_{-1} + (M_2)_{-1} + (M_3)_{-1}\right] + A_1 + \frac{1}{2}A_{-1} - \frac{1}{2}\left[(L_1)_{-1} + (L_2)_{-1} + (L_3)_{-1}\right] \Big] \tag{2.2}$$

A non-trivial value $\nu = 1 \bmod 2$ of this invariant guarantees the presence of chiral hinge modes provided the bulk and the surfaces are gapped. For our model at half-filling, the inversion symmetry labels [c.f. Fig. 2.2(c)] directly imply an higher-order topology. Therefore the chiral hinge states shown in Fig. 2.2(a) are the direct manifestation of a bulk-hinge correspondence.

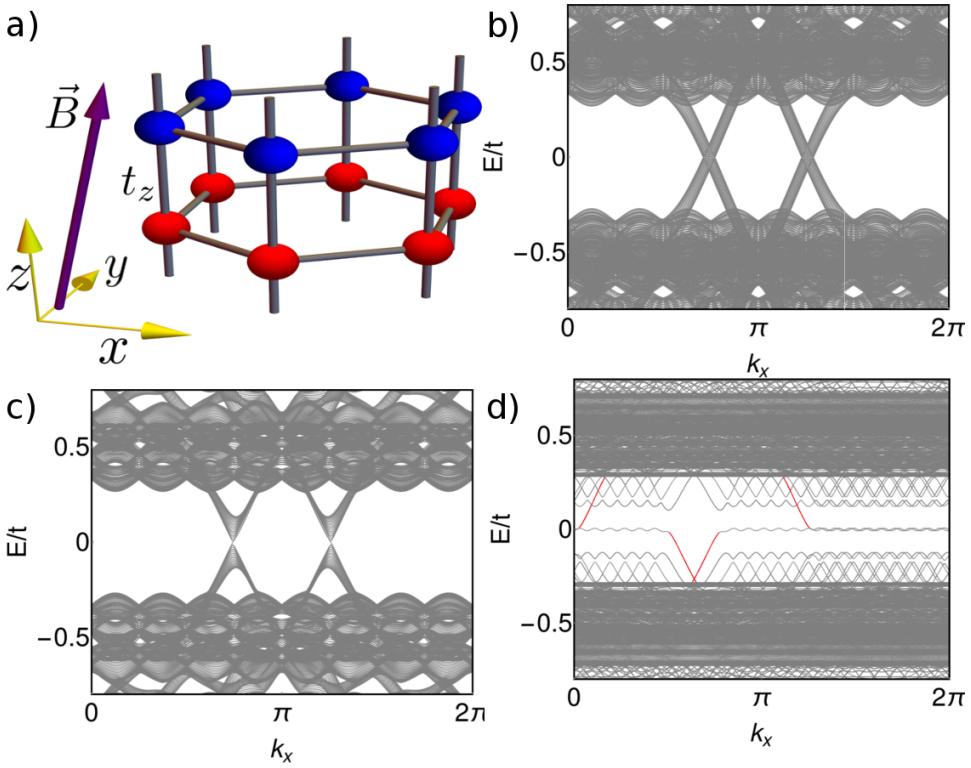

Figure 2.4: a) Schematic side-view of an AA stacked honeycomb lattice in a canted magnetic field. b) Spectrum for a zigzag ribbon of alternately doped stacks of graphene with $t/t_z = 0.2$, $\phi/\phi_0 = 1/8$, $V_0 = 0.5$ and $\phi_2/\phi_0 = \phi_3/\phi_0 = 0$, where ϕ/ϕ_0, ϕ/ϕ_1 and ϕ/ϕ_2 are the flux per plaquette in the z, x and y direction respectively. c) Same as (b), but now with a magnetic field in the x-direction $\phi_2/\phi_0 = 0.05$. d) Same as (b), but now with a magnetic field in the x-direction $\phi_2/\phi_0 = 0.05$, and y-direction $\phi_3/\phi_0 = 0.01$.

2.3 Stacks of quantum Hall layers

With these results in hand, we next introduce our main result: the possibility to engineer an inversion symmetry protected second-order topological insulator in stacks of doped quantum Hall layers with a honeycomb lattice structure. To show this, we first recall that the quantum Hall effect on the honeycomb lattice exhibits a zeroth Landau level above (below) which the total Chern number $\mathcal{C} = +1(-1)$ for relatively weak magnetic fluxes per plaquette [see Fig. 2.3]. This also implies that the sign of the Hall conductance is opposite in p- and n-doped layers. We then take advantage of this property to realize a quantum Hall analogue of the quantum anomalous Hall model introduced above. For the intralayer part of the Hamiltonian we thus consider layers with an alternating bias $\pm V_0$. The corresponding Hamiltonian is then

$$\mathcal{H}_{\parallel} = -t \sum_{\langle i,j\rangle,\alpha} c^{\dagger}_{i,\alpha} c_{j,\alpha} + V_0 \sum_{i,\alpha} (-1)^{\alpha} c^{\dagger}_{i,\alpha} c_{i,\alpha}.$$

The effect of the perpendicular magnetic field is taken into account via the usual Peierls substitution $t \to t\, \mathrm{e}^{ie \int d\mathbf{s}\cdot\mathbf{A}/\hbar}$, where $d\mathbf{s}$ is the line integral between the bonds, e is the electron charge, and we took the vector potential in the Landau gauge $\mathbf{A} = (-By, 0, 0)$ with B the magnetic field strength. The interlayer Hamiltonian can be taken to be the same as in Eq. (2.1) when considering the buckled honeycomb layers realized in silicene [44]. However, to describe stacks of graphene layers we will consider a mirror-symmetric interlayer Hamiltonian of the form $\mathcal{H}_{\perp} = -t_z \sum_{\alpha} c^{\dagger}_{i,\alpha} c_{i,\alpha+1} + h.c.$ [c.f. Fig. 2.4(a)].

Since the external perpendicular magnetic field does not break the mirror symmetry in the stacking direction, we expect the presence of protected surface Dirac cones inside the bulk band gap $\propto V_0$. This is verified in Fig. 2.4(b) where we show the energy spectrum for stacks of zigzag terminated ribbons with an odd number of layers. Note that due to the remaining chiral symmetry of our microscopic tight-binding model the surface energy spectrum features Dirac nodal lines. which underline the absence of an effective interlayer coupling between the quantum Hall edge states.

In order to drive the system from a mirror Chern insulating phase to a second-order topological insulating phase, we next introduce an additional component of the magnetic field in the layer plane, which breaks the mirror

	Γ	M_1	M_2	M_3	A	L_1	L_2	L_3
+1	5	3	3	3	3	3	3	3
-1	1	3	3	3	3	3	3	3

Table 2.1: Inversion eigenvalues at half-filling at inversion-symmetric points in the Brillouin zone for $\phi/\phi_0 = 1/3$, $V_0 = 0.8t$.

symmetry in the stacking direction but preserves the bulk inversion symmetry of our AA-stacked graphene multilayers. Fig. 2.4(c) shows the edge spectrum when superimposing a finite component of the magnetic field parallel to the zigzag direction. The nodal degeneracies are removed but the surface still features an unprotected surface Dirac cone signalling a coupling between the quantum Hall edge states that is still effectively mirror symmetric. We get rid of this additional unprotected degeneracy by further adding a magnetic field component in the layer plane but perpendicular to the zigzag direction. This leads to surface gap openings with the edge spectrum [c.f. Fig. 2.4(d)] that is now composed of surface Landau levels and additionally features chiral states localized at opposite hinges. Moreover, the chiral hinge states at positive and negative energies are separated by a zeroth surface Landau level, and therefore live on different hinges [see Appendix A]. As discussed above, this change in the location of the chiral hinge modes by tuning the Fermi level is perfectly compatible with the topology of our system.

Finally, to verify the bulk non-trivial topology of our microscopic tight-binding model, we have computed the multiplicities of the inversion symmetry eigenvalues at the inversion-symmetric momenta of the BZ [see Table 2.1]. When computing Eq. (2.2) we then find a non- trivial value of the $\mathbb{Z}_2$ topological invariant in perfect agreement with the foregoing analysis. As shown in Appendices B and C, the existence of an inversion-symmetric second-order topological insulator in stacks of doped quantum Hall layers is not restricted to graphene layers but can be also extended to buckled structures, e.g. silicene, and even multilayer phosphorene [45], thus strengthening the generality of our design principle.

2.4 Conclusion

To sum up, we have proved the existence of a second-order topological insulator protected by inversion symmetry using a coupled layer approach in which the layers have alternating Chern numbers. It can be derived from a parent topological mirror Chern insulator by crystalline symmetry breaking terms that retain the bulk inversion symmetry of the bulk crystal. The presence of the topologically protected chiral hinge modes can be inferred from a three-dimensional $\mathbb{Z}_2$ invariant. We have shown that a non-trivial value of this invariant can be encountered in stacks of doped honeycomb layers subject to an external magnetic field slightly tilted away from the stacking direction. The required alternating doping of the honeycomb sheets can be obtained for instance by separating the monolayers with two-dimensional polar spacers [46]. As a result, we believe that graphene, silicene, and phosphorene multilayers provide an excellent platform to engineer chiral inversion-symmetric higher-order topological insulators.

Appendix A: Localization of hinge states

In Fig. 2.5 we show the localization of hing states in alternately doped graphene layers in a canted magnetic field.

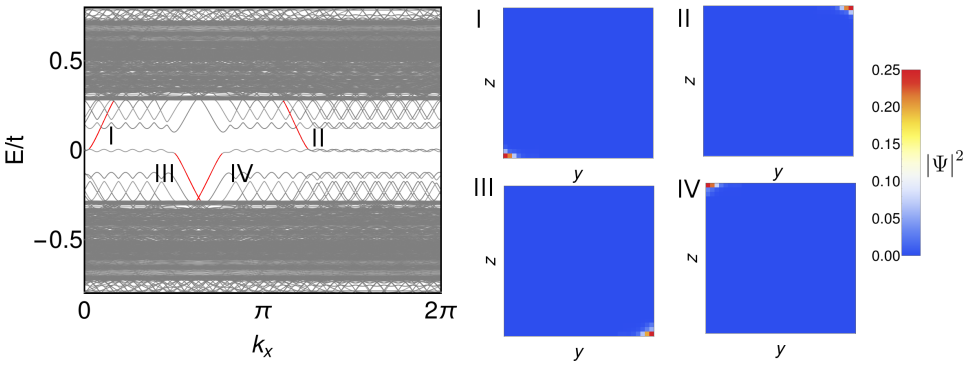

Figure 2.5: Figure showing the localization of the hinge states of stacks of alternately doped graphene layers in a canted magnetic field, in a zigzag ribbon geometry for $t/t_z = 0.2$, $\phi/\phi_0 = 1/8$, $V_0 = 0.5$, $\phi_2/\phi_0 = 0.05$ and $\phi_3/\phi_0 = 0.01$ (the same parameters as Fig. 4(c) of the main text). Going from the gap above the zeroth LL of the surface to the one below it, the chiral hinge states localize on different hinges. This realizes both inversion symmetric configurations, as alluded to in the main text.

Appendix B: Silicene multilayers

Silicene, a single layer of silicon, has a buckled honeycomb structure (see Fig. 2.6(d)). In AA stacking the interlayer coupling naturally breaks the mirror symmetry implying the existence of larger surface gaps and hence enhanced stability of the hinge states. This is demonstrated in Fig. 2.6(a)-(c) where we show the spectrum of stacked alternately doped silicene using the same parameter set adopted in the main text for the case of graphene layers. Notice that the buckled silicene structure shown in Fig. 2.6(d) leads to an interlayer Hamiltonian that can be taken in the form of Eq.(1) of the main text.

Appendix C: Multilayer phosphorene

Phosphorene, a single layer of black phosphorus, consists of phosphor atoms arranged in a puckered honeycomb lattice (see Fig. 2.7(d)), and when stacked the layers are displaced by half a unit cell in the zigzag direction. Here, we show that in principle one can realize chiral hinge states in alternately doped multilayer phosphorene. To show this we take the tight-binding model of Ref. [39] of the main text, and apply alternating doping and a magnetic field. To simplify the calculation we use only the three dominant hopping terms (c.f. Fig. 2.7(d)), which give a qualitatively correct energy spectrum in the asbence of external magnetic fields. The spectrum for a zigzag ribbon of multilayer phosphorene is shown in Figs. 2.7(a)-(c), for a perpendicular and canted magnetic field. Again we see the appearance of a Dirac cone, and chiral edge states when completely canting the magnetic field. Phosphorene has a gap of about 2 eV, hence one would need to apply much stronger doping than in graphene or silicene. Although this could be impractical, the results show the generality of our approach in engineering chiral hinge states.

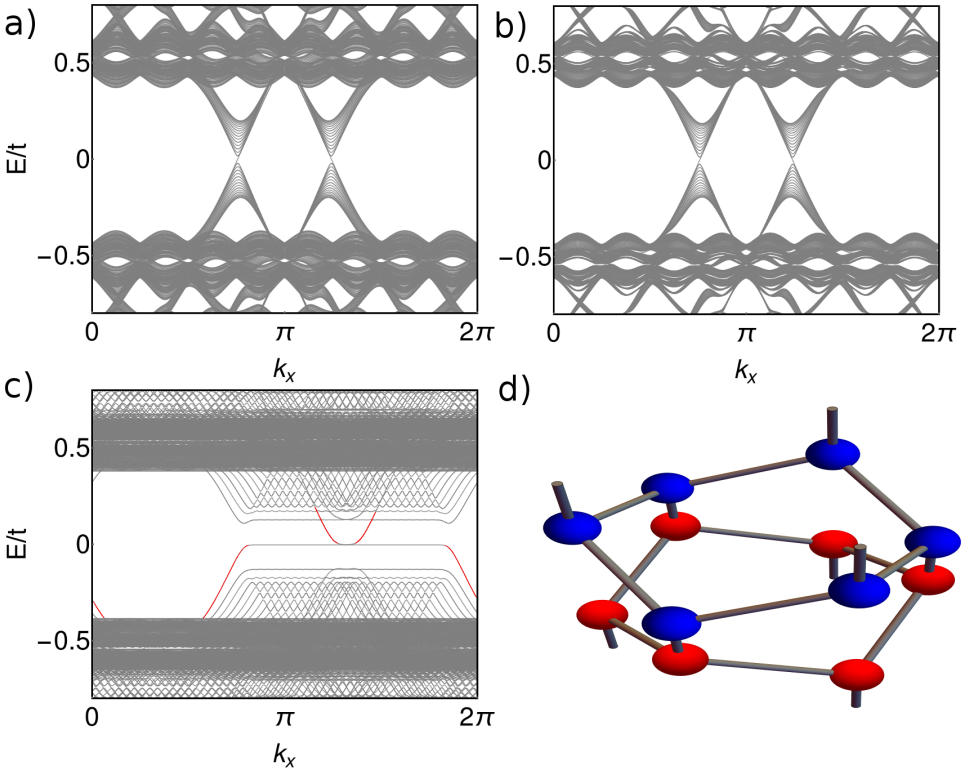

Figure 2.6: Spectra for a zigzag ribbon of alternately doped stacks of silicene with a) $t/t_z = 0.2$, $\phi/\phi_0 = 1/8$, $V_0 = 0.5$ and $\phi_2/\phi_0 = \phi_3/\phi_0 = 0$, where ϕ/ϕ_0, ϕ/ϕ_1 and ϕ/ϕ_2 are the flux per plaquette in the z, x and y direction respectively. (b) Same as (a), but now with a magnetic field in the x-direction $\phi_2/\phi_0 = 0.05$. c) Same as (a), but now with a magnetic field in the x-direction $\phi_2/\phi_0 = 0.05$, and y-direction $\phi_3/\phi_0 = 0.01$. d) Schematic side-view of an AA stacked buckled honeycomb lattice. In the first layer the A sublattice is connected to the next layer, while in the second layer the B sublattice is connected to the next layer.

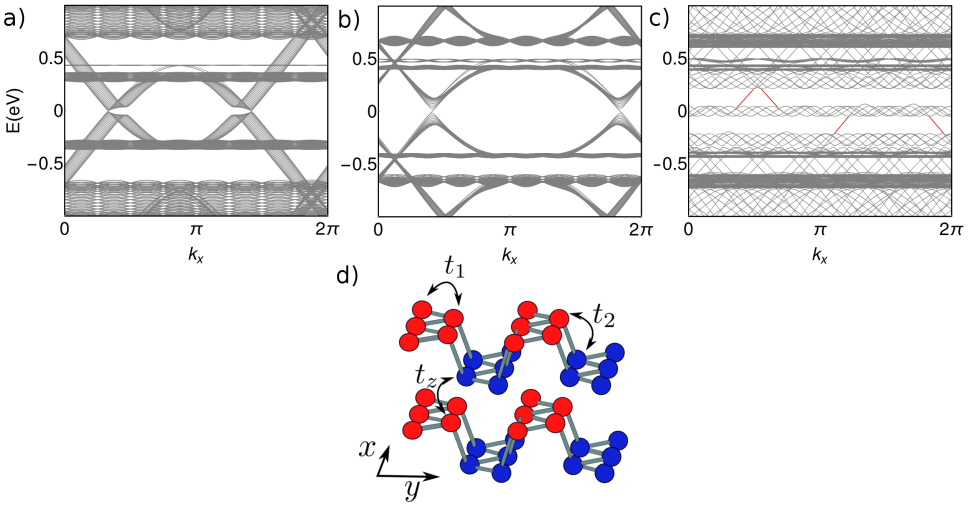

Figure 2.7: a) Spectrum for alternately doped stacked phosphorene with $t_1 = -1.486$ eV, $t_2 = 3.729$ eV, $t_z = 0.524$ eV, $\phi/\phi_0 = 1/8$, $V_0 = 2.1$ and $\phi_2/\phi_0 = \phi_3/\phi_0 = 0$, where ϕ/ϕ_0, ϕ/ϕ_1 and ϕ/ϕ_2 are the flux per plaquette in the z, x and y direction respectively. b) Same as (a), but now with a magnetic field in the x-direction $\phi_2/\phi_0 = 0.02$. c) Same as (a), but now with a magnetic field in the x-direction $\phi_2/\phi_0 = 0.02$, and y-direction $\phi_3/\phi_0 = 0.04$. d) Schematic figure of multilayer phosphorene.

3 Classification of crystalline insulators without symmetry indicators

Atomic and fragile topological phases in twofold rotation symmetric systems

Since the discovery of the quantum Hall effect [1], and its theoretical explanation in terms of the topological properties of the Landau levels [47–49], topological phases of matter have become a rich playground for the theoretical prediction and experimental verification of new quantum phenomena. From the birth of topological insulators [2–4, 41, 50–53], to topological superconductors supporting Majorana zero modes [54–58], to topological semimetals [32, 59–69], new types of topological phases keep arising. It is fair to say that the major theoretical effort in the field has been to classify, using appropriate mathematical schemes, all possible topologically distinct gapped phases and subsequently relate them to topological indices. In the presence of internal symmetries – time-reversal, particle-hole and chiral symmetry – alone, the classification of free-fermion gapped phases has been obtained in all ten symmetry classes and arbitrary number of dimensions [70–72]. The corresponding phases with non-trivial topology feature, by the bulk-boundary correspondence, protected gapless modes that are anomalous [11, 12]. The chiral (helical) edge states of quantum (spin) Hall insulators, as well as the single surface Dirac cones of strong three-dimensional topological insulators violating the fermion doubling theorem, are prime realizations of such anomalies.

In crystalline systems characterized by an additional set of spatial symmetries, new topologically distinct phases emerge [13, 14, 73–75]. The non-trivial topology of a system is then manifested in the appearance of anomalous gapless surface modes, which are present only on surfaces that are left invariant under the protecting spatial symmetry and violate stronger versions of the fermion doubling theorem [16, 25]. Furthermore, crystalline symmetries can also yield non-trivial topological phases, dubbed higher-

order topological states [8, 9, 17, 19–23, 26, 26–29, 76–81], characterized by conventional gapped surfaces but with gapless anomalous one-dimensional modes at the hinges connecting two surfaces related by the protecting spatial symmetry.

As long as insulating systems are concerned, the existence of anomalous surface or hinge boundary modes is deeply connected to the fact that non-trivial topological phases cannot be adiabatically connected to atomic insulators, whose insulating nature can be understood considering electrons as trapped classical point particles. In other words, a topological non-trivial insulator only arises when there is an obstruction in describing the system using an atomic picture. Therefore, the ground state of a topological non-trivial insulator cannot be represented using exponentially localized Wannier functions respecting the internal and/or the set of spatial symmetries of the system [82]. This obstruction to a "Wannier-representability", the classification in terms of topological invariants and the existence of gapless anomalous boundary modes can be formulated in a unique consistent framework for systems equipped only with internal symmetries [82, 83]. When adding spatial symmetries, however, different complications arise.

First, distinct atomic insulators, which are by definition topologically trivial, generally possess different crystalline topological invariants. This, in turn, requires a careful inspection of such topological indices to identify the criteria dictating the appearance of topologically non-trivial crystalline phases. Second, there can exist "non-Wannierazible" topological phases in crystals which do not possess boundaries that are left invariant under the protecting spatial symmetry. As a result, the surfaces of these systems are fully gapped even if the bulk is topological. Notwithstanding these complications, substantial progresses has been made with the theory of topological quantum chemistry [5] and that of symmetry-based indicators [10, 84, 85], which allows one to discriminate all different atomic insulators from genuine topological non-trivial phases using the spatial symmetry character of the valence bands and their connectivity throughout the Brillouin zone. Combining these theories with density-functional-theory calculations has very recently led to catalogues containing a huge number of topological materials [86–88].

Nonetheless, there exist topological phases that are not detectable using the symmetry labels of the valence bands. An extreme case is a system with only translation symmetry: it can be in a topological "tenfold-way"

phase due to its internal symmetries, but it is signaled as being topologically trivial using spatial symmetry indicators. More importantly, there can exist topological crystalline phases in low-symmetric crystals that are neither characterizable by the symmetry content of the valence bands nor by the tenfold-way [89]. To date, these phases lack any classification and consequently any material realization.

In this work, we achieve the first of such classifications. Specifically, we consider the paradigmatic example of two-dimensional crystals with twofold rotation symmetry, *i.e.* in the wallpaper group $p2$, where the gapped phases of time-reversal symmetric (non-magnetic) systems with sizable spin-orbit coupling cannot be classified with the symmetry data of the valence bands. Instead, we construct Berry phase related $\mathbb{Z}_2$ invariants to first isolate and remove topologically non-trivial quantum spin-Hall phases from the set of distinct gapped phases. Thereafter, we enumerate all distinct atomic insulating phases and classify them using a trio of $\mathbb{Z}_2$ topological invariants. Using our Berry phase based classification, we are able to determine: *i)* in systems with two occupied valence bands, the existence of topological non-trivial crystalline phases similar in nature to the fragile phases detected by symmetry eigenvalues in other wallpaper groups [6, 7, 90, 91]. *ii)* with four occupied valence bands, the emergence of an additional fragile topological crystalline phase, whose possible existence has been overlooked so far. To underline the importance of these findings, we point out that topological crystalline phases of the fragile type have been predicted to occur in magic-angle twisted bilayer graphene [92–96].

This chapter is organized as follows. In Section 3.1 we first present the example of a time-reversal symmetric one-dimensional atomic chain where the symmetry character of the bands is not able to classify the distinct gapped phases, and show that such a classification becomes instead possible introducing a "partial" Berry phase $\mathbb{Z}_2$ invariant. We then show in Section 3.2 that these $\mathbb{Z}_2$ invariants can be also defined on high-symmetry lines in the Brillouin zone of a two-dimensional crystal in the $p2$ wallpaper group, and can be used to first remove topological phases protected by time-reversal symmetry, and then classify atomic and fragile topological phases when two valence bands are occupied. In Section 3.3 we introduce a new $\mathbb{Z}_2$ invariant corresponding to a "nested" quantized partial Berry phase, thanks to which we are able to diagnose the atomic insulating phases realized with four occupied valence bands and establish the existence of our novel $N_F = 4$ fragile

topological insulator. The trio of $\mathbb{Z}_2$ invariants is then used to classify all atomic insulating phases for a generic number of occupied Kramers pairs of bands in Section 3.4. Finally, we present our conclusions and comment on extensions of our work in Section 3.5.

3.1 Motivation and warmup in 1D: mirror-symmetric chains

We start out by considering an atomic chain of spin one-half electrons with time-reversal symmetry and an additional mirror symmetry with respect to a one-dimensional (1D) mirror point. Moreover, we will assume inversion symmetry to be explicitly broken. The space group $\mathcal{G}$ for this atomic chain is generated by

$$\mathcal{G} = \langle \{E|\mathbf{t}\}, \{\mathcal{M}|0\} \rangle,$$

where E is the identity, $\mathbf{t}$ the lattice translation vector, and $\mathcal{M}$ the mirror symmetry with respect to the 1D mirror point. In the unit cell of this 1D crystal, there are two distinct maximal Wyckoff positions whose site symmetry group, or stabilizer group, is isomorphic to the point group $\mathcal{C}_s$. The first, labelled $1a$, has coordinate $x = 0$ and corresponds to the origin of the unit cell. Its stabilizer group is simply generated by $\{\mathcal{M}|0\}$. Similarly, the second maximal Wyckoff position, labelled $1b$, corresponds to the edge of the unit cell with coordinate $x = 1/2$ in units of the lattice constant, and its stabilizer group is generated by $\{\mathcal{M}|1\}$, which is also isomorphic to $\mathcal{C}_s$. For all other positions in the unit cell, the stabilizer group only contains the identity. Therefore these Wyckoff positions have multiplicity two and coordinates $(x, -x)$. Let us now enumerate the elementary band representations [97] for exponentially localized Wannier functions (WFs) sitting at the maximal Wyckoff positions $1a$ and $1b$. They can be induced by considering that in reciprocal space there are two mirror-symmetric momenta in the Brillouin zone (BZ), *i.e.* $\Gamma = 0$ and $X = \pi$. Moreover, since the stabilizer group of $1a$ does not contain any translation, the mirror eigenvalues $\pm i$ at Γ and X must be identical. On the contrary, the stabilizer group of $1b$ contains a lattice translation of half a unit cell and therefore the mirror eigenvalues at Γ and X are opposite. The elementary band representations can then be summarized as in Table 3.1. Note that the "composite" band representation for two

Wyckoff position	Representation	Γ	X
$1a$	$\rho_i^{1a} \uparrow \mathcal{G}$	i	i
	$\rho_{-i}^{1a} \uparrow \mathcal{G}$	$-i$	$-i$
$1b$	$\rho_i^{1b} \uparrow \mathcal{G}$	i	$-i$
	$\rho_{-i}^{1b} \uparrow \mathcal{G}$	$-i$	i

Table 3.1: Elementary band representation for the one-dimensional space group of a mirror symmetric chain. The first column indicates the maximal Wyckoff positions. The second column the corresponding induced band representation, and the last two columns the mirror eigenvalues at the center and edge of the 1D BZ.

symmetric WFs [8] at the same position with opposite mirror eigenvalues $\pm i$ have a representation content in momentum space that is independent on whether they are centered at $1a$ or $1b$. This yields the equivalence $\rho_i^{1a} \oplus \rho_{-i}^{1a} \uparrow \mathcal{G} \simeq \rho_i^{1b} \oplus \rho_{-i}^{1b} \uparrow \mathcal{G}$, which simply states that the corresponding pairs of exponentially localized WFs can be moved anywhere along the line between the $1a$ and the $1b$ sites in opposite directions.

The aforementioned composite band representation becomes a physical elementary band representation (PEBR) [5] when time-reversal symmetry Θ is taken into account. This is because Θ requires the complex irreducible one-dimensional representations at Γ and X to double. The corresponding pairs of energy bands, however, do not derive from Wannier states with charge centers at arbitrary positions along the chain. Kramers theorem indeed guarantees that exponentially localized WFs come in Kramers degenerate pairs, in which each pair has the same center. Moreover, while an even number of Wannier Kramers pairs centered at the maximal Wyckoff positions $1a$ or $1b$ can be freely moved away without breaking either the mirror or time-reversal symmetry, with an odd number of Wannier Kramers pairs sitting at $1a$ or $1b$ the center of at least one pair of Wannier states is unmovable [29]. Put differently, the parity of Wannier Kramers pairs centered at the maximal Wyckoff positions $1a$ and $1b$ represent stable topological $\mathbb{Z}_2$ indices characterizing a one-dimensional time-reversal and mirror-symmetric insulator. More importantly, these stable topological indices cannot be read off from the symmetry character of the bands since only one PEBR exists. The discrepancy between the existence of real space stable topological indices and the absence of distinct PEBRs can be overcome using the recent finding that

Kramers pairs of bands in a mirror symmetric [98], or equivalently $\mathcal{C}_2$ twofold rotation symmetric [99], atomic chain possess a $\mathbb{Z}_2$ topological index defined in terms of the "partial" polarization introduced by Fu and Kane [100], which is quantized by the presence of these point group symmetries. In its $U(N_F)$ gauge invariant form it can be written as

$$\nu^{\mathcal{M}} := \frac{1}{\pi}\left[\int_0^{\pi} dk\, \mathrm{Tr}\, \mathcal{A}(k) + i \log \frac{\mathrm{Pf}\,[w(\pi)]}{\mathrm{Pf}\,[w(0)]}\right] \mathrm{mod}\ 2. \tag{3.1}$$

In the equation above, we have introduced the non-Abelian Berry connection $\mathcal{A}_{m,n}(k) = \langle u_m(k)|\, i\partial_k\, |u_n(k)\rangle$, and the sewing matrix $w_{m,n}(k) = \langle u_m(-k)|\, \Theta\, |u_n(k)\rangle$ that is antisymmetric at the Γ and X points and hence characterized by its Pfaffian $\mathrm{Pf}(w)$. The $\mathbb{Z}_2$ invariant defined above can be related to the charge centers of the Wannier Kramers pairs by introducing the unitary Wilson loop operator [83, 101]

$$\mathcal{W}_{k+2\pi\leftarrow k} = \overline{\exp}\left[i\int_k^{k+2\pi} \mathcal{A}(k')dk'\right], \tag{3.2}$$

where $\overline{\exp}$ denotes path ordering of the exponential while k is the Wilson loop base point. The eigenvalues of the Wilson loop operator, $\exp(2\pi i\, \nu_j)$, j labelling the occupied bands, are independent of the base point k and uniquely determine the Wannier centers ν_j. The presence of mirror symmetry translates into a chiral symmetry for the Wilson loop eigenvalues [7], thus implying that the Wannier centers are restricted to the values $\nu_j = 0, 1/2$ or to "unpinned" pairs $(\bar{\nu}, -\bar{\nu})$. Moreover, time-reversal symmetry guarantees that each Wilson loop eigenvalue has to be doubly degenerate. The concomitant presence of mirror and time-reversal symmetry therefore yields $\sum_j \nu_j \bmod 1 \equiv 0$, and consequently $\sum_j \nu_j \bmod 2 \equiv \nu^{\mathcal{M}}$ can only assume the values 0 and 1. Knowing the relation between the $\mathbb{Z}_2$ topological invariant and the Wannier centers, we can straightforwardly classify the insulating states realized in a one-dimensional mirror-symmetric atomic chain. In fact, with a total number of occupied bands $N_F = 4n + 2$, n being integer, an insulating atomic chain for which $\nu^{\mathcal{M}} = 0$ ($\nu^{\mathcal{M}} = 1$) will be characterized by the presence of an odd number of Wannier Kramers pairs at $1a$ ($1b$). If instead $N_F = 4n$ the system can be described in terms of exponentially localized Wannier functions with an even or odd number of Kramers degenerate pairs centered at $1a$ *and* $1b$ depending on whether $\nu^{\mathcal{M}} = 0$ or $\nu^{\mathcal{M}} = 1$,

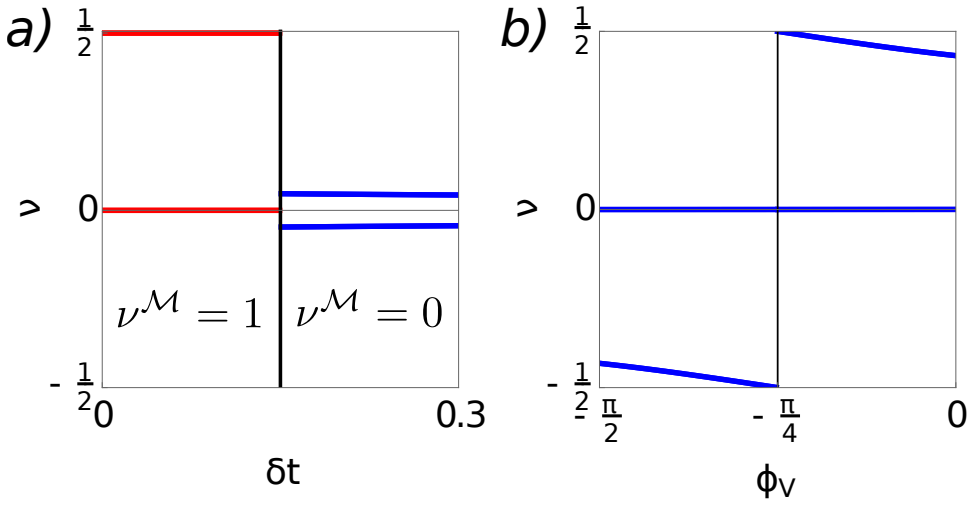

Figure 3.1: Evolution of the Wilson loop eigenvalues for a mirror and time-reversal symmetric Aubry-André-Harper model [Eq. (3.3)] at $N_F = 4$ by (a) sweeping the dimerization hopping amplitude δt while preserving mirror symmetry ($\phi_V = -\pi/4$) and (b) changing the phase ϕ_V away from the mirror-symmetric point for $\delta t = -0.25t_0$. Other parameters are set to $\phi_t = \phi_\lambda = \pi$, $\lambda_0 = 0.5t_0$, $\delta\lambda_0 = -0.3t_0$ and $\delta V = t_0$.

respectively.

To verify this relation between the $\mathbb{Z}_2$ topological invariant $\nu^{\mathcal{M}}$ and the Wannier centers distribution, we have computed the Wilson loop spectrum for a time-reversal and mirror symmetric one-dimensional spinful Aubry-André-Harper [102–104] model described by the Hamiltonian [98],

$$\begin{aligned}\mathcal{H} &= \sum_{j,\sigma}\left[t_0 + \delta t\cos\left(\pi j + \phi_t\right)\right] c^\dagger_{j+1,\sigma} c_{j,\sigma} \\ &\quad + i\sum_{j,\sigma,\sigma'}\left[\lambda_0 + \delta\lambda\cos\left(\pi j + \phi_\lambda\right)\right] c^\dagger_{j+1,\sigma} s^y_{\sigma\sigma'} c_{j,\sigma'} \\ &\quad + \sum_{j,\sigma}\left[V_0 + \delta V\cos\left(j\pi/2 + \phi_V\right)\right] c^\dagger_{j,\sigma} c_{j,\sigma} + \text{H.c.},\end{aligned}$$

where $c^\dagger_{j,\sigma}$ is the creation operator for an electron at site j with spin σ

($\sigma = \uparrow, \downarrow$), and s^i are the conventional Pauli matrices. The Hamiltonian contains harmonically modulated nearest-neighbor hopping, spin-orbit coupling and onsite potentials of amplitudes δt, $\delta\lambda$, and δV, and phases ϕ_t, ϕ_λ and ϕ_V. The periodicities of the modulated hopping and spin-orbit coupling have been chosen to be of two lattice sites while the periodicity of the onsite potential is four lattice sites. Moreover, t_0, λ_0 and V_0 are the site-independent amplitudes of the hopping, spin-orbit coupling and on-site potential. The model possesses time-reversal symmetry whereas mirror symmetry is preserved only for specific values of the phases $\phi_{t,\lambda,V}$.

For the mirror-symmetric model, the half-filled $N_F = 4$ insulating state undergoes a band gap closing-reopening, accompanied by a change of the $\mathbb{Z}_2$ topological invariant, by sweeping the strength of the nearest-neighbor hopping amplitude δt.

As explicitly shown in Fig. 3.1(a), the insulating state can be described in terms of two Wannier Kramers pairs centered at $1a$ and $1b$ in the $\nu^{\mathcal{M}} = 1$ region. On the contrary, a $\nu^{\mathcal{M}} = 0$ value of the topological invariant implies the existence of two Wannier pairs centered at two mirror related, non-maximal Wyckoff positions in the unit cell. Moreover, by breaking the mirror symmetry of the model [see Fig. 3.1(b)] the position of the exponentially localized Wannier function can be freely moved at arbitrary positions in the unit cell in agreement with the fact that the space group in this case only contains the identity. Finally, we emphasize that the change of the $\mathbb{Z}_2$ invariant is associated with a band gap closing-reopening occurring at unpinned points in the BZ [98], which is a restatement of the fact that the topological index characterizing a mirror and time-reversal symmetric insulating chain cannot be inferred from the symmetry character of the occupied bands.

3.2 Wallpaper group $p2$: insulators with two occupied bands

Having established the $\mathbb{Z}_2$ classification of mirror and time-reversal symmetric insulating chains in the absence of symmetry indicators, we next consider the main focus of this work: two-dimensional (2D) crystals possessing a $\mathcal{C}_2$ twofold rotation symmetry. The smallest two-dimensional wallpaper group containing $\mathcal{C}_2$ is $p2$. It has four maximal Wyckoff positions labelled as $1a = \{0,0\}$, $1b = \{1/2,0\}$, $1c = \{0,1/2\}$ and $1d = \{1/2,1/2\}$. Their

Wyckoff position	Representation	Γ	X	Y	M
$1a$	$\rho_{i}^{1a}\uparrow\mathcal{G}$	i	i	i	i
	$\rho_{-i}^{1a}\uparrow\mathcal{G}$	$-i$	$-i$	$-i$	$-i$
$1b$	$\rho_{i}^{1b}\uparrow\mathcal{G}$	i	$-i$	i	$-i$
	$\rho_{-i}^{1b}\uparrow\mathcal{G}$	$-i$	i	$-i$	i
$1c$	$\rho_{i}^{1c}\uparrow\mathcal{G}$	i	i	$-i$	$-i$
	$\rho_{-i}^{1c}\uparrow\mathcal{G}$	$-i$	$-i$	i	i
$1d$	$\rho_{i}^{1d}\uparrow\mathcal{G}$	i	$-i$	$-i$	i
	$\rho_{-i}^{1d}\uparrow\mathcal{G}$	$-i$	i	i	$-i$

Table 3.2: Elementary band representation for the $p2$ wallpaper group $\mathcal{G} = \langle\{E|\mathbf{t}\}, \{\mathcal{C}_2|0\}\rangle$. The first column indicates the maximal Wyckoff positions; the second column the corresponding induced band representation, and the last two columns the $\mathcal{C}_2$ eigenvalues at the $\Gamma = \{0,0\}$, $X = \{\pi,0\}$, $Y = \{0,\pi\}$ and $M = \{\pi,\pi\}$ points in the BZ. In time-reversal symmetric systems, the PEBRs obey the equivalence $\rho^{1a}\uparrow\mathcal{G} \simeq \rho^{1b}\uparrow\mathcal{G} \simeq \rho^{1c}\uparrow\mathcal{G} \simeq \rho^{1d}\uparrow\mathcal{G}$.

stabilizer group is isomorphic to $\mathcal{C}_2$, which implies that in systems with time-reversal symmetry the induced band representations have the same symmetry character [cf. Table 3.2].

However, the parity of the Wannier Kramers pairs centered at $1a$,$1b$,$1c$,$1d$ still represent real space stable topological indices that discriminate between non-equivalent atomic insulating states. To classify these different atomic insulators, we first use the fact that in the BZ of a twofold rotation symmetric crystal, the $\mathcal{C}_2$ symmetry constraint $\mathcal{C}_2^{-1}\mathcal{H}(\mathbf{k})\mathcal{C}_2 = \mathcal{H}(-\mathbf{k})$ is equivalent to a one-dimensional mirror symmetry constraint along the time-reversal invariant non-contractible loop lines $k_{1,2} \equiv 0$, and $k_{1,2} = \mathbf{G}_{1,2}/2$. Therefore, we can in principle define a quartet of $\mathbb{Z}_2$ invariants $\left\{\nu^{\mathcal{M}}_{k_1=0}; \nu^{\mathcal{M}}_{k_1=\mathbf{G}_1/2}; \nu^{\mathcal{M}}_{k_2=0}; \nu^{\mathcal{M}}_{k_2=\mathbf{G}_2/2}\right\}$ [c.f. Fig. 3.2]. These topological indices are not all independent, however, since the differences $\nu^{\mathcal{M}}_{k_{1,2}=\mathbf{G}_{1,2}/2} - \nu^{\mathcal{M}}_{k_{1,2}=0}$ can be related [105] to the Fu-Kane-Mele (FKM) $\mathbb{Z}_2$ topological invariant [3, 100] characterizing a time-reversal invariant 2D topological insulator. This follows from the fact that $\nu^{\mathcal{M}}_{k_{1,2}=\mathbf{G}_{1,2}/2} - \nu^{\mathcal{M}}_{k_{1,2}=0}$ keeps track of the evolution of the Wannier centers during a time-reversal pumping process [83]. Therefore, the condition $\nu^{\mathcal{M}}_{k_{1,2}=\mathbf{G}_{1,2}/2} - \nu^{\mathcal{M}}_{k_{1,2}=0} = 1 \bmod 2$ immediately implies

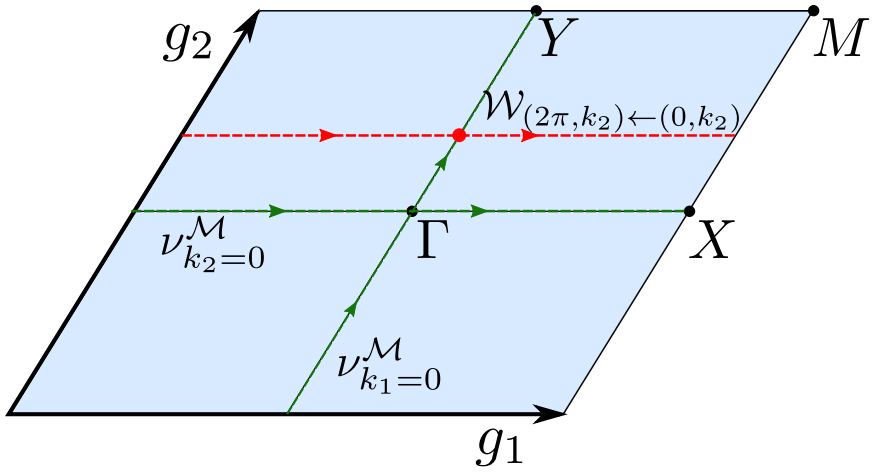

Figure 3.2: Schematic drawing of a $\mathcal{C}_2$ symmetric Brillouin zone spanned by reciprocal lattice vectors g_1 and g_2 with high-symmetry points Γ, X, Y and M. The contours along which the partial Berry phases γ_1^I and γ_2^I are calculated are drawn in green, a typical Wilson loop operator contour, discussed in the main text, is drawn in red.

a quantum spin Hall (QSH) insulating state. When dealing with insulating crystalline systems without anomalous edge states (trivial FKM invariant), we are thus left with a $\mathbb{Z}_2 \times \mathbb{Z}_2$ classification [106], which, as we will show below, is only able to diagnose the atomic insulating states when one Kramers pair of bands is occupied.

The assertion above can be immediately proved by using the fact that for an atomic insulator with two occupied bands, the exponentially localized Wannier Kramars' pair must be centered at one of the maximal Wyckoff positions. Hence, the corresponding center of charge already provides a $\mathbb{Z}_2 \times \mathbb{Z}_2$ classification. Furthermore, the center of charge can be straightforwardly connected to the doublet of one-dimensional invariants $\nu^{\mathcal{M}}_{k_{1,2}=0}$ as follows. Let us consider the Wilson loop operator in the e_1 direction $\mathcal{W}_{(k_1+2\pi,k_2)\leftarrow(k_1,k_2)}$ where (k_1, k_2) is the base point. Its eigenvalues $\exp[2\pi i\ \nu_j(k_2)]$ $(j = 1, 2)$ depend on the k_2 coordinate of the Wilson loop base point and the corresponding phases $\nu_j(k_2)$ are the centers of the one-dimensional hybrid Wannier functions [c.f. Fig. 3.2]. Due to time-reversal symmetry the Wannier bands realize a Kramers related pair [c.f. Appendix A], and therefore can be

Wyckoff position	$\nu^{\mathcal{M}}_{k_1=0}$	$\nu^{\mathcal{M}}_{k_2=0}$
$1a$	0	0
$1b$	0	1
$1c$	1	0
$1d$	1	1

Table 3.3: The $\mathbb{Z}_2 \times \mathbb{Z}_2$ classification of atomic insulators in the $p2$ wallpaper group with one occupied Kramers pair, *i.e.* $N_F = 2$. The first column indicates the maximal Wyckoff position, while the second and third column are the $U(2)$ gauge invariant line invariants.

split into two time-reversed channels $s = I, II$ satisfying $\nu^I(k_2) \equiv \nu^{II}(-k_2)$. The additional $\mathcal{C}_2$ rotation symmetry mandates the Wilson loop spectrum to be chiral symmetric, *i.e.* $\nu^I(k_2) \equiv -\nu^{II}(k_2)$. As a result, the center of charge of the Wannier Kramers pair in the e_1 direction is

$$\frac{1}{2\pi}\oint \nu^I(k_2)dk_2 \bmod 1 \equiv \nu^I(k_2 = 0) \bmod 1 \equiv \frac{\nu^{\mathcal{M}}_{k_2=0}}{2}.$$

Repeating the same argument using the Wilson loop operator in the e_2 direction, we therefore reach the classification of atomic insulators with one occupied Kramers pair of bands summarized in Table 3.3.

Strictly speaking, this classification does not enumerate all possible insulating phases with a trivial FKM invariant. Contrary to 1D systems where all insulating phases can be adiabatically continued to an atomic insulating phase [10], in 2D systems there can exist topologically non-trivial states that present an obstruction to a representation in terms of symmetric and exponentially localized WFs [6]. These topological phases have been dubbed "fragile" topological phases since although not admitting a Wannier representation by themselves, such a representation becomes possible when additional trivial bands are added to the system. In recent works, the existence and diagnosis of fragile topological phases [7, 95, 107] have been linked to the topological nature of disconnected PEBR's [5]. However, the defining characteristic of a fragile topological phase – the absence of a Wannier gap in the Wilson loop spectrum that consequently must display a non-trivial winding – can exist also in our low-symmetric crystal with a single unsplittable PEBR.

In fact, due to the concomitant presence of the commuting two-fold rotation symmetry and time-reversal symmetry, a crystal in the $p2$ space group is also invariant under the combined antiunitary symmetry operation $\mathcal{C}_2\Theta$ with $(\mathcal{C}_2\Theta)^2 = 1$. Assuming a periodic and smooth real gauge can be found[a], this also implies that the Wilson loop operator in the $e_{1,2}$ direction belongs to the orthogonal group $SO(2)$, with the homotopy group $\pi_1[SO(2)] = \mathbb{Z}$ guaranteeing the existence of an integer winding number invariant [108]. A $\mathcal{C}_2\Theta$-protected fragile topological phase of this kind has been first discussed in Ref. [109] and dubbed Stiefel-Whitney (SW) insulator since the parity of the winding number corresponds to the second SW class invariant. Note that for a SW insulator to exist, the total Berry phases along the $k_{1,2} \equiv 0$ lines – which correspond to the first SW class invariant in a smooth and periodic real gauge – must vanish. This constraint is immediately verified in a $\mathcal{C}_2$ crystal with time-reversal symmetry. On the other hand, time-reversal symmetry also guarantees the winding number of the Wilson loop operator to assume $2\mathbb{Z}$ values, which, in the language of Ref. [109] would imply the $\mathbb{Z}_2$ second SW class invariant to be trivial.

However, in a $N_F = 2$ insulator with time-reversal symmetry a Wilson loop spectrum winding an even number of times cannot be unwinded. Consider the Wilson loop operator $\mathcal{W}_{(k_1,k_2+2\pi)\leftarrow(k_1,k_2)}$ and assume, for instance, that the line invariant $\nu^{\mathcal{M}}_{k_1=0} = 0$. The Wilson loop spectrum has to display two symmetry enforced degeneracies at $k_1 = 0, \pi$ with the corresponding hybrid Wannier centers at $\nu = 0$. The absence of a Wannier gap also implies the existence of two degeneracies at time-reversal related momenta $\bar{k}_1, -\bar{k}_1$ where the hybrid Wannier center $\nu = 1/2$. The $\mathcal{C}_2\Theta$ symmetry mandates that these unpinned degeneracies can be only moved [c.f. Appendix A and Ref. [7]] pairwise (as required by time-reversal), and consequently cannot be destroyed. Hence, the winding of the Wilson loop spectrum is robust, which allows for the definition of a fragile topological phase in insulators with one occupied Kramers pair of bands. Furthermore, the Wilson loop winding can occur independent of the $\mathbb{Z}_2$ line invariants, thus suggesting that the complete classification in systems with a trivial FKM invariant is $\mathbb{Z}_2 \times \mathbb{Z}_2 \times \mathbb{Z}_2$, where the third $\mathbb{Z}_2$ invariant discriminates between gapped and winding Wilson loop spectra.

To verify the existence of the fragile topological phase discussed above,

[a] A real gauge can be formulated as $\mathcal{C}_2\Theta\,|\psi\rangle = |\psi\rangle$.

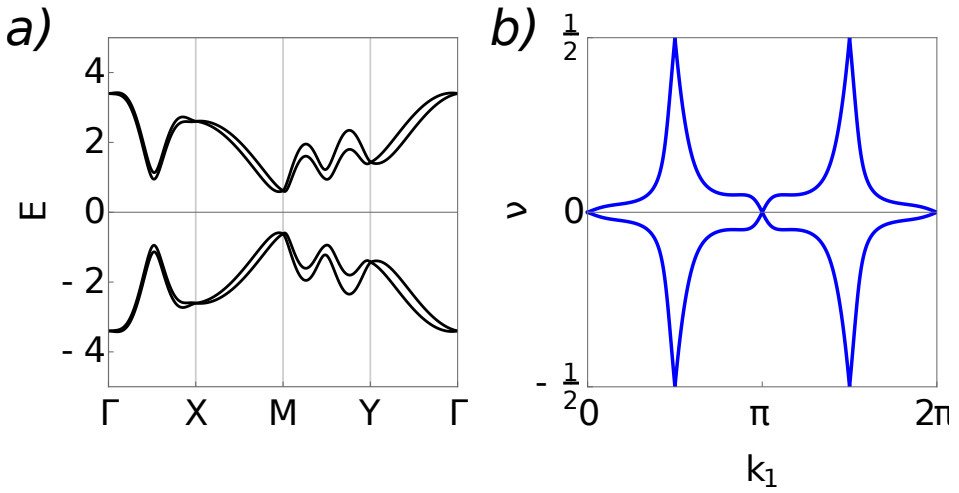

Figure 3.3: (a) Band structure of the $N_F = 2$ fragile topological insulator with twofold rotation and time-reversal symmetry. Energies have been measured in units of t. There are no degeneracies other than those required by time-reversal symmetry. (b) The Wilson loop spectrum along the k_1 direction for the half-filled insulating state. We have chosen the following parameter set: $t/t_2 = 0.4$; $t/t_3 = -1.6$; $\lambda/t = 0.15$.

we introduce a four-band tight-binding model on a $\mathcal{C}_3$ and mirror symmetry broken honeycomb lattice reading:

$$\begin{aligned}\mathcal{H} = &\left\{-t\left[1+\cos\left(k_y\right)+\cos\left(2k_x\right)\right]-t_2\cos\left(k_x\right)\right\}\tau_x s_0\\ &\left\{-t\left[-\sin\left(k_y\right)-\sin\left(2k_x\right)\right]-t_2\sin\left(k_x\right)\right\}\tau_y s_0\\ &-t_3\sin\left(2k_x\right)\tau_z s_z\end{aligned}$$

where t, t_2, t_3 are hopping amplitudes, the τ_i's are Pauli matrices representing an internal degree of freedom, whereas the s_i's act in spin space. The two independent spin sectors are additionally coupled by a Rashba-like term

$$\begin{aligned}\mathcal{H}_R = -i\lambda\Bigg\{&\left[-\frac{1}{2}\sin\left(k_x\right)+\sin\left(k_y\right)\right]i\tau_x s_x\\ &+\left[\frac{1}{2}-\frac{1}{2}\cos\left(k_x\right)+\cos\left(k_y\right)\right]i\tau_y s_x\Bigg\},\end{aligned}$$

with λ the corresponding hopping amplitude. This model has a full spectral gap at half-filling [see Fig. 3.3(a)], andcan be thought of as being made of two coupled Chern insulators with opposite Chern numbers $\mathcal{C} = \pm 2$, thereby respecting time-reversal symmetry. In Fig. 3.3(b) we show the Wilson loop spectrum along the k_1 direction, which displays the non-trivial winding discussed above. We close this section by emphasizing that the existence of the fragile topological phase does not strictly rely on the existence of a single PEBR. In Appendix B, we introduce a $\mathcal{C}_4$ symmetric tight-binding model on the square lattice where the $N_F = 2$ atomic insulating states can be generally represented in terms of symmetric WFs centered at the maximal Wyckoff positions $1a = \{0, 0\}$ and $1b = \{1/2, 1/2\}$, which possess distinguishable PEBRs. The symmetry content of the occupied bands of our model is compatible with an atomic insulator with a Wannier Kramers pair centered at $1b$. However, inspection of the Wilson loop spectrum firmly establishes it as being a topological insulator of the fragile type.

3.3 $\mathbb{Z}_2 \times \mathbb{Z}_2 \times \mathbb{Z}_2$ classification with $N_F = 4$: a new fragile topological phase

With the $\mathbb{Z}_2 \times \mathbb{Z}_2 \times \mathbb{Z}_2$ classification of $N_F = 2$ insulating phases in our hands, we next consider insulators with $N_F = 4$. We will follow the same strategy used in the preceding section, and enumerate and classify all the existing atomic insulating phases. It is easy to see that there exist seven distinct insulating states representable in terms of symmetric WFs. In fact, with two Wannier Kramers pair in the system, their centers will either lie at two $\mathcal{C}_2$ related non-maximal Wyckoff positions or at two distinct maximal Wyckoff positions. Therefore, the two $\mathbb{Z}_2$ line invariants $\nu^{\mathcal{M}}(k_{1,2} = 0)$ are insufficient to classify these states. Now we will show, using a procedure similar to the "nested" Wilson loop one of topological multipole insulators [17, 110], that it is possible to obtain an additional $\mathbb{Z}_2$ invariant by identifying two sectors in the Wilson loop spectrum, each of which carries its own topological content, *i.e.* its quantized partial polarization.

We recall that the essential characteristic of a generic atomic insulating state is the presence of a Wannier gap in the Wilson loop spectrum. Its chiral symmetry, dictated by the $\mathcal{C}_2\Theta$ symmetry, then allows us to distinguish two regions, one symmetrically centered around $\nu = 0$ and one symmetrically centered around $\nu = 1/2$, each possessing both twofold rotation and time-reversal symmetry, and populated by Kramers related pairs of Wannier bands. We have plotted the possible Wilson loop spectra for two Kramers pairs in Fig. 3.4, where the red bands are centered around $\nu = 0$ and the green bands around $\nu = 1/2$. The blue bands can be seen as centered around either point[b]. Obviously, the parity of the pairs of Wannier bands belonging to the gapped region centered around $\nu = 1/2$ can be linked to the line invariants $\nu^{\mathcal{M}}_{k_{1,2}=0}$. Considering for instance the spectrum of the Wilson loop $\mathcal{W}_{(k_1,k_2+2\pi)\leftarrow(k_1,k_2)}$ and further splitting the Wannier bands in two time-reversed channels, we immediately find that $\nu^{\mathcal{M}}_{k_1=0} = 0$ ($\nu^{\mathcal{M}}_{k_1=0} = 1$) if the Wilson loop spectrum region centered at $\nu = 1/2$ is populated by an even [c.f. Figs. 3(b)-(d)] (odd [c.f. Fig. 3(a)]) number of pairs of Wannier bands. Furthermore, we can obtain two distinct $\mathbb{Z}_2$ invariants for the two disconnected regions of the k_1 dependent Wilson loop spectrum as follows.

[b] Since we have to take a region symmetrically centered around $\nu = 0, 1/2$ we have to either include both or neither of the blue bands.

Let us consider the Wilson loop operator $\mathcal{W}_{(k_1,k_2+2\pi)\leftarrow(k_1,k_2)}$, choosing its base point on the time-reversal and twofold rotation symmetric line $k_2 = 0$ [c.f. Fig. 3.2]. The corresponding eigenstates $\left|\nu^j_{e_2;(k_1,0)}\right\rangle$, where the subscript e_2 specifies the k_2 direction of the Wilson loop, satisfy

$$\mathcal{W}_{(k_1,2\pi)\leftarrow(k_1,0)} \left|\nu^j_{e_2;(k_1,0)}\right\rangle = e^{2\pi i \nu_j(k_1)} \left|\nu^j_{e_2;(k_1,0)}\right\rangle,$$

and allow us to define the Wannier basis [17, 76],

$$\left|w^j_{e_2;(k_1,0)}\right\rangle = \sum_n \left|u^n_{(k_1,0)}\right\rangle \left[\nu^j_{e_2;(k_1,0)}\right]^n$$

, where $n = 1, \ldots, N_F$. Since the quantized partial polarization associated to the Bloch Hamiltonian eigenfunctions $\left|u^n_{(k_1,0)}\right\rangle$ is unchanged by a general $U(N_F)$ transformation, it follows that the $\mathbb{Z}_2$ invariant $\nu^{\mathcal{M}}_{k_2=0}$ can be equivalently computed in the Wannier band eigenbasis $\left|w^j_{e_2;(k_1,0)}\right\rangle$. More importantly, working in such a basis allows us to decompose $\nu^{\mathcal{M}}_{k_2=0}$ into two different $\mathbb{Z}_2$ invariants, which we dub as $\nu^{\mathcal{M};0}_{k_2=0}$ and $\nu^{\mathcal{M};1/2}_{k_2=0}$, corresponding to the "nested" quantized partial polarizations for the two gapped sectors of the Wilson loop spectrum (the red and green bands in Fig. 3.4, respectively). This is because, as mentioned above, the two gapped regions separately satisfy both time-reversal and twofold rotation symmetry, which guarantees that the partial polarization of the corresponding Wannier band eigenstates is quantized. Note that Wannier bands only respect twofold rotation and time-reversal symmetry when the Wilson loop base points lie on a mirror symmetric line.

Having obtained three distinct $\mathbb{Z}_2$ topological invariants, we can now classify the atomic insulating phases enumerated above. Fig. 3.4(a) schematically shows the k_1-dependent Wilson loop spectrum when the two gapped sectors are each populated with one pair of Wannier bands, and thus $\nu^{\mathcal{M}}_{k_1=0} = 1$. The gapped sector centered around $\nu = 0$ is further characterized by the $\mathbb{Z}_2$ invariant $\nu^{\mathcal{M};0}_{k_2=0}$, and its value dictates whether the Wannier Kramers pair is centered at the maximal Wyckoff position $1a$ ($\nu^{\mathcal{M};0}_{k_2=0} = 0$) or $1b$ ($\nu^{\mathcal{M};0}_{k_2=0} = 1$). The same argument can be applied to the gapped sector centered at $\nu = 1/2$ to set apart Wannier Kramers pairs centered at $1c$ ($\nu^{\mathcal{M};1/2}_{k_2=0} = 0$) and $1d$

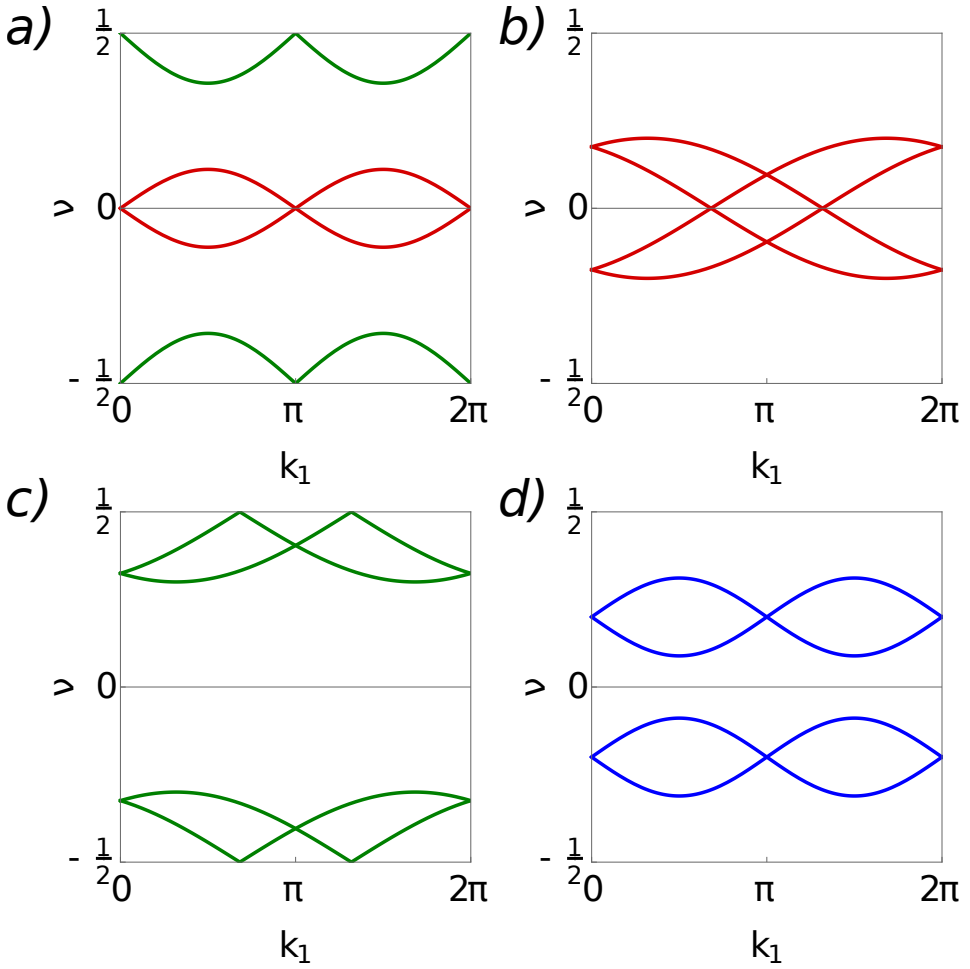

Figure 3.4: Schematic drawings of the Wilson loop spectra for the $N_F = 4$ atomic insulating states in the $p2$ wallapaper group. Panel (a) corresponds to four different atomic insulating states, where the pair of bands around $\nu = 0$ ($\nu = 1/2$) can have a Wannier center at $1a$ or $1b$ ($1c$ or $1d$), respectively, which can be determined by calculating their nested partial polarizations. Panel (b) corresponds to an atomic insulator with Wannier Kramers pairs centered at $1a \oplus 1b$, while panel (c) is for $1c \oplus 1d$. In panel (d) the Wannier functions are centered at $\mathcal{C}_2$ related generic points in the unit cell.

Wyckoff positions	$\nu^{\mathcal{M}}_{k_1=0}$	$\nu^{\mathcal{M};0}_{k_2=0}$	$\nu^{\mathcal{M};1/2}_{k_2=0}$
$1a \oplus 1c$	1	0	0
$1a \oplus 1d$	1	0	1
$1b \oplus 1c$	1	1	0
$1b \oplus 1d$	1	1	1
$1a \oplus 1b$	0	1	0
$1c \oplus 1d$	0	0	1
$\boldsymbol{\nu} \oplus -\boldsymbol{\nu}$	0	0	0

Table 3.4: The classification of atomic insulating states in the $p2$ wallpaper group when two occupied Kramers pairs of bands are occupied, *i.e.* $N_F = 4$. The first column indicates the centers of charge of the Wannier Kramers pairs; the second column is the $\mathbb{Z}_2$ line invariant of the full Wilson loop spectrum; the second and third columns are the invariants derived from the nested Wilson loops, which obey the sum rule $\left(\nu^{\mathcal{M};0}_{k_2=0} + \nu^{\mathcal{M};1/2}_{k_2=0}\right) \mod 2 = \nu^{\mathcal{M}}_{k_2=0}$. The last row refers to insulators where the Wannier Kramers pairs are centered at $\mathcal{C}_2$ related non-maximal Wyckoff positions.

($\nu^{\mathcal{M};1/2}_{k_2=0} = 1$). This, in turn, allows us to catalogue four distinct atomic insulating states.

Next, we consider insulating states where the Wannier bands occupy only one gapped sector of the Wilson loop spectrum, and thus $\nu^{\mathcal{M}}_{k_1=0} = 0$. Fig. 3.4(b),(c),(d) show the allowed possibilities for the Wannier bands. They can either realize a connected pair with two protected degeneracies at time-reversal related momenta $(\bar{k}_1, -\bar{k}_1)$ or can come in disconnected pairs, in which case the two pairs can be arbitrarily assigned to the $\nu = 0$ or the $\nu = 1/2$ sector. Let us first inspect the value the invariants $\nu^{\mathcal{M};0}_{k_2=0}$ ($\nu^{\mathcal{M};1/2}_{k_2=0}$) assume for the connected pair of Wannier bands shown in Fig. 3.4(b),(c). We can divide the four Wannier bands in two time-reversed channels, that each possess $\mathcal{C}_2\Theta$ symmetry. Then, an essential twofold degeneracy in one channel at $\nu = 0$ ($\nu = 1/2$) implies a π Berry phase [see Appendix A and Ref. [109]], and consequently the nested line invariant $\nu^{\mathcal{M};0}_{k_2=0}$ ($\nu^{\mathcal{M};1/2}_{k_2=0}$) is enforced to be 1. As a result, the schematic Wannier bands shown in Fig. 3.4(b),(c) correspond to the atomic insulating phase with Wannier Kramers pairs centered at $1a \oplus 1b$ and $1c \oplus 1d$ respectively. Using similar arguments, we also find

that the disconnected Wannier bands of Fig. 3.4(d) are characterized by a zero nested partial polarization [see Appendix A]. Therefore, in this atomic insulating state the Wannier Kramers pairs are centered at two non-maximal Wyckoff positions related to each other by the twofold rotation symmetry. All in all, we have thus reached the classification summarized in Table 3.4 of the seven distinct atomic insulating states realizable in the $p2$ wallpaper group with four occupied bands.

When comparing this with the eight allowed configurations for the three $\mathbb{Z}_2$ invariants, one can immediately recognize that an insulating state characterized by the two nested quantization polarization invariants $\nu^{\mathcal{M};0}_{k_2=0} = \nu^{\mathcal{M};1/2}_{k_2=0} = 1$ with $\nu^{\mathcal{M};0}_{k_1=0} = 0$ cannot be represented in terms of symmetric exponentially localized Wannier functions. In fact, such a configuration featuring essential degeneracies at unpinned momenta k_1 both around $\nu = 0$ and $\nu = 1/2$ would necessarily imply the closing of the Wannier gap and hence a non-trivial winding of the Wilson loop. We thus conclude that such an insulator corresponds to a topologically non-trivial phase of the fragile type. Its stability against symmetry-allowed perturbations is rooted in the fact that the possible local annihilation of the degeneracies on the $\nu = 0$ or $\nu = 1/2$ line requires a change of the line invariant $\nu^{\mathcal{M}}_{k_2=0} = \left(\nu^{\mathcal{M};0}_{k_2=0} + \nu^{\mathcal{M};1/2}_{k_2=0}\right) \mod 2$, which is only possible with a bandgap closing-reopening point.

Let us now present a model realization of this novel fragile topological insulating phase. The model is built by stacking two quantum spin-Hall insulators on the honeycomb lattice – the so-called Kane-Mele model [2] – with opposite sign of the spin-dependent next-nearest neighbor hopping parametrizing the spin-orbit coupling strength. It reads:

$$\begin{aligned}\mathcal{H}^{\alpha}_{\mathrm{KM}} = &- t^{\alpha} \sum_{\langle i,j\rangle,\sigma} c^{\alpha\dagger}_{i,\sigma} c^{\alpha}_{j,\sigma} + \epsilon^{\alpha} \sum_{i,\sigma} c^{\alpha\dagger}_{i,\sigma} c^{\alpha}_{j,\sigma} - (-1)^{\alpha}\, i t^{\alpha}_2 \sum_{\langle\langle i,j\rangle\rangle_{\hat{x}},\sigma} \eta_{ij} c^{\alpha\dagger}_{i,\sigma} c^{\alpha}_{j,\sigma} \\ &- i\lambda^{\alpha} \sum_{\langle i,j\rangle,\sigma,\sigma'} c^{\alpha\dagger}_{i,\sigma} \left(\mathbf{d}\times\mathbf{s}\right)^{\sigma\sigma'}_{z} c^{\alpha}_{j,\sigma'},\end{aligned}$$

where $\alpha = 1, 2$ labels the layer degree of freedom, t^{α} denotes the nearest-neighbor hopping amplitude, $\langle i,j\rangle$ the sum over nearest-neighbors, t^{α}_2 the amplitude of intrinsic spin-orbit coupling, $\langle\langle i,j\rangle\rangle_{\hat{x}}$ the sum over next-nearest neighbors *only* in the x-direction, $\eta_{ij} = +1\,(-1)$ for hopping in the clock-

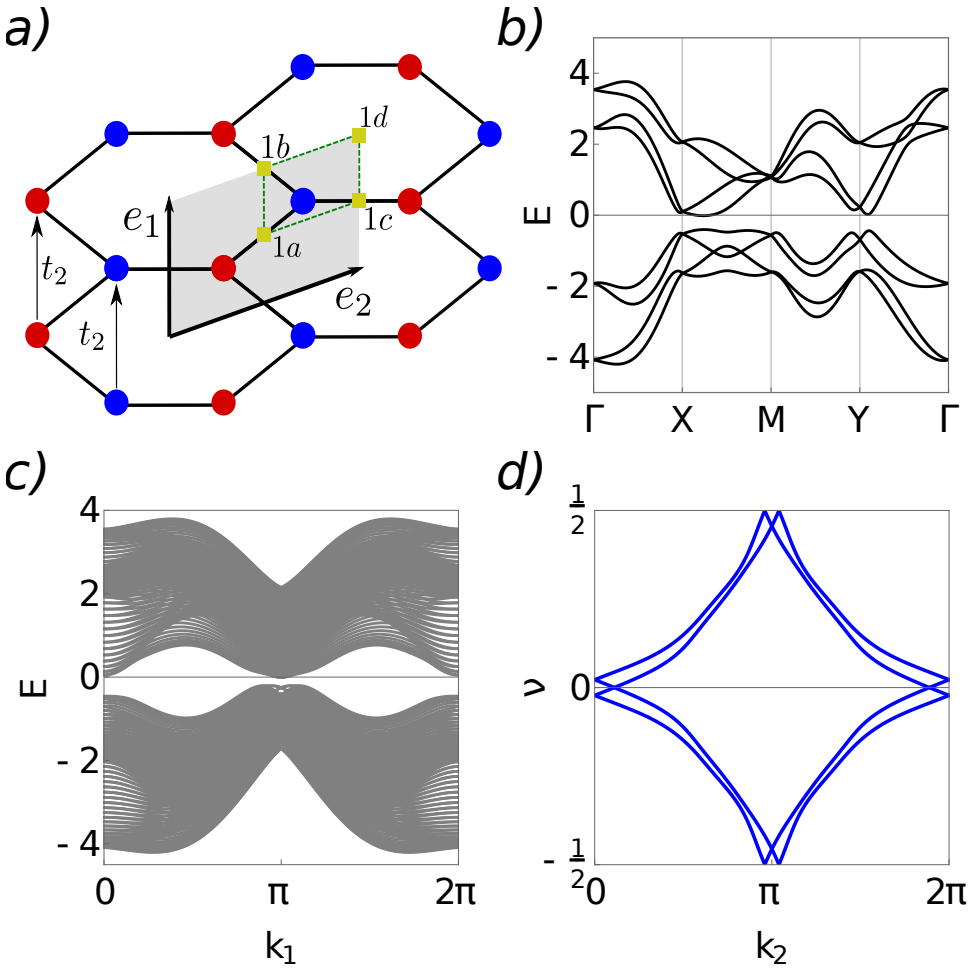

Figure 3.5: (a) Top view of the strained honeycomb bilayer realizing the $N_F = 4$ fragile topological phase. The intralayer spin-dependent hopping amplitude t_2 has been taken only along the zigzag direction to amplify the threefold rotation symmetry breaking. (b) Bulk bands showing a full spectral gap at half-filling. (c) The corresponding spectrum in a ribbon geometry demonstrate the insulating nature of the edges. (d) Wannier bands along the k_2 direction. The Wilson loop in the k_1 direction also show a similar winding. We have chosen the following parameter set: $t^2/t^1 = 1.1$, $t_2^1/t^1 = 1.1$, $t_2^2/t^1 = -0.9$, $\epsilon^1/t^1 = -\epsilon^2/t^1 = 0.1$, $\lambda^1/t^1 = \lambda^2/t^1 = 0.15$, $t_3/t^1 = 0.25$.

wise (counter-clockwise) direction, λ^α the Rashba amplitude, $\mathbf{d}$ the vector between two sites, $\mathbf{s}$ the vector of Pauli matrices and ϵ^α an on-site potential.

We couple the two QSH states with the interlayer coupling term

$$\mathcal{H}_{\text{mix}}(t_3) = -t_3 \left(\sum_{i,\sigma} c^{2\dagger}_{i,\sigma} c^{1}_{i,\sigma} + \sum_{\langle i,j\rangle,\sigma} c^{2\dagger}_{i,\sigma} c^{1}_{j,\sigma} + \sum_{\langle\langle i,j\rangle\rangle_{\hat{y}},\sigma} c^{2\dagger}_{i,\sigma} c^{1}_{j,\sigma} \right),$$

where $\langle\langle i,j\rangle\rangle_{\hat{y}}$ denotes next-nearest neighbor hopping along the $\hat{y}$-direction.

Inversion symmetry is explicitly broken by considering a chemical potential difference between the two layers, *i.e.* $\epsilon^1 \neq \epsilon^2$ while the threefold rotation symmetry breaking due to, *e.g.*, a uniaxial strain [c.f. Fig. 3.5(a)] is incorporated by considering the directional dependence in the hopping amplitudes t_2. The Rashba spin-orbit coupling term also breaks the $\mathcal{M}_z$ symmetry. Being composed of two quantum spin Hall insulators, the FKM invariant of the half-filled model is trivial, and with the explicit interlayer coupling the helical edge states disappear [see Fig. 3.5(b) for the ribbon spectrum]. A direct computation of the Wilson loop spectrum [c.f. Fig. 3.5(d)] shows the non-trivial winding with the line invariants $\nu^{\mathcal{M}}_{k_{1,2}=0} = 0$ that present an obstruction to the Wannier representation of this phase. In Appendix C, we also present a spinful model inspired by the $p_{x,y}$ orbital model presented in Ref. [107] that also realizes the $N_F = 4$ fragile topological phase discussed above.

3.4 More occupied bands

Contrary to the $N_F = 2$ topologically non-trivial phase, which is trivialized only when certain Kramers pairs of bands are added , the $N_F = 4$ topological insulator discussed above is intensively fragile: it is trivialized by the addition of a generic Kramers pair of bands. This assertion can be immediately proved noticing that for a generic $N_F = 6$ insulating state, the $\mathbb{Z}_2 \times \mathbb{Z}_2 \times \mathbb{Z}_2$ classification is saturated by enumerating the phases with symmetric Wannier function. In fact, with three Wannier Kramers pairs in the system, their centers can either lie on three distinct maximal Wyckoff positions, or two Wannier pairs sit at $\mathcal{C}_2$-related non-maximal Wyckoff position with a third pair located at one maximal Wyckoff position. Inspecting the possible features of the Wilson loop spectrum and iterating the arguments presented

Wyckoff positions	$\nu_{k_1=0}^{\mathcal{M}}$	$\nu_{k_2=0}^{\mathcal{M};0}$	$\nu_{k_2=0}^{\mathcal{M};1/2}$
$1a \oplus 1b \oplus 1c$	1	1	0
$1a \oplus 1b \oplus 1d$	1	1	1
$1a \oplus 1c \oplus 1d$	0	0	1
$1b \oplus 1c \oplus 1d$	0	1	1
$1a \oplus \boldsymbol{\nu} \oplus -\boldsymbol{\nu}$	0	0	0
$1b \oplus \boldsymbol{\nu} \oplus -\boldsymbol{\nu}$	0	1	0
$1c \oplus \boldsymbol{\nu} \oplus -\boldsymbol{\nu}$	1	0	0
$1d \oplus \boldsymbol{\nu} \oplus -\boldsymbol{\nu}$	1	0	1

Table 3.5: The $\mathbb{Z}_2 \times \mathbb{Z}_2 \times \mathbb{Z}_2$ classification of atomic insulating states in the $p2$ wallpaper group when three occupied Kramers pairs of bands are occupied, *i.e.* $N_F = 6$, indicating the relation between the Wannier Kramers pairs center of charges and the ("nested") quantized partial polarization topological invariants. This classification is generically valid for an arbitrary number of occupied bands $N_F = 4n + 2$ with the integer $n \geq 1$, which will only include more unpinned pairs of Kramers pairs.

in the former sections we reach the classification summarized in Table 3.5. Note that this classification is generally valid for $N_F = 4n + 2$ and $n \geq 1$. In fact, by adding two Wannier Kramers pairs to a state with $N_F = 6$, we will end up in one of the $N_F = 6$ configurations [c.f. Table 3.5] with the addition of two Wannier Kramers pair centered at unpinned two-fold rotation symmetric momenta, which do not change the $\mathbb{Z}_2$ invariants.

Finally, in Table 3.6 we also provide the classification of atomic insulators with four Wannier Kramers, which is also valid for a generic number of occupied bands $N_F = 4n$ and $n > 1$. Note that the distribution of $\mathbb{Z}_2$ invariants is strictly equivalent to the case of four occupied bands. However, the topological non-trivial fragile phase is substituted by an atomic insulator where the four Wannier Kramers pairs are centered at the four maximal Wyckoff positions. In this configuration, in fact, the Wilson loop spectrum is the superposition of Fig. 3.4(b) and Fig. 3.4(c) which is allowed with a full Wannier gap with a minimum number of eight Wannier bands.

Wyckoff positions	$\nu^{\mathcal{M}}_{k_1=0}$	$\nu^{\mathcal{M};0}_{k_2=0}$	$\nu^{\mathcal{M};1/2}_{k_2=0}$
$1a \oplus 1b \oplus 1c \oplus 1d$	0	1	1
$\boldsymbol{\nu}_1 \oplus -\boldsymbol{\nu}_1 \oplus \boldsymbol{\nu}_2 \oplus -\boldsymbol{\nu}_2$	0	0	0
$1a \oplus 1b \oplus \boldsymbol{\nu} \oplus -\boldsymbol{\nu}$	0	1	0
$1a \oplus 1c \oplus \boldsymbol{\nu} \oplus -\boldsymbol{\nu}$	1	0	0
$1a \oplus 1d \oplus \boldsymbol{\nu} \oplus -\boldsymbol{\nu}$	1	0	1
$1b \oplus 1c \oplus \boldsymbol{\nu} \oplus -\boldsymbol{\nu}$	1	1	0
$1b \oplus 1d \oplus \boldsymbol{\nu} \oplus -\boldsymbol{\nu}$	1	1	1
$1c \oplus 1d \oplus \boldsymbol{\nu} \oplus -\boldsymbol{\nu}$	0	0	1

Table 3.6: The $\mathbb{Z}_2 \times \mathbb{Z}_2 \times \mathbb{Z}_2$ classification of atomic insulating states in the $p2$ wallpaper group when four occupied Kramers pairs of bands are occupied, *i.e.* $N_F = 8$, indicating the relation between the Wannier Kramers pairs center of charges and the ("nested") quantized partial polarization topological invariants. This classification is generically valid for an arbitrary number of occupied bands $N_F = 4n$ with the integer $n > 1$, which will only include more unpinned pairs of Kramers pairs.

3.5 Conclusions

In this paper, we presented a classification of gapped insulating phases that cannot be diagnosed using crystalline symmetry eigenvalues. We have showcased two-dimensional crystals in the wallpaper group $p2$ where all gapped phases have the same physical elementary band representation, but they can be nevertheless classified with three $\mathbb{Z}_2$ topological invariants: the quantized nested partial polarizations – partial Berry phases – along high-symmetry lines in the two-dimensional Brillouin zone of the system.

Using the ensuing $\mathbb{Z}_2 \times \mathbb{Z}_2 \times \mathbb{Z}_2$ classification, we have been able to classify all atomic insulating states and identify non-Wannierazible topological crystalline phases protected by twofold rotation symmetry and time-reversal symmetry. Since the crystal does not possess boundaries that are left invariant under the protecting twofold rotation symmetry, these topological phases do not display gapless anomalous boundary modes although their bulk is topologically non-trivial. Instead, they represent an example of the recently discovered fragile topology, and thus they can be trivialized with the addition of atomic valence bands. In this respect, we wish to emphasize that the fragile topological phase realized with two occupied valence

bands, which is similar in nature to the fragile phases recently discussed in the literature in other wallpaper groups does not necessarily decay into a Wannierazible atomic insulating state when an additional Kramers related pair of bands are introduced. In fact, such band addition might lead to our novel $N_F = 4$ topological crystalline phase whose Wilson loop winding is strictly protected by the quantization of the nested quantized partial Berry phase in the presence of time-reversal and twofold rotation symmetries.

An interesting direction for future research is the extension of the classification presented here to other wallpaper and space groups where the symmetry data of the valence bands could be combined with Berry phase invariants to search for new topological electronic materials. Furthermore, the Berry phase invariants for atomic insulating phases can be also exploited to obtain, using the Wannier centers flow of hybrid Wannier functions [8, 29], topological invariants for higher-order topological insulators with helical hinge modes in non-centrosymmetric crystals.

Appendix A: Nested partial polarization in Wilson loop spectra with $\mathcal{C}_2$ and Θ symmetry

Here we show that the nested partial polarizations are well-defined quantities in gapped Wilson loop spectra, and that they are quantized in the presence of $\mathcal{C}_2$ and Θ symmetry. In addition, we calculate the partial polarizations for various Wilson loop spectra.

Let us start by examining how the symmetries act on the Wilson loop. Consider the Wilson loop operator $\mathcal{W}_{(k_1,2\pi)\leftarrow(k_1,0)}$, $\mathcal{C}_2$ and Θ symmetry then require [7, 101]

$$\mathcal{C}_2\mathcal{W}_{(k_1,2\pi)\leftarrow(k_1,0)}\mathcal{C}_2^\dagger = \mathcal{W}^\dagger_{(-k_1,2\pi)\leftarrow(-k_1,0)},$$
$$\Theta\mathcal{W}_{(k_1,2\pi)\leftarrow(k_1,0)}\Theta^\dagger = \mathcal{W}^\dagger_{(-k_1,2\pi)\leftarrow(-k_1,0)},$$

where the complex conjugate on the right-hand side comes from the fact that both symmetries send $k \to -k$ and hence reverse the contour of the Wilson loop operator. Furthermore, $\mathcal{C}_2$ relates the eigenvalues of the Wilson loop operator

$$\{\nu_i(k_1)\} = \{-\nu_i(-k_1)\},$$

and time-reversal relates

$$\{\nu_i(k_1)\} = \{\nu_i(-k_1)\},$$

where $\{\}$ denotes the set of eigenvalues. Hence $\mathcal{C}_2\Theta$ enforces a chiral symmetry in the Wilson loop spectrum.

Now let us show, following Ref. [7], that a single crossing in the Wilson loop spectrum is locally protected by the combination of $\mathcal{C}_2$ and Θ symmetry. Let us work in a basis where $\mathcal{C}_2\Theta = \mathcal{K}$, where $\mathcal{K}$ indicates complex conjugation. The symmetry restriction on the Wilson loop operator is then

$$\mathcal{K}\mathcal{W}_{(k_1,2\pi)\leftarrow(k_1,0)}\mathcal{K} = \mathcal{W}_{(k_1,2\pi)\leftarrow(k_1,0)},$$

since $\mathcal{C}_2\Theta$ sends $k \to k$. Since the Wilson loop operator in this basis is an $SO(N)$ matrix, we can write it as the exponential of an Hermitian matrix

$\mathcal{H}_{\mathcal{W}}$, which is restricted by $\mathcal{C}_2\Theta$ such that

$$\mathcal{H}_{\mathcal{W}}(k_1) = -\mathcal{H}_{\mathcal{W}}(k_1)^* .$$

Near a two-band crossing, this restriction means that locally $\mathcal{H}_{\mathcal{W}}(k_1) = k_1 \cdot \sigma_y$. A single twofold degeneracy on the $\nu = 0, 1/2$ lines cannot be gapped out without breaking $\mathcal{C}_2\Theta$ symmetry, but only moved on the line. Therefore, as for a Weyl point, the degeneracy can be only removed by pair annihilation.

We now turn to the various possible Wilson loop spectra, and compute their partial polarizations. In Fig. 3.6(a) we have drawn a generic Wilson loop spectrum for one occupied Kramers pair. The corresponding Wannier bands are given by

$$\varphi_k^I = \alpha\psi_k^I + \beta\psi_k^{II},$$
$$\varphi_k^{II} = \gamma\psi_k^I + \delta\psi_k^{II},$$

where ψ_k^I and ψ_k^{II} are the Bloch waves (schematically drawn in Fig. 3.6(b) along the same contour), and the coefficients are given by the eigenvectors of the Wilson loop matrix [see also Sec. IV]. The Wannier bands in Fig. 3.6(a) are thus obtained by a unitary transformation on the occupied eigenstates of the Hamiltonian [Fig. 3.6(b)], and will be linear combinations thereof. These Wannier bands satisfy [see again Fig. 3.6(a)],

$$\varphi_k^I = e^{i\theta(k)}\mathcal{C}_2\varphi_{-k}^I,$$
$$\varphi_k^I = e^{i\phi(k)}\Theta\varphi_{-k}^{II}.$$

The partial polarization is in this case given by the Berry phase of φ_k^I. Since φ_k^I is $\mathcal{C}_2$ symmetric, its Berry phase, and hence the partial polarization is quantized to $0, \pi$.

Now consider two occupied Kramers pairs with two crossings at $\nu = 0$ (Fig. 3.6(c)). The colors indicate the Kramers partners, and the dotted (solid) lines are $\mathcal{C}_2$ partners. To find the partial polarization we split the bands into two time-reversal channels. The only possibility that leaves us with periodic subsets of bands is taking the solid blue and dotted red bands together, and the solid red and dotted blue bands together (shown in Fig. 3.6(c) on the right).

Let us denote the solid blue Wannier band by $a(k)$, and define the red dotted band $b(k)$ by

$$b(k) := \mathcal{C}_2 \theta a(k).$$

Clearly the bands are not periodic, and we have

$$\begin{aligned} a(2\pi) &= b(0), \\ b(2\pi) &= a(0). \end{aligned}$$

We now try to construct a periodic gauge by a basis transformation, under which the partial polarization is invariant. We define

$$\begin{aligned} \tilde{a}(k) &= [a(k) + b(k)]/2, \\ \tilde{b}(k) &= [a(k) - b(k)]/2. \end{aligned}$$

Now

$$\begin{aligned} \tilde{a}(2\pi) &= [a(2\pi) + b(2\pi)]/2 \\ &= [b(0) + a(0)]/2 = \tilde{a}(0), \end{aligned}$$

hence $\tilde{a}(k)$ is periodic, however

$$\begin{aligned} \tilde{b}(2\pi) &= [a(2\pi) - b(2\pi)]/2 \\ &= [b(0) - a(0)]/2 = -\tilde{b}(0), \end{aligned}$$

is anti-periodic. Multiplying by a phase and defining

$$\tilde{\tilde{b}}(k) = e^{ik/2}\tilde{b}(k),$$

remedies this situation. Under $\mathcal{C}_2\Theta$ we now have

$$\begin{aligned} \mathcal{C}_2\Theta\, \tilde{a}(k) &= \tilde{a}(k), \\ \mathcal{C}_2\Theta\, \tilde{\tilde{b}}(k) &= e^{-ik/2}\tilde{b}(k) \\ &= e^{-ik}\tilde{\tilde{b}}(k). \end{aligned}$$

Using this, we can calculate the Berry phase of the two bands separately,

$$\begin{aligned}\gamma_a &= \int dk\, \tilde{a}\,(k)^\dagger\, i\partial_k \tilde{a}\,(k) \\ &= \int dk\, \tilde{a}\,(k)^\dagger\, (\mathcal{C}_2\theta)^\dagger\, (\mathcal{C}_2\theta)\, i\partial_k \tilde{a}\,(k) \\ &= -\int dk\, \tilde{a}\,(k)^\dagger\, i\partial_k \tilde{a}\,(k) = -\gamma_a\end{aligned}$$

and

$$\begin{aligned}\gamma_b &= \int dk\, \tilde{\tilde{b}}\,(k)^\dagger\, i\partial_k \tilde{\tilde{b}}\,(k) \\ &= \int dk\, \tilde{\tilde{b}}\,(k)^\dagger\, (\mathcal{C}_2\theta)^\dagger\, (\mathcal{C}_2\theta)\, i\partial_k \tilde{\tilde{b}}\,(k) \\ &= -\int dk\, \tilde{\tilde{b}}\,(k)^\dagger\, e^{ik} i\partial_k e^{-ik} \tilde{\tilde{b}}\,(k) \\ &= -\gamma_b - \int dk\, \partial_k k = -\gamma_b - 2\pi,\end{aligned}$$

from which we see $\gamma_a = 0$ and $\gamma_b = \pi$, and thus we find that the partial polarization is π. In particular, this shows that the nested polarization around $\nu = 0, 1/2$ will be π when there are an odd number of crossings in half the Brillouin zone on this line.

Let us finally consider two occupied Kramers' pairs with a disconnected Wilson loop spectrum (see Fig. 3.6(d)-(e)). To calculate the partial polarization of these bands, let us first consider the red Kramers pair in isolation. To calculate the partial polarization we need to again calculate the Berry phase of the red dotted band. This band does not posses $\mathcal{C}_2$ symmetry and hence its Berry phase will not be quantized. In order to calculate the partial polarization of the blue bands, we calculate the Berry phase of the blue dotted band. However, since the blue dotted and the red dotted bands are related by $\mathcal{C}_2$ symmetry, we find for their Berry phases

$$\gamma^I_{\text{Red}} = -\gamma^I_{\text{Blue}},$$

and hence the partial polarization, which is the sum of the two, is zero.

To calculate *nested* partial polarizations, we need to select symmetric

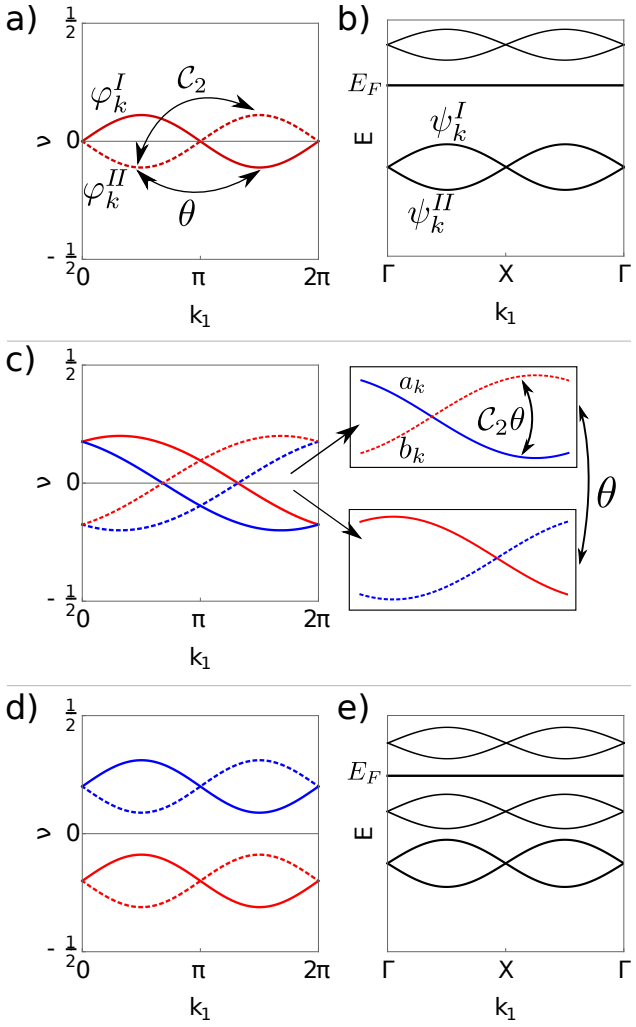

Figure 3.6: (a) Schematic drawing of a generic Wilson loop spectrum with one occupied Kramers pair. The two Wannier bands φ_k^I and φ_k^{II} are related to each other by time-reversal symmetry, and are themselves $\mathcal{C}_2$ symmetric. (b) Generic band structure corresponding to (a), the Wannier states are obtained by linear combinations of the eigenstates of the Hamiltonian ψ_k^I,ψ_k^{II}. (c) Wilson loop spectrum for two occupied Kramers pairs with two crossings at $\nu = 0$. The colors denote the two different Kramers pairs, and the $\mathcal{C}_2$ partners have a solid (dotted) line. The two time-reversal channels are depicted on the right, which are by themselves $\mathcal{C}_2\Theta$ symmetric. (d) Disconnected Wilson loop of two occupied Kramers pairs, again color denotes Krames pairs, dotted (solid) the $\mathcal{C}_2$ partners. (e) Corresponding band structure with two occupied Kramers pairs.

regions centered around $\nu = 0$ and $\nu = 1/2$. Since there are two gaps in the spectrum, we have two choices. We can either include the pair of Kramers pairs, or exclude them from either region. However, we have just seen that the partial polarization of this set of bands is zero, and hence either choice will yield the same result. Indeed for any N_F, the only choice in selecting a subset of bands centered around $\nu = 0, 1/2$, is including or excluding pairs of disconnected bands such as in Fig. 3.6(e), making the nested partial polarizations well-defined quantities.

Gapped Wilson loop spectra for arbitrary N_F will consist of linear combinations of the three cases presented here, and since the partial polarization is an additive quantity, we know how to calculate it for arbitrary N_F.

Let us finally show that the nested partial polarization of Wannier band cannot change by a gap closing in the Wilson loop spectrum away from $\nu = 0, 1/2$ in the presence of $\mathcal{C}_2$ and Θ symmetry. We consider the situation in Fig. 3.7(a), where we want to show that by a gap closing as shown in Fig. 3.7(b), the nested partial polarization of the blue pair of bands cannot change. We parametrize this gap closing by some parameter λ, where for $\lambda = 0$ the Wilson loop spectrum is gapless and looks like Fig. 3.7(b).

The nested partial polarization is equal to the Berry phase of the blue dotted band, which we will call $a_{k,\lambda}$. To see how the Berry phase of this band changes due to a gap closing, we consider the $\lambda - k_1$ plane. The change in Berry phase is then given by the sum of the Berry phases around the gap closing points which we will call γ_1 and γ_2, the contours of which are drawn in Fig. 3.7(c).

In a $\mathcal{C}_2$ symmetric system we have, up to a total derivative,

$$\mathcal{A}_\lambda(k, \lambda) \equiv \langle a_{k,\lambda}| \, i\partial_\lambda \, |a_{k,\lambda}\rangle = \mathcal{A}_\lambda(-k, \lambda),$$

since $\mathcal{C}_2$ does not act on λ, and

$$\mathcal{A}_k(k, \lambda) \equiv \langle a_{k,\lambda}| \, i\partial_k \, |a_{k,\lambda}\rangle = -\mathcal{A}_\lambda(-k, \lambda),$$

again up to a total derivative. Now the segments of the contour at constant k (dotted lines in Fig. 3.7(c)) cancel each other because

$$\mathcal{A}_\lambda(k, \lambda)\, d\lambda = -\mathcal{A}_\lambda(-k, \lambda)\, d\lambda,$$

since $d\lambda$ is oriented differently for the two segments. The contours at con-

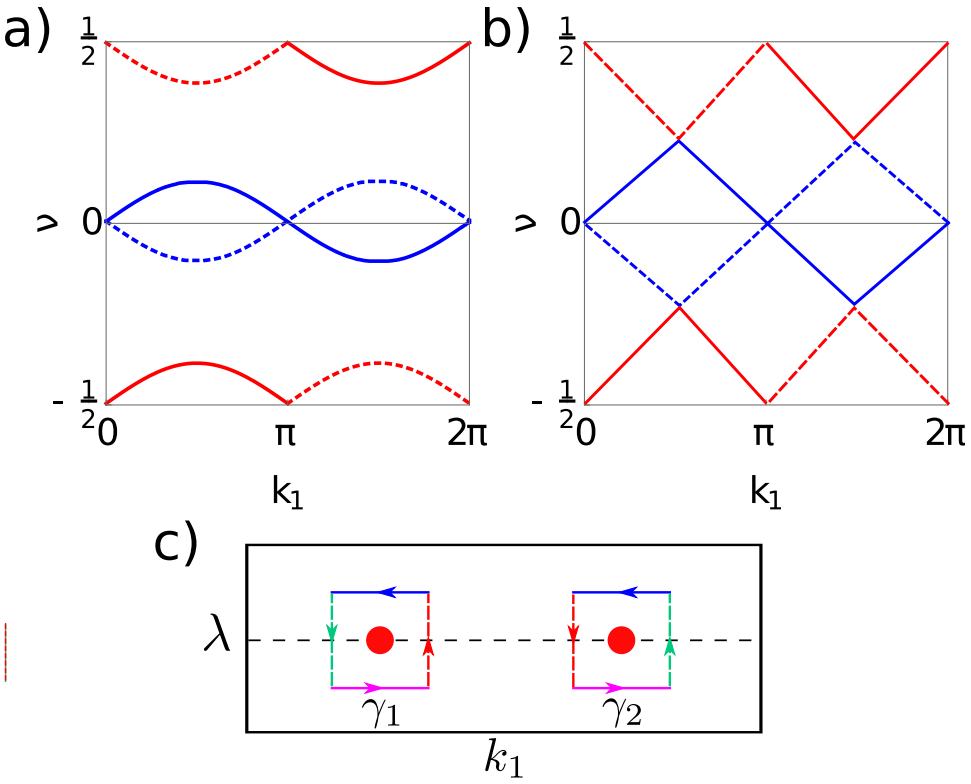

Figure 3.7: (a) Schematic Wilson loop spectrum for two occupied Kramers pairs, (b) which might undergo a gap closing and reopening. (c) Contours in parameter space used to calculate the change in Berry phase.

stant λ give us

$$\mathcal{A}_k\left(k,\lambda\right)dk = -\mathcal{A}_k\left(-k,\lambda\right)dk.$$

Hence we find

$$\gamma_1 = -\gamma_2 + 2\pi n,$$

where $n \in \mathbb{Z}$, and hence the change in Berry phase for $a_{k,\lambda}$ is a multiple of 2π, leaving the nested partial polarization unchanged.

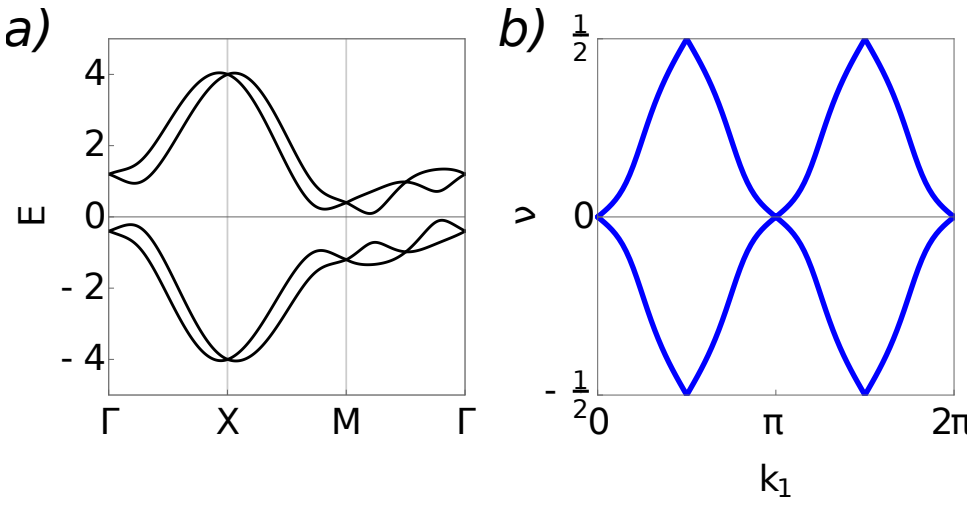

Figure 3.8: Bulk bands (a) and Wilson loop spectrum (b) for the $\mathcal{C}_4$ symmetric fragile topological insulator. Plots are for $\epsilon_1/t = 0.1$,$\epsilon_2/t = -0.3$, $t_2/t = 0.8$, $\lambda/t = 0.4$.

Appendix B: Topological insulator model of the fragile type with $N_F = 2$

In addition to the model presented in the main text, a topological phase of the fragile type with $N_F = 2$ can also be obtained in a fourfold rotation symmetric system by considering the following $\mathcal{C}_4$ symmetric $\mathcal{C} = +2$ Chern insulator,

$$\begin{aligned}\mathcal{H} = &-\epsilon_1\big[\cos(k_x)+\cos(k_y)\big](\tau_0+\tau_z)-\epsilon_2\big[\cos(k_x)+\cos(k_y)\big](\tau_0-\tau_z)\\ &-2t\big[\cos(k_x)-\cos(k_y)\big]\tau_x-t_2\big[\sin(k_x)\sin(k_y)\big]\tau_x,\end{aligned}$$

where $\epsilon_1, \epsilon_2, t, t_2$ are hopping amplitudes. We then again add a time-reversal copy and couple them by

$$\mathcal{H}_{\text{mix}} = -\lambda\left[\sin(k_x)\,\tau_0 s_y + \sin(k_y)\,\tau_0 s_x\right].$$

The bulk bands and Wilson loop spectrum are plotted in Fig. 3.8. The

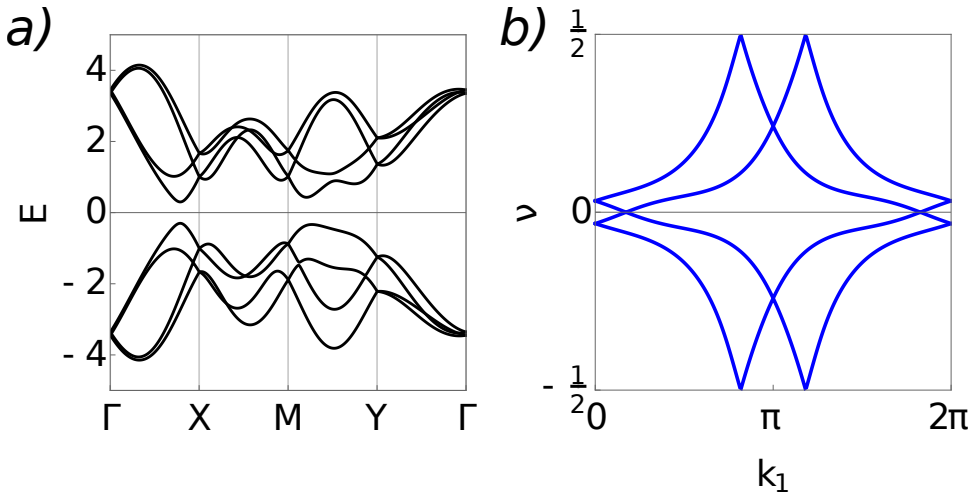

Figure 3.9: Bulk band spectrum (a) and Wilson loop spectrum (b) of the Hamiltonian $\mathcal{H}_{p_x p_y}$ for $\epsilon = 0.5$, $t_\pi/t_\sigma = 1.5$, $t_2/t_\sigma = 3.75$, $\lambda/t_\sigma = 1.2$

$\mathcal{C}_4$ operator is represented by $\mathcal{C}_4 = \tau_z \otimes e^{is_z/4}$, and time-reversal by $\Theta = U\mathcal{K}$ with $U = I_2 \otimes is_y$ and $\mathcal{K}$ is complex conjugation. The symmetry eigenvalues of the occupied bands at Γ are $\{e^{i\pi/4}, e^{-i\pi/4}\}$, and at the M point $\{-e^{-i\pi/4}, -e^{i\pi/4}\}$, which are compatible with a Wannier function centered at the maximal $\mathcal{C}_4$ symmetric position $1b = \{1/2, 1/2\}$.

Appendix C: Fragile topological insulator with two occupied Kramers pairs of bands

As mentioned in the main text, a different way to construct a model exhibiting the $N_F = 4$ fragile topological phase is by considering a model of $p_{x,y}$ orbitals on a honeycomb lattice introduced in Ref. [107],

$$\mathcal{H}_{p_x p_y}(k) = \begin{pmatrix} 0 & h_k \\ h_k^\dagger & 0 \end{pmatrix} + H_k^1,$$

with

$$h_k = \frac{1}{2}\left(1+\alpha\, e^{-ik_2}+e^{-ik_1}\right)(t_\sigma+t_\pi)+\frac{\sqrt{3}}{4}\left(-1+e^{-ik_1}\right)(t_\sigma-t_\pi)\,\sigma_x - \frac{1}{2}\left(-\frac{1}{2}+\alpha\, e^{-ik_2}-\frac{1}{2}e^{-ik_1}\right)(t_\sigma-t_\pi)\,\sigma_z,$$

and

$$H_k^1 = -\frac{t_2}{4}\left\{\sin\left[i\left(k_2-k_1\right)\right]+\sin\left[ik_1\right]-\rho\,\sin\left[ik_2\right]\right\}\tau_z\otimes\sigma_y,$$

where t_σ and t_π are the hopping amplitudes for the σ and π pairing, t_2 is the amplitude of next-nearest-neighbor hopping and σ_i and τ_i are Pauli matrices that act in orbital and sublattice space respectively. α and ρ are two parameters we have introduced to break the $\mathcal{C}_3$ symmetry. For $\alpha=\rho=1$, the $\mathcal{C}_3$, symmetry is preserved and our Hamiltonian is equivalent to the one in Ref. [107].

We now take two copies of two copies of $\mathcal{H}_{p_xp_y}(k)$, where one copy has spin pointing in the positive x-direction, and the other spin pointing in the negative x-direction. In addition, we shift the momentum along the x-direction of the copies in opposite direction:

$$\begin{aligned}\mathcal{H} =& \mathcal{H}_{p_xp_y}\left(k-\hat{x}\epsilon\right)|{\leftarrow}\rangle\langle{\leftarrow}| + \mathcal{H}_{p_xp_y}\left(-k+\hat{x}\;\epsilon\right)^*|{\rightarrow}\rangle\langle{\rightarrow}| \\ &+ \mathcal{H}_{\text{mix}}|{\rightarrow}\rangle\langle{\leftarrow}|,\end{aligned} \tag{3.3}$$

where the spins are mixed by

$$\mathcal{H}_{\text{mix}} = -i\lambda\sin\left(k_x\right)\tau_0\otimes\sigma_0.$$

This Hamiltonian has $\mathcal{C}_2$ and Θ symmetry, where $\mathcal{C}_2 = -\tau_0\sigma_x e^{is_x\pi/2}$, and $\Theta = U\mathcal{K}$ with $U=-i\tau_0\sigma_0 s_y$ and $\mathcal{K}$ complex conjugation, and τ_i, σ_i, s_i Pauli matrices acting in orbital-space, sublattice-space and spin-space respectively. Fig. 3.9 shows the bulk band spectrum and the Wilson loop spectrum.

4 The hybrid-order topology of weak topological insulators

The essence of a free-fermion topological insulator is that it cannot be adiabatically deformed to a trivial atomic insulator, whose nature can be understood considering electrons as localized point particles. Put differently, topological insulators do not admit a representation in terms of exponentially localized Wannier functions (WFs). This obstruction to Wannier representability is, in turn, reflected in the presence of anomalous gapless boundary modes. Examples include the chiral (helical) edge modes in quantum (spin) Hall insulators [1–3, 47, 50, 100], as well as the surface Dirac cones of three-dimensional topological insulators (TI) [41]. In crystalline systems with an additional set of spatial symmetries, additional topological phases can arise [13]. These topological crystalline insulators (TCI) cannot be represented in terms of WFs respecting the spatial symmetries of the system, and feature, by the bulk-boundary correspondence, anomalous surface states violating a stronger version of the fermion doubling theorem [16] on surfaces that are left invariant under the protecting symmetry. Mirror Chern insulators [14, 74], for instance, are characterized by the presence of gapless surface Dirac cones pinned to mirror planes. Similarly, higher-order topological insulators (HOTI) [8, 9, 17, 19] feature anomalous gapless one-dimensional modes at the hinges connecting two surfaces related by the protecting crystalline symmetry [81].

The topologies related to the internal and spatial symmetries do not necessarily exclude each other and can also coexist. This occurs, for instance in different "dual" topological materials [111–114], which have the topological structure of both a weak TI and a mirror Chern insulator. Likewise, it has been recently proposed that certain topological superconductors can concomitantly feature both surface cones and Majorana hinge modes [115–117]. In all these systems, the topological crystalline structure can be diagnosed using the spatial symmetry content of the electronic bands [5, 10, 25, 97, 107] while the topology due to the internal symmetry is uniquely determined

by the "tenfold-way" invariants [70, 72, 84]. There exist, however, certain topological crystalline phases that are neither characterizable by symmetry indicators, nor by the tenfold way [118]. In two-dimensional systems these phases have recently started to be classified [119].

The question that immediately arises is whether crystalline topologies without symmetry indicators can be embedded in a topological non-trivial insulating phase protected by an internal symmetry. In this work, we provide an affirmative answer by showing that two-dimensional topological insulators in the wallpaper group $p2$ – where time-reversal symmetry (TRS) guarantees the complete absence of symmetry indicators – can be characterized by a set of three crystalline topological $\mathbb{Z}_2$ indices. They correspond to two quantized partial Berry phases [98, 99] and one additional novel topological index that cannot be diagnosed even from the Wilson loop. We subsequently use this new invariant to show that weak TIs possessing a twofold rotation symmetry around the $[\nu_1, \nu_2, \nu_3]$ direction, $\nu_{1,2,3}$ indicating the so-called weak topological indices [120], can be in a non-trivial topological crystalline phase. It is characterized by the presence of anomalous *unpinned* Dirac cones at the surfaces whose Miller indices (modulo 2) are identical to the weak topological indices, *i.e.* the so-called "dark" surfaces of weak TIs where surface Dirac cones protected by TRS are absent. This topological crystalline phase corresponds to a form of hybrid-order topology since the system can be switched to a HOTI with helical hinge modes using translational symmetry breaking perturbations.

4.1 Crystalline topological invariants in quantum spin-Hall insulators

We start out by developing a scheme that is able to capture the full crystalline topology of quantum spin-Hall insulators (QSHI) in systems with a two-fold rotation symmetry $\mathcal{C}_2$. To do so, we first recall that for atomic insulating phases, the crystalline topology is fully determined by the gauge-invariant charge centers [16, 29, 119] of time-reversal symmetric Wannier functions that respect the symmetries of the crystal. The construction of such symmetric Kramers pairs of Wannier functions requires the construction of two time-reversed channels [100] of Bloch waves $\left|\Psi_n^{I,II}(q)\right\rangle$ that are separately $\mathcal{C}_2$ symmetric, where n is a band index running from one to $N_F/2$ and

N_F the total number of occupied bands. The Bloch waves $\left|\Psi_n^{I,II}(q)\right\rangle$ need not be individual eigenstates of the Hamiltonian, but are still basis states spanning the eigenspace corresponding to the N_F occupied bands. Importantly, the construction of symmetric Wannier functions requires a smooth, periodic, and symmetric gauge for the $\left|\Psi_n^{I,II}(q)\right\rangle$ Bloch waves. Since we want to study crystalline topology in non Wannier representable QSHI, we relax these constraints on the gauge by demanding its smoothness, periodicity and symmetry modulo a $\mathcal{U}(N_F/2)\otimes\mathcal{U}(N_F/2)$ gauge degree of freedom, with these two residual gauges acting in the two time-reversed and $\mathcal{C}_2$ symmetric channels. In other words, we require a smooth, periodic and symmetric set of projectors $\rho^{I(II)}(q) = \sum_n \left|\Psi_n^{I(II)}(q)\right\rangle \left\langle\Psi_n^{I(II)}(q)\right|$. In Appendix A, we show how to construct such a gauge assuming for simplicity there are no degeneracies in the band structure other than those required by time-reversal. Since within each sector we have not demanded a continuous gauge, it follows that the channels described by the Bloch waves $\left|\Psi_n^{I,II}(q)\right\rangle$ can be characterized by non-vanishing but opposite Chern numbers $C^{I,II}$. Furthermore, the twofold rotation symmetry endows the two channels with $\mathbb{Z}$ indices that correspond to the multiplicities of the rotation eigenvalues $m^I_{\pm i} \equiv m^{II}_{\mp i}$ at the high-symmetry points in the Brillouin zone (BZ), *i.e.* $m = \Gamma, X, Y, M$ [see Fig. 4.1(a)].

We will now show that these integer crystalline indices and the Chern numbers of the channels can be used to construct four $\mathbb{Z}_2$ invariants that fully characterize the topology of $\mathcal{C}_2$ and time-reversal symmetric insulators in two dimensions. Two $\mathbb{Z}_2$ invariants can be immediately identified in the quantized partial polarizations [98] on the $\mathcal{C}_2$ symmetric lines of the BZ $k_{1,2} \equiv 0$. They correspond to the centers of charge of one-dimensional hybrid Wannier functions and are diagnosed [119] by the Wilson loop spectra $\nu(k_{1,2})$ [see Fig. 4.1(b)]. These quantized partial polarizations can be expressed in terms of the crystalline indices $m^I_{\pm i}$ as $\gamma^I_{1(2)} \equiv \left[\Gamma^I_i + X^I_i(Y^I_i)\right] \mod 2$ (see Appendix B). The third $\mathbb{Z}_2$ invariant corresponds to the Fu-Kane-Mele invariant that characterizes QSHI and can be expressed (see Appendix B) in terms of the crystalline indices as $\nu_{\mathrm{FKM}} = \left(\Gamma^I_i + X^I_i + M^I_i + Y^I_i\right) \mod 2$. To define a fourth $\mathbb{Z}_2$ invariant, notice that the additional combination of eigenvalues $\nu^I_{1d} = \left(\Gamma^I_{-i} - X^I_{-i} - Y^I_{-i} + M^I_{-i}\right)/2 \mod 2$ is linearly independent from the previously defined $\mathbb{Z}_2$ indices. For an atomic insulating

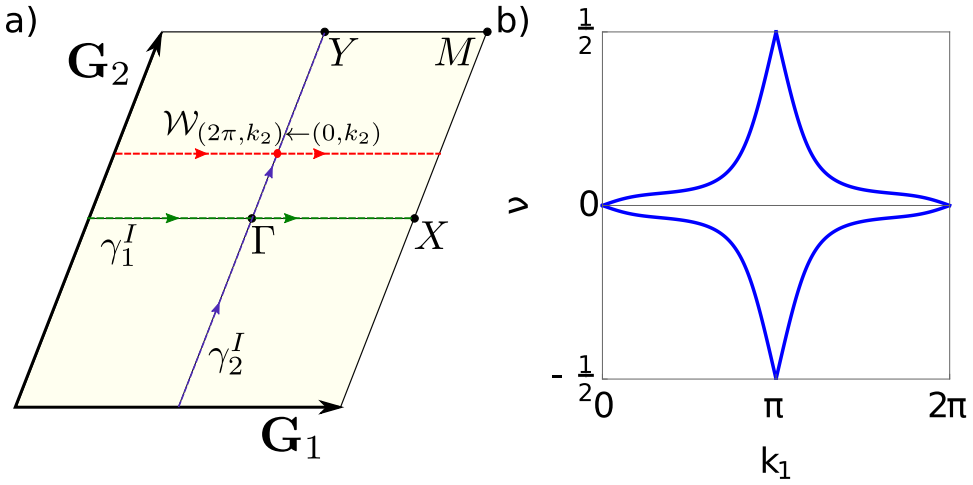

Figure 4.1: (a) Schematic drawing of the Brillouin zone of $\mathcal{C}_2$ symmetric crystal, spanned by reciprocal lattice vectors $\mathbf{G}_1$ and $\mathbf{G}_2$. The partial polarizations are calculated along the green and blue line, and a typical Wilson loop contour is shown in red. (b) Wilson loop spectrum of a QSHI. The winding reflects the topological non-trivial nature of the insulating phase. The quantized value of the Wilson loop for $k_1 = 0$ corresponds to the quantized partial polarizations γ_2^I.

phase, ν_{1d}^I corresponds to the parity of the time-reversed pairs of symmetric Wannier functions centered at the corner of the unit cell with coordinates $1d = \{1/2, 1/2\}$. The fact that in a QSHI the two time-reversed channels I, II are characterized by an odd Chern number immediately yields a semi-integer value $\nu_{1d}^I = \pm 1/2$. However, and this is key, we can still define a $\mathbb{Z}_2$ number reading

$$\gamma_3^I = \frac{1}{2}\left[C^I + \left(\Gamma_{-i}^I - X_{-i}^I - Y_{-i}^I + M_{-i}^I\right)\right] \mod 2.$$

Being independent of the partial polarizations, this new integer cannot be diagnosed by the Wilson loop spectrum but still represents a well-defined and gauge-invariant crystalline topological number. In fact, γ_3^I is manifestly gauge-invariant under intrachannel $\mathcal{U}(N_F/2)$ transformations since it is made out of a Chern number and the twofold rotation symmetry eigenvalues. Furthermore, γ_3^I is also invariant under interchannel gauge transformations, which correspond to the swapping of the channels ($I \leftrightarrow II$) for isolated pairs of bands. These transformations concomitantly change the sign of the Chern numbers of the channels and the multiplicities of the $\mathcal{C}_2$ symmetry eigenvalues, and therefore do not change γ_3^I. We have thus identified three gauge-invariant $\mathbb{Z}_2$ crystalline topological indices, which together with the Fu-Kane-Mele invariant yield a $\mathbb{Z}_2^4$ classification in agreement with a recent K theory study [121].

We finally emphasize that the gauge-invariant γ_3^I is different in nature from the "spin Chern numbers" existing in systems with a mirror symmetry $\mathcal{M}_z$. In this situation, the two time-reversed and $\mathcal{C}_2$ symmetric channels I, II can be taken to be the spin eigenstates $|\uparrow\rangle, |\downarrow\rangle$, such that $C^I \equiv C^\uparrow$. However, this does not determine the value of γ_3^I, as the spin Chern number does not determine ν_{1d}^I. Thus one can find both $\gamma_3^I = 0, 1$ for the same spin Chern number.

4.2 Hybrid-order weak TIs

Next, we exploit the existence of the novel crystalline topology of γ_3^I in three-dimensional bulk crystals with a $\mathcal{C}_{2z}$ rotational symmetry. To do so, let us consider the three-dimensional Brillouin zone of our time-reversal invariant system as a collection of two-dimensional momentum cuts parametrized by

the momentum k_z parallel to the twofold rotation axis. At the time-reversal invariant two-dimensional planes $k_z = 0, \pi$ we consider the system to be a topological non-trivial QSHI. As a result, the bulk three-dimensional crystal will be a three-dimensional topological insulator of the weak class. In principle, we could choose the two $\mathbb{Z}_2$ topological crystalline indices corresponding to the quantized partial polarization of the $k_z = 0, \pi$ QSHI to be different. This, however, would imply that in the triad of "weak" topological invariants [120] (ν_1, ν_2, ν_3), ν_1 and/or ν_2 are different from zero. Hence, the three-dimensional system would feature an even number of surface Dirac cones protected by time-reversal at the (001) and $(00\bar{1})$ surfaces that are left invariant under the $\mathcal{C}_{2z}$ rotation symmetry. As a result, any physical consequence of the crystalline topology cannot manifest itself: it would be completely obscured by the internal, time-reversal, symmetry topology.

However, we can choose the two $\mathbb{Z}_2$ topological crystalline invariants at the time-reversal invariant planes to be equal, thus constraining the weak invariants to be $(0, 0, 1)$. The time-reversal symmetric topology now guarantees the existence of an even number of massless Dirac cones appearing at time-reversal invariant (100) and (010) surface momenta [c.f. Fig. 4.2], while the $\mathcal{C}_{2z}$ invariant (001) surfaces are completely gapped. A non-trivial crystalline topology, which can thus only arise from a difference in γ_3^I at the $k_z = 0, \pi$ planes, will then be in full force and lead to the appearance of a single pair of surface Dirac cones [c.f. Fig. 4.2] at unpinned surface momenta related by the twofold rotation symmetry. This pair of surface Dirac cones realizes a rotational anomaly violating the fermion multiplication theorem of Ref. [16] and can be only removed by breaking the protecting $\mathcal{C}_{2z}$ and/or Θ symmetry [c.f. Fig. 4.2]. We point out that the existence of this rotation anomaly cannot be diagnosed by considering the flow of gauge-invariant Wannier centers between the $k_z = 0, \pi$ planes as in Ref. [16]. This is because at $k_z = 0, \pi$ our system is a topological insulator, and therefore cannot be represented in terms of localized Wannier functions. The appearance of the unpinned Dirac surface cones is instead detected by considering the k_z-directed Wilson loop [see Appendix D] in agreement with Ref. [122], although the stability of the surface Dirac cones cannot be inferred from the Wilson loop that consequently cannot be used to derive a "topological index". We dub this new three-dimensional insulating phase a hybrid-order weak topological insulator: it is by itself a first-order topological insulator in $d = 3$ dimensions with $d-1$ gapless boundary modes, but it can be switched

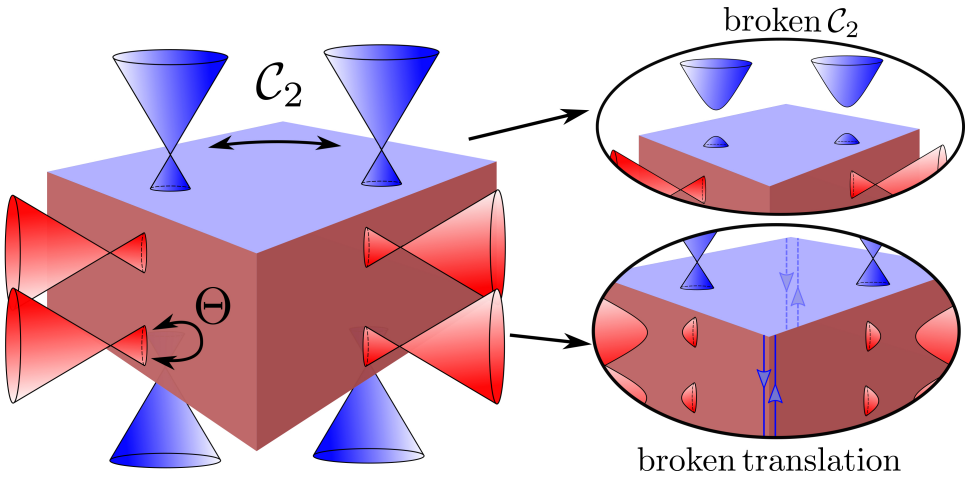

Figure 4.2: Schematic of a hybrid-order weak topological insulator. At the top and bottom surfaces left invariant under the protecting $\mathcal{C}_{2z}$ symmetry a single pair of surface Dirac cones exist. On the side surfaces an even number of Dirac cones pinned to time-reversal invariant surface momenta are mandated by the weak topological invariants. When breaking $\mathcal{C}_2$ symmetry, the topological crystalline surface Dirac cones at the top and bottom surfaces can be gapped out leaving these surfaces completely dark. By breaking the translational symmetry, *i.e.* doubling the unit cell, the time-reversal symmetry protected Dirac cones gap out, and the topological crystalline Dirac cones are then connected by helical hinge states.

using unit cell doublings in the $\hat{z}$-direction, and thus without breaking any protecting symmetry, to a second-order topological crystalline insulator with anomalous gapless hinge modes [c.f. Fig. 4.2] and $\mathcal{C}_2$ rotation anomaly [16], and reminiscent of the surface cones one predicted to appear in $\alpha-Bi_4Br_4$ and a family of Zintl compounds [123, 124].

4.3 Stacked Kane-Mele model

Having established the existence of the hybrid-order weak topological insulator, we now present an explicit model based on stacked Kane-Mele systems realizing this phase. Let us consider a tight-binding model for spin-1/2 electrons on AA stacked honeycomb lattices. In momentum space the Bloch Hamiltonian can be written as:

$$\begin{aligned}\mathcal{H}(\mathbf{k}) = d_1(\mathbf{k})\tau_x \otimes s_0 + d_2(\mathbf{k})\tau_y \otimes s_0 + d_5(\mathbf{k})\tau_z \otimes s_z \\ + d_4(\mathbf{k})\tau_z \otimes s_y,\end{aligned} \tag{4.1}$$

where the τ_i's and s_i's are the Pauli matrices acting in sublattice and spin space respectively. The first two terms in the Hamiltonian above correspond to intralayer spin-independent nearest-neighbor hopping processes, and the corresponding coefficients are $d_1(\mathbf{k}) = -t\left[1 + \cos x_1 + \cos x_2\right]$ and $d_2(\mathbf{k}) = -t\left[\sin x_1 + \sin x_2\right]$. Here we have introduced the hopping amplitude t while $x_{1,2} = \mathbf{k} \cdot \mathbf{a}_{1,2}$, $\mathbf{a}_{1,2}$ being the Bravais lattice vectors. The third term in the Hamiltonian Eq. 4.1 corresponds to spin-orbit interaction which involves intralayer spin-dependent second-neighbor hopping. We take the corresponding coefficient $d_5(\mathbf{k}) = 2t_2 \sin(x_1)$, with t_2 the hopping strength, thus explicitly breaking the threefold rotation symmetry. Finally, the last term in the Hamiltonian involves interlayer spin-dependent hopping amplitudes and the corresponding coefficient reads $d_4(\mathbf{k}) = -2t_3 \sin(k_z)$. We introduce this term to explicitly break the effective "in-plane" time-reversal symmetry [125] to allow for the possibility of a change of (crystalline) topology in the two time-reversal symmetric planes $k_z = 0, \pi$. Since the Hamiltonian Eq. 4.1 preserves bulk inversion symmetry, we can immediately obtain the strong and weak topological indices and thus obtain $(\nu_0; \nu_1, \nu_2, \nu_3) = (0; 0, 0, 1)$. In this form, however, Eq. 4.1 does not model a hybrid-order weak topological insulator: it can be adiabatically connected to a stack of uncoupled QSHI

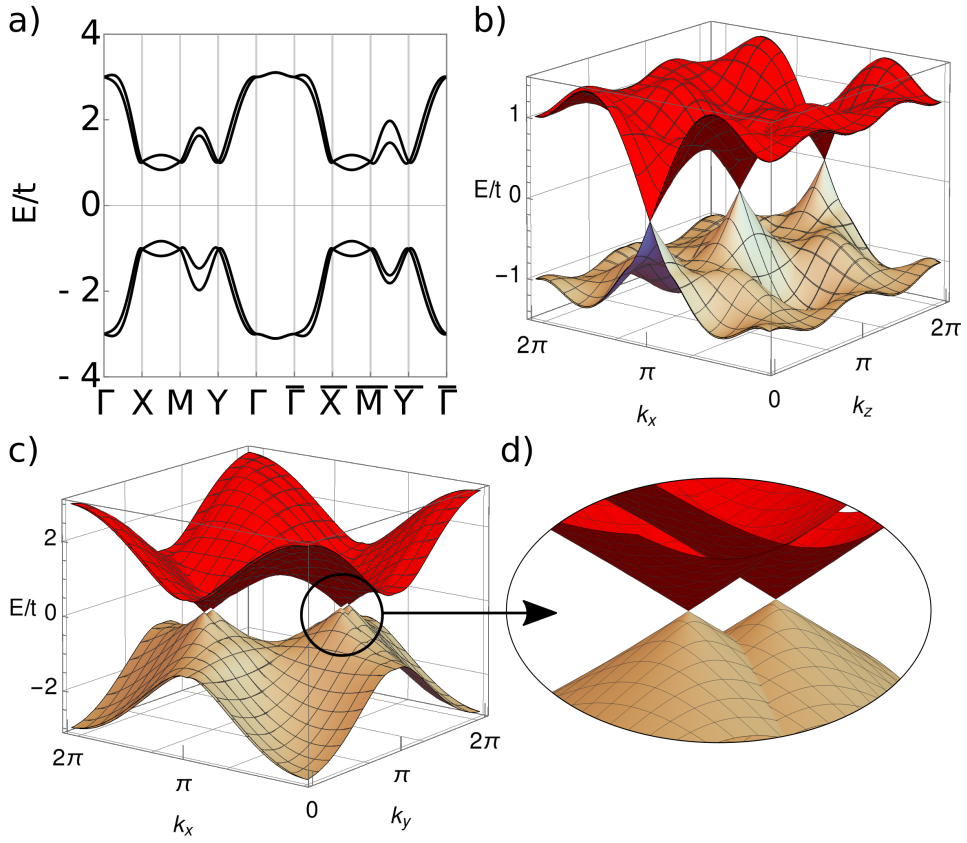

Figure 4.3: (a) Bulk bandstructure of the stacked Kane-Mele model Eq. 4.1 by further accounting for a Rashba spin-orbit coupling term of strength $\lambda/t = 0.1$. The strength of the modified intralayer spin-orbit coupling term has been fixed to $t_2/t = 0.7$, whereas the interlayer spin-orbit coupling strength has been fixed to $t_3/t = 0.4$. (b) Energy spectrum in a slab geometry with open boundary conditions along the $\hat{y}$ direction. The (010) and $(0\bar{1}0)$ surfaces exhibit an even number of Dirac cones pinned at time-reversal invariant surface momenta as required by the weak topological invariants. (c) Surface energy spectrum along the stacking $\hat{z}$ direction. There are two pairs of surface Dirac cones localized at the (001) and the $(00\bar{1})$ surface. The Dirac points are found at unpinned surface momenta related by the $\mathcal{C}_2$ symmetry. The zoom-in (d) shows that the Dirac cones at opposite surface are located at different momenta due to the lack of inversion symmetry. All energies have been measured in unit of the hopping strength t.

and consequently its (001) surface does not feature gapless modes. To endow the system with a non-trivial crystalline topology we instead modify the intralayer spin-orbit coupling as $d_5(\mathbf{k}) \to \cos(k_z) d_5(\mathbf{k})$. This modification keeps the strong and weak topological indices intact but changes the crystalline topology of the system. Note that also the inversion eigenvalues remain unchanged, thus implying that the hybrid-order phase cannot be diagnosed by inversion symmetry indicators.

To show this, we have computed the bulk bandstructure [see Fig. 4.3(a)] and the surface energy spectra [see Fig. 4.3(b),(c),(d)] of this modified model by further accounting for an intralayer Rashba spin-orbit coupling term [a] of strength λ that explicitly breaks inversion symmetry. At the side surfaces we observe the conventional surface Dirac cones of a weak topological insulators [c.f. Fig. 4.3(b)]. More importantly, diagonalization of the Hamiltonian with open boundary conditions along the stacking direction [c.f. Fig. 4.3(c)] reveals the presence of two $\mathcal{C}_2$ symmetry protected surface Dirac cones thus verifying that our model realizes a hybrid-order weak topological insulator. Note that the pairs of Dirac cones at the (001) and $(00\bar{1})$ surface are found at different surface momenta in agreement with the lack of inversion symmetry.

We have also verified that our model can be switched to a higher-order topological insulator by suitable translational symmetry breaking perturbations. Specifically we have introduced an interlayer staggered chemical potential of strength ϵ that provides the required doubling of the unit cell and further introduced an interlayer coupling in the enlarged unit cell of the form $-\delta\tau_z s_x$. Fig. 4.4(a) shows the corresponding bulk bandstructure that is still characterized by a substantial gap. At the (010) $[(0\bar{1}0)]$ surface the time-reversal symmetry protected Dirac cones are gapped out [see Fig. 4.4(b)] while the twofold rotation symmetry-protected Dirac cones at the (001) $[(00\bar{1})]$ surface are preserved [see Fig. 4.4(c)]. Notice that Dirac cone pairs localized at opposite surface are connected by helical hinge states [see Fig. 4.4(d)] as expected for a helical higher-order topological insulator protected by a twofold rotation symmetry.

[a] The term is $[-1/2+\cos(k_2)-\cos(k_1)]\tau_y\otimes s_x+[\sin(k_2)-\sin(k_1)/2]\tau_x\otimes s_x+[\sqrt{3}/2(\cos(k_1)-1)]\tau_y\otimes\sigma_y+[\sin(k_1)\sqrt{3}/2]\tau_x\otimes s_y$

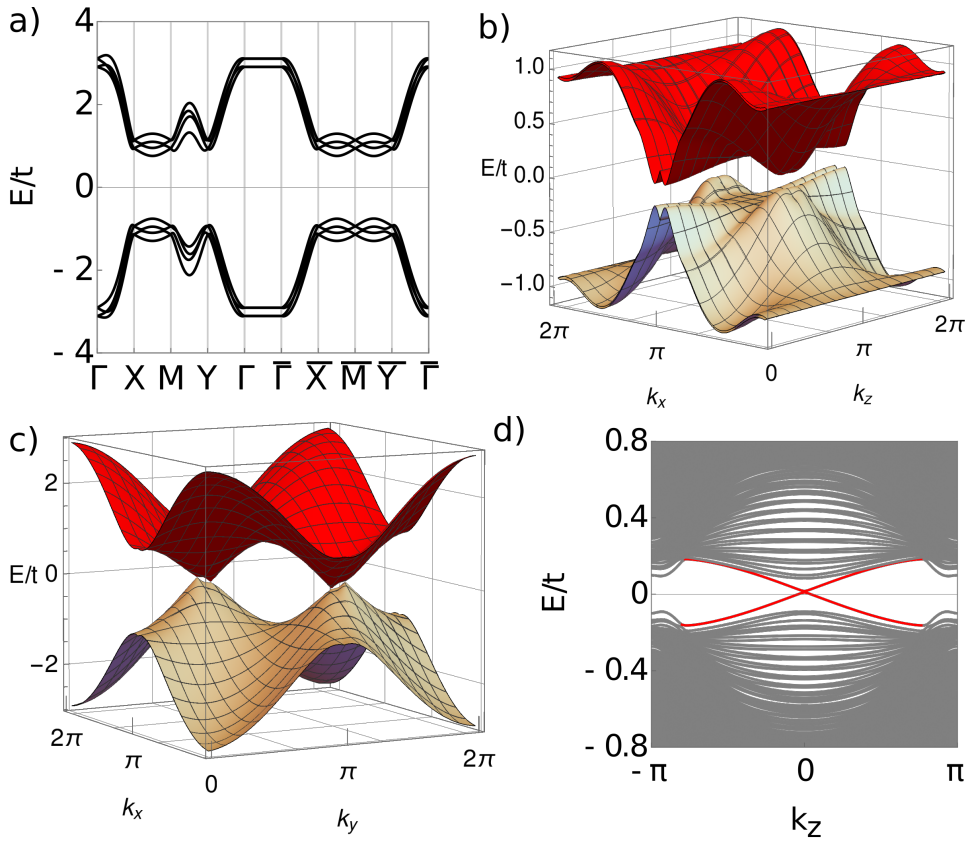

Figure 4.4: (a) Bulk band structure of the stacked Kane-Mele model with a translational breaking perturbation. The parameter set is the same as in Fig. 4.3. Moreover the translational symmetry breaking parameters have been fixed to $\epsilon/t = 0.1$ and $\delta/t = 0.2$. (b) Surface energy spectrum showing the gapping of the time-reversal symmetry protected Dirac cones. (c) Surface energy spectrum along the stacking direction that still feature the $\mathcal{C}_2$-protected Dirac cones at unpinned surface momenta. (d) Energy spectrum in a ribbon geometry with periodic boundary conditions only along the stacking direction. Within the surface energy gap we find gapless anomalous helical hinge modes, colored in red.

4.4 Conclusions

To sum up, we have shown that weak topological insulators with an additional twofold rotation symmetry around the dark direction can feature a pair of Dirac cones on their dark surfaces, which are protected by the rotation symmetry. This hybrid-order weak topological insulator can be turned into a higher-order topological insulator with protected helical hinge modes by translational symmetry breaking perturbations. We have shown that the existence of such a topological phase comes about due to a third $\mathbb{Z}_2$ topological invariant characterizing quantum spin-Hall insulators in $\mathcal{C}_2$-symmetric crystals, that can be read off neither from symmetry indicators nor from the properties of the Wilson loop spectrum. Considering the minimal symmetry requirements and the fact that the $\mathcal{C}_2$ protected surface Dirac cones appear at unpinned points in the surface Brillouin zone, we anticipate that our findings could apply to a large number of weak topological insulators.

Appendix A: Constructing $\mathcal{C}_2$-symmetric channels for pairs of isolated Kramers pairs

Our goal is to numerically construct, for systems with $\mathcal{C}_2$ and time-reversal symmetry, a gauge that divides our system in two channels that are by themselves $\mathcal{C}_2$ symmetric, and are related to each other by time-reversal Θ, and consequently $\mathcal{C}_2\Theta$ symmetry. Since we are assuming that there are no other degeneracies than those required by time-reversal symmetry, it is sufficient to consider a single Kramers pair of bands. We then want to find a gauge such that we have two states ψ_k^I and ψ_k^{II} that satisfy

$$\mathcal{C}_2\Theta\psi_k^I = \psi_k^{II}, \tag{4.2}$$

$$\mathcal{C}_2\psi_k^{I,II} = \psi_{-k}^{I,II}. \tag{4.3}$$

To construct such a gauge, let us first see how to construct locally, at each k-point, a gauge that satisfies Eq. (4.2). To do so we start by numerically diagonalizing the Hamiltonian to find the two occupied eigenstates $\Psi_k^{I,II}$. We then calculate the unitary matrix $M^{ij} = \Psi_k^{i\dagger}\mathcal{C}_2\theta\Psi_k^j$ and diagonalize it by a transformation $\psi_k^i = U_k^{ij}\Psi_k^j$,where U_k^{ij} consists of the eigenvectors of M^{ij}. The matrix M then has the form

$$M = \begin{pmatrix} e^{i\rho_1} & 0 \\ 0 & e^{i\rho_2} \end{pmatrix}.$$

After a further unitary transformation $\psi_k^{1,2} \to e^{i\rho_{1,2}/2}\psi_k^{1,2}$, M will be the identity matrix. A final unitary transformation

$$\begin{pmatrix} \psi_k^I \\ \psi_k^{II} \end{pmatrix} \to \frac{1}{\sqrt{2}} \begin{pmatrix} -1 & 1 \\ 1 & 1 \end{pmatrix} \begin{pmatrix} \psi_k^I \\ \psi_k^{II} \end{pmatrix},$$

then ensures M is completely off-diagonal, and thus we have found states ψ_k^I and ψ_k^{II} that satisfy Eq. (4.2).

In order to construct a gauge satisfying Eqs. (4.2) and (4.3) across the Brillouin zone, let us start by noting that for an isolated Kramers pair of bands, the local gauge freedom is $U(1) \otimes SU(2)$. That is, we are free to do a rotation between the basis states, and can then change each basis state by a $U(1)$ phase. Now the conditions of Eqs. (4.2) and (4.3) completely fix the

$SU(2)$ part of the gauge freedom, up to the unitary operation of relabeling the states $\psi_k^I \longleftrightarrow \psi_k^{II}$. There will thus be a remaining $U(1)$ degree of freedom within each $\mathcal{C}_2$ symmetric channel.

We can now start at the Γ point in the Brillouin zone at $k = (0, 0)$, and follow the steps described to make the matrix M off-diagonal. Since Γ is a time-reversal invariant point, Kramers theorem guarentees that the time-reversal operator θ is off-diagonal. Rotating such that $C_2\theta$ is off-diagonal thus also ensures that this basis is C_2 diagonal.

Once we have found the states at the Γ point, we take a point close to it at $k = (\epsilon, 0)$ for a small ϵ and repeat the procedure to make M off-diagonal. We then consider the overlap matrix $\psi^i_{(0,0)}\psi^j_{(\epsilon,0)}$, which will either be almost completely diagonal, or almost completely off-diagonal. If it is off-diagonal, this means that we need to switch the labels I, II by a unitary transformation

$$\begin{pmatrix} \psi_k^I \\ \psi_k^{II} \end{pmatrix} \to \begin{pmatrix} 0 & 1 \\ 1 & 0 \end{pmatrix} \begin{pmatrix} \psi_k^I \\ \psi_k^{II} \end{pmatrix}.$$

We then define $\psi^i_{-k} = \mathcal{C}_2\psi^i_k$. Continuing in this way along half the Brillouin zone also ensures that the second condition Eq. (4.2) is satisfied.

The gauge constructed in this way fixes the $SU(2)$ part of the gauge degrees of freedom, since we ensured that the overlap matrix is diagonal. Within each channel, there is still a $U(1)$ phase degree of freedom which we have not fixed, and for which there is an obstruction to smoothness if the band has a non-zero Chern number. For our purposes we do not need to fix this phase, as neither the eigenvalues nor the Chern number can change under this $U(1)$ gauge transformation

Appendix B:Topological invariants of systems with two-fold rotational symmetry

Using the procedure of the previous section, we can divide the occupied bands of a system into two channels that are tow-fold rotation symmetric, and have broken time-reversal symmetry. In this section we show how one can compute the topology of the system once such a gauge has been found.

First consider the partial polarizations, which are quantized along the

high-symmetry lines of the BZ by $\mathcal{C}_2$ and time-reversal symmetry. Using the constructed gauge, the two $\mathcal{C}_2$-symmetric channels give us an easy way to compute the partial polarizations. Since the two channels are related by time-reversal symmetry, the partial polarization is equal to the polarization in one channel. This means we have to calculate the Berry phase of one channel along high-symmetry lines in the BZ. On these contours, each channel is effectively a one-dimensional system with $\mathcal{C}_2$ symmetry. For such systems, the Berry phase γ is quantized and can directly be expressed in terms of its $\mathcal{C}_2$-eigenvalues as [126]

$$\gamma = (-i) \prod_i^{N_F} \log[-\xi_i(0)\xi_i(\pi)] \mod 2\pi,$$

where $\xi_i(k)$ is the $\mathcal{C}_2$ eigenvalue of band i at momentum k. Since the eigenvalues can be either $\pm i$, the term inside the logarithm can either be $\pm$ and hence each term inside the product is either 0 or π. This allows us to rewrite

$$\begin{aligned}
\gamma &= \sum_i^{N_F} -i \log[-\xi_i(0)\xi_i(\pi)] \mod 2\pi \\
&= \sum_i^{N_F} -i(\log[i\xi_i(0)] + \log[i\xi_i(\pi)]) \mod 2\pi \\
&= -i \sum_i^{N_F} \log[i\xi_i(0)] - i \sum_i^{N_F} \log[i\xi_i(\pi)]) \mod 2\pi \\
&= \pi(m_i^{k=0} + m_i^{k=\pi}) \mod 2\pi,
\end{aligned}$$

Where $m_i^{k=0}$ denotes the multiplicity of eigenvalue i at $k = 0$ and the last equality follows since whenever an eigenvalue is $-i$, the log evaluates to zero.

Applying this to the contours $\Gamma - X$ and $\Gamma - Y$ we find $\gamma^I_{1(2)} \equiv \left[\Gamma^I_i + X^I_i(Y^I_i)\right] \mod 2$ as presented in the main text.

The Fu-Kane-Mele invariant is equal to the Chern number in one of the channels modulo 2. This Chern number can in turn be expressed as the

difference of the berry phases of the contours $\Gamma - Y$ and $X - M$ (CITE). Hence the FKM-invariant can be expressed as

$$\nu_{\mathrm{FKM}} = (\Gamma_i^I + X_i^I + Y_i^I + M_i^I) \mod 2$$

So far we have found three invariants constructed out of four eigenvalue multiplicities. For atomic insulators, a fourth linearly independent crystalline invariant is given by [8]

$$\nu_{1d} = \frac{1}{2}(\Gamma_{-i} - X_{-i} - Y_{-i} + M_{-i}),$$

where m_{-i} is the multiplicity of eigenvalue $-i$ at high-symmetry point $m = \Gamma, X, Y, M$.

This invariant is related to the number of Wannier functions localized at Wyckoff position $1d$ in real space by [8]

$$\nu_{1d} = -N_{1d;i} + N_{1d;-i}$$

where $N_{1d;i}$ is the number of symmetric Wannier functions localized at Wyckoff position $1d$ with two-fold rotation eigenvalue i. When considering non-atomic insulators, one cannot find localized symmetric Wannier functions, however we can still calculate ν_{1d}. For systems with an odd Chern number ν_{1d} will be half-integer, since there will be an odd number of i eigenvalues, and an odd number of $-i$ eigenvalues. Hence we can construct an invariant that is always integer by the combination

$$\gamma_3 = (\mathcal{C}/2 + \nu_{1d}) \mod 2.$$

Appendix C: Sums of quantum spin Hall insulators

Here we explicitly show how adding together and coupling two QSHI can result in either a fragile topological phase or a trivial phase. To this end we

consider a Kane-Mele model,

$$\begin{aligned}\mathcal{H}_{KM}(t,t_2) = &-t\left[1+\cos(k_1)+\cos(k_2)\right]\tau_x\otimes s_0\\ &-t\left[\sin(k_1)+\sin(k_2)\right]\tau_y\otimes s_0+2t_2\sin(k_1)\,\tau_z\otimes s_z,\end{aligned}$$

where t and t_2 are the nearest-neighbor and intrinsic spin-orbit coupling amplitudes, and τ_i and s_i are Pauli matrices acting in sub-lattice and spin-space. We also add a Rashba coupling

$$\begin{aligned}\mathcal{H}_R =&\lambda\Big\{[-1/2+\cos(k_2)-\cos(k_1)]\tau_y\otimes s_x\\ &+[\sin(k_2)-\sin(k_1)/2]\tau_x\otimes s_x+[\sqrt{3}/2(\cos(k_1)-1)]\tau_y\otimes\sigma_y\\ &+[\sin(k_1)\sqrt{3}/2]\tau_x\otimes s_y\Big\},\end{aligned}$$

where λ is the Rashba amplitude. Note that the intrinsic spin-orbit coupling term only acts along k_1 such that threefold rotation symmetry is broken.

We now take two copies of this model, and couple them by adding a term $-\delta i\sigma_x\otimes\tau_x\otimes s_y$, where δ is the amplitude of the coupling and σ_x is a Pauli matrix acting in "copy" space. Let us denote the parameters of the two copies by t^i and t_2^i , where $i=1,2$ denotes the copy. To examine the phase that results from coupling the two QSHI, we consider its Wilson loop spectrum along k_1 (see main text). Let us first consider the parameters of the two Kane-Mele models to be equal and such that the system is insulating. This leads to a Wilson loop spectrum as in Fig. 4.6(a), showing this is an atomic insulator with two Kramers pairs at unpinned points in the BZ. Changing the sign of t_2 between the copies, such that $t_2^1=-t_2^2$ and keeping the sign of t the same, results in a fragile topological phase [see Fig. 4.6(b)]. Note that when turning off Rashba coupling, such that we restore inversion symmetry, the two copies have the same inversion eigenvalues, meaning this phase or γ_3 cannot be diagnosed by inversion. To obtain this phase, we can also instead change the sign of t between the copies such that $t^1=-t^2$, while keeping the sign of the other parameters equal. Changing both the sign of t and t_2 between the two copies again results in the trivial phase.

Finally, we note that when taking the hybrid-order topology model and adding translational-symmetry breaking perturbation (as presented in the main text), the resulting system at $k_z=0$ will be fragile topological insulator with Wilson loop Fig. 4.6(b), while at $k_z=\pi$ it will be a trivial insulator

with Wilson loop Fig. 4.6(a).

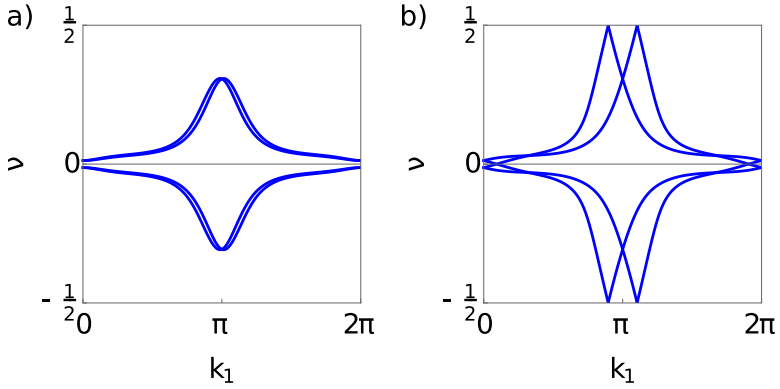

Figure 4.5: (a) Wilson loop spectrum of two coupled Kane-Mele models for $t^2 = t^1$, $t_2^1/t^1 = t_2^2/t^1 = 0.7$, $\lambda/t^1 = 0.2$ and $\delta/t^1 = 0.4$. (b) Wilson loop spectrum for the same model as in a), changing only $t_2^1/t^1 = -t_2^2/t^1 = 0.7$.

Appendix D: Spectral flow in the hybrid-order topological insulator

In general protected edge states can be detected by studying the WIlson loop spectrum along the momentum direction perpendicular to the surface [122]. For the hybrid-order topological insulator, the $\mathcal{C}_2$-related cones on the top and bottom surfaces can be detected by considering the Wilson loop along k_z, as a function of k_1 and k_2. This is plotted in Fig. 4.6 for the hybrid-order topological insulator presented in the main text. Here we see two protected gap-closing points that are related by $\mathcal{C}_2$ symmetry.

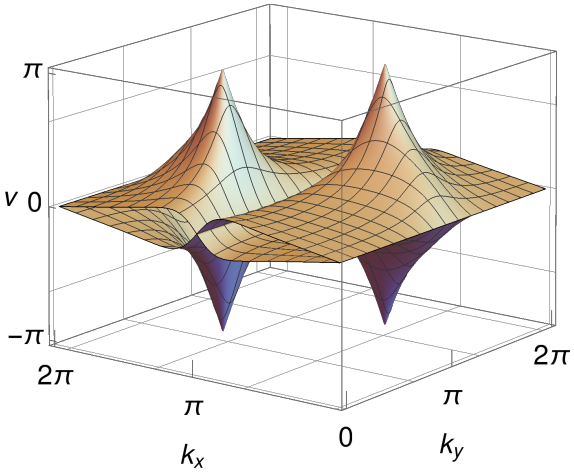

Figure 4.6: Wilson loop spectrum along k_z plotted as a function of k_1 and k_2 of the hybrid-order topological insulator presented in the main text. Two $\mathcal{C}_2$ related band crossings indicate gapless modes on the top and bottom surfaces.

5 The Floquet Hofstadter butterfly

The complex fractal structure of the Hofstadter butterfly, which reveals the interplay between the lattice constant and the magnetic length when a perpendicular magnetic field is applied to a crystal lattice, has fascinated researchers since its first theoretical prediction [127]. However, its experimental realization seemed to be impossible at first sight, because for typical crystal lattice spacings, the magnetic field required to observe the butterfly is of the order of thousands of tesla. Recently, moiré superlattices, obtained when depositing graphene on mismatched substrates, such as hBN, have been realized [128, 129]. These structures have an effective lattice spacing that is an order of magnitude larger than the usual crystal lattices. This has brought the required magnetic-field strength within experimental reach, and enabled the observation of the Hofstadter butterfly spectra [130, 131]. In addition, the Hofstadter butterfly has been proposed in nanophotonic devices [132], and for bosons in optical lattices [133–135], where it has also been experimentally realized [136, 137].

All these studies were done in equilibrium, and so far out-of-equilibrium Hofstadter setups have not received much attention, although driven systems have been under intense scrutiny recently [138–153]. In particular, time-periodic driving attracted great interest because it can be conveniently described in the framework of Floquet theory [138, 140, 154, 155]. This allows one to define quasi-static properties of the driven system that can be measured, and is a tuning knob for quantum simulations both in condensed-matter and cold-atom experiments. The quasi-energy spectrum obtained using Floquet theory is periodic, with a period proportional to the driving frequency. Recently, periodically driven systems have been observed in photonics [146], condensed-matter [147], and cold-atom experiments [148, 156].

Periodic driving described by Floquet theory can lead to many interesting topological phase transitions [139–144, 157], characterized by a slightly different topological invariant than for the undriven case [158–161]. For example, Floquet theory predicts additional topological phases in the Kitaev chain [145]. Topological behavior induced by periodic driving has been ob-

served experimentally in photonic waveguides [146], and a gap opening has been detected on the surface of a topological insulator upon irradiation with circularly polarized light [147]. The Berry curvature of such Floquet Bloch bands has also been explicitly measured [148].

Several recent works have been dedicated to the investigation of the driven Hofstadter model. In Refs. [151, 152], the driven Hofstadter model has been investigated on a square lattice for a specific flux $\phi = 1/3$ (in units of the flux quantum $\phi_0 = h/e$), and for two different driving protocols. In both cases, the authors find counter-propagating edge modes in the quasi-energy spectrum, crossing $E = \pm\pi\hbar/T$, where T is the period of the driving. The Hofstadter butterfly for a driven honeycomb lattice has been studied in Ref. [162], with an extensive Chern number analysis. In Ref. [153], a transition from the half-integer to the integer quantum Hall effect has been theoretically proposed to occur upon elliptical driving of an ac field.

Here, we show that the Floquet method can be used to unveil the formation of the Hofstadter butterfly at low magnetic fields by adding a periodic driving. Upon tuning the frequency, the bands start to overlap and avoided

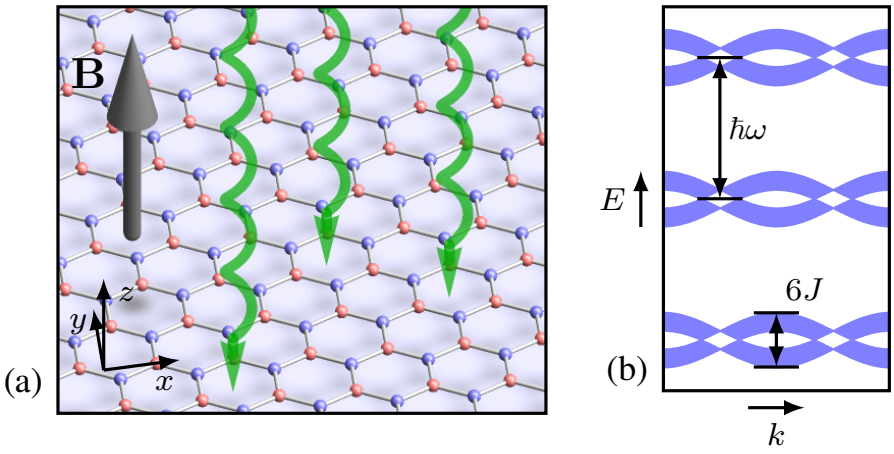

Figure 5.1: (a) Schematic setup of our model. The honeycomb lattice is subjected to a perpendicular magnetic field, and is simultaneously irradiated by circularly polarized light. (b) Quasi-energy spectrum of the Floquet model. The generic feature of the Floquet spectrum is the periodicity with $\hbar\omega$ in the vertical direction.

crossings occur, that lead to the formation of wings. At small flux, where the spectrum has a Landau-level structure, the procedure can be analytically monitored using the Floquet formalism. In doing so, we gain insight on the mechanism of hybridization between Landau levels. For larger magnetic fields, we perform numerical calculations to obtain the full butterfly spectrum for various frequencies.

The outline of this chapter is as follows. In Sec. 5.1, we introduce the model and explain the details of Floquet theory. In Sec. 5.2, we present numerical results for the small-flux regime and derive an effective model to explain the mixing of the Landau levels. In Sec. 5.3, we present and analyze our numerical results for the full range of flux, in both high- and low-frequency regimes. Our findings are summarized in Sec. 5.4.

5.1 The model

We consider a honeycomb lattice (e.g., a graphene monolayer) subject to a perpendicular magnetic field and to irradiation by circularly polarized light [see Fig. 5.1(a)]. The system is described by a tight-binding model of electrons on a honeycomb lattice, where the background magnetic field and the circularly polarized light are included through a vector potential $\mathbf{A}$, via Peierls substitution. The Hamiltonian reads

$$H = -J \sum_{l=1,2,3} \sum_{\mathbf{r}} |\mathbf{r} + \delta_l\rangle e^{i \int d\mathbf{s}\cdot\mathbf{A}} \langle \mathbf{r}| + \text{H.c.}, \tag{5.1}$$

where J is the hopping parameter, $\mathbf{r}$ is the position of a site, δ_l are the nearest-neighbor vectors of the honeycomb lattice, and $d\mathbf{s}$ parametrizes the path between two sites $\mathbf{r}$ and $\mathbf{r} + \delta_l$. The vector potential consists of two contributions,

$$\mathbf{A}(\mathbf{r}, t) = \mathbf{A}_{\text{mag}}(\mathbf{r}) + \mathbf{A}_{\text{light}}(t). \tag{5.2}$$

The first term is due to the background magnetic field, which will be described in the Landau gauge,

$$\mathbf{A}_{\text{mag}}(\mathbf{r}) = -\frac{e}{\hbar}(By,\, 0), \tag{5.3}$$

where e is the electron charge and $\hbar$ the reduced Planck constant. The second contribution comes from the circularly polarized light and is periodic in time,

$$\mathbf{A}_{\text{light}}(t) = A_0 \left(-\sin(\omega t), \cos(\omega t)\right), \tag{5.4}$$

where A_0 is the amplitude, ω is the frequency of the light and t denotes time.

Let us start by considering the static Hamiltonian, with $\mathbf{A}_{\text{light}} = 0$. A Fourier transformation then yields the Harper equation of the honeycomb lattice (we set the lattice spacing to unity):

$$\begin{aligned} -\frac{E}{J}\begin{pmatrix}1 & 0\\ 0 & 1\end{pmatrix}\psi_r(k) = {} & \begin{pmatrix}0 & 1\\ 1 & 0\end{pmatrix}\psi_r(k) \\ & + e^{i\frac{\sqrt{3}}{2}k_x}\begin{pmatrix}0 & e^{\frac{3}{2}i\left(k_y+\frac{2}{3}\pi\frac{rp}{q}\right)}\\ e^{-\frac{3}{2}i\left(k_y+\frac{2}{3}\pi\frac{rp}{q}\right)} & 0\end{pmatrix}\psi_{r+1}(k) \\ & + e^{-i\frac{\sqrt{3}}{2}k_x}\begin{pmatrix}0 & e^{\frac{3}{2}i\left(k_y+\frac{2}{3}\pi\frac{rp}{q}\right)}\\ e^{-\frac{3}{2}i\left(k_y+\frac{2}{3}\pi\frac{rp}{q}\right)} & 0\end{pmatrix}\psi_{r-1}(k), \end{aligned} \tag{5.5}$$

where $r = 1, \ldots, q$, and $\psi_{q+1} = \psi_1$, with

$$\psi_r(k) = (a_{r,k_x,k_y}, b_{r,k_x,k_y}). \tag{5.6}$$

Here, a and b are the annihilation operators of the two sublattices

$$\psi_r(k) = \left(\psi^{\text{A}}_{r,k_x,k_y}, \psi^{\text{B}}_{r,k_x,k_y}\right). \tag{5.7}$$

Here, the components ψ^{A} and ψ^{B} refer to the two sublattices of the honeycomb lattice, and we have taken the flux per unit cell to be $\phi = p/q$ in units of the flux quantum ϕ_0, where p and q are co-prime integers. Thus, the matrices in the Harper equation [Eq. (5.5)] act in sublattice space.

To describe the influence of the circularly polarized light, we now also

consider $\mathbf{A}_{\text{light}}$. This will amount to each hopping picking up a phase,

$$\mathrm{e}^{i\int d\mathbf{s}\cdot\mathbf{A}_{\text{light}}} = \exp\left\{iA_0\left[-\cos(\theta)\sin(\omega t)+\sin(\theta)\cos(\omega t)\right]\right\}, \tag{5.8}$$

where θ is the angle between the bond and the x-axis. Since the Hamiltonian is now periodic in time, we can define the Floquet Hamiltonian by [138]

$$H_{\text{Floq}} = \frac{i\hbar}{T}\ln\left[U(T,0)\right]. \tag{5.9}$$

Here, $T = 2\pi/\omega$ is the period of the driving and $U(T,0)$ is the time-evolution operator, which may be found by numerically solving the Schrödinger equation

$$i\hbar\frac{\partial U(t,t')}{\partial t} = H(t)\,U\left(t,t'\right). \tag{5.10}$$

By calculating the eigenvalues and eigenstates of H_{Floq}, we can determine the quasi-static behavior of the system at stroboscopic timescales larger than T. The time-periodic Hamiltonian can thus be expanded into the Fourier coefficients H_n, as

$$H(t) = \sum_n H_n \mathrm{e}^{in\omega t}. \tag{5.11}$$

The eigenenergies of the Floquet Hamiltonian then follow from diagonalization of

$$H_{\text{Floq}} = \begin{pmatrix} \ddots & \vdots & \vdots & \vdots & \iddots \\ \cdots & H_0+\hbar\omega & H_1 & H_2 & \cdots \\ \cdots & H_{-1} & H_0 & H_1 & \cdots \\ \cdots & H_{-2} & H_{-1} & H_0-\hbar\omega & \cdots \\ \iddots & \vdots & \vdots & \vdots & \ddots \end{pmatrix}. \tag{5.12}$$

We can interpret the Hamiltonian Eq. (5.12) as an infinite set of copies of the Hamiltonian H_0, separated by energies $\hbar\omega$, as illustrated by Fig. 5.1(b). These copies are then mixed by the off-diagonal elements. If $\hbar\omega$ is much larger than the bandwidth $6J$ of the spectrum of H_0, this mixing will be negligible. However, when $\hbar\omega$ becomes comparable to $6J$, the different copies

of H_0 start to overlap and the mixing terms become important.

For high frequencies, the Floquet Hamiltonian can be expanded to first non-trivial order as [138, 157, 163–166]

$$H_{\text{Floq}} \approx H_0 + [H_{-1}, H_1]/\hbar\omega. \tag{5.13}$$

5.2 Landau-level regime

We will first focus our attention to the small-flux limit, where the Hofstadter spectrum typically exhibits a Landau-level structure. In Fig. 5.2, we plot the energies as a function of the flux ϕ for different values of the driving frequency ω. We consider the regime where the frequency becomes comparable to the bandwidth $6J$. In Fig. 5.2(a), for $\hbar\omega = 5.2J$, we observe that two subsequent copies of H_0 are still well separated. (The two copies shown here live in the intervals $[-\hbar\omega/2, \hbar\omega/2]$ and $[\hbar\omega/2, 3\hbar\omega/2]$, respectively.) The coupling between the two copies reduces their width to a value smaller than $6J$. Upon lowering the frequency, the two copies of bands come closer to each other and start to overlap. We see this process in Figs. 5.2(c)-(h). In Figs. 5.2(b) and 5.2(c), the initial overlap of the bands takes place. Curiously, the top two Landau levels of the lower copy do not mix with any Landau level of the upper copy, while the rest hybridizes and a gap opens due to their avoided crossings. We will explain this behavior in the next section using an effective model to describe this regime. In Figs. 5.2(e)-(h), one sees additional gaps opening, and one observes that the two largest gaps acquire a shape that resembles the wings of the undriven Hofstadter butterfly.

5.2.1 Effective model

We now derive an effective model to describe the initial overlap of the two copies of bands displayed in Figs. 5.2(b)-(d), aiming at understanding why the top two bands of the lower copy do not hybridize with the bands of the upper copy. To do so, we zoom in around $E \approx \hbar\omega/2$, where the overlap occurs. Our starting point is the Hamiltonian in Eq. (5.12). Since we are interested in the regime where two copies start overlapping, $\hbar\omega \lesssim 6J$, at energy $E \approx \hbar\omega/2$, we can restrict ourselves to two copies of H_0. Here, we take the ones centered at $E = 0$ and $E = \hbar\omega$, and consider their mixing, of which the dominant contribution stems from H_1 and H_{-1}. The mixing with

levels in more distant Floquet copies is negligible, as the effect is suppressed with increasing energy difference. (A similar analysis is done in Ref. [161].) The effective Hamiltonian then becomes

$$H_{\text{Floq}}^{\text{eff}} = \begin{pmatrix} H_0 + \hbar\omega & H_1 \\ H_{-1} & H_0 \end{pmatrix}. \tag{5.14}$$

To derive analytical expressions for H_n, with $n = -1, 0, 1$, we initially solve the problem at zero dc magnetic field ($\phi = 0$), including only the time-dependent perturbation. In this case, H_n can be obtained by making the following substitution in the Hamiltonian,

$$\begin{aligned} J \to \frac{J}{T}\int_0^T dt' \exp\Big\{ iA_0\Big[-\cos(\theta)\sin\left(\omega t'\right) + \sin(\theta)\cos\left(\omega t'\right)\Big]\Big\} \exp\left\{in\omega t'\right\} \\ = J\, J_n\left(A_0\right) \exp\left[in\left(\theta + \frac{\pi}{2}\right)\right], \end{aligned} \tag{5.15}$$

where J_n is the nth Bessel function of the first kind. Applying this substitution to the tight-binding Hamiltonian [Eq. (5.1)] of the honeycomb lattice, we obtain

$$H_n = \begin{pmatrix} 0 & h_n \\ h_n' & 0 \end{pmatrix}, \tag{5.16}$$

where

$$\begin{aligned} h_n &= -J\left(\mathrm{e}^{i\left(k_y\frac{1}{2}+k_x\frac{\sqrt{3}}{2}\right)}\mathrm{e}^{in\frac{5}{6}\pi} + \mathrm{e}^{i\left(k_y\frac{1}{2}-k_x\frac{\sqrt{3}}{2}\right)}\mathrm{e}^{in\frac{\pi}{6}} + \mathrm{e}^{-ik_y}\mathrm{e}^{in\pi\frac{3}{2}}\right) J_n\left(A_0\right), \\ h_n' &= -J\left(\mathrm{e}^{-i\left(k_y\frac{1}{2}+k_x\frac{\sqrt{3}}{2}\right)}\mathrm{e}^{-in\frac{\pi}{6}} + \mathrm{e}^{-i\left(k_y\frac{1}{2}-k_x\frac{\sqrt{3}}{2}\right)}\mathrm{e}^{-in\frac{5}{6}\pi} + \mathrm{e}^{ik_y}\mathrm{e}^{in\frac{\pi}{2}}\right) J_n\left(A_0\right). \end{aligned}$$

At small ϕ, we enter the Landau-level regime. Because of the suppression of the mixing with energy difference, the strongest overlap occurs between the highest and lowest Landau levels of two neighboring Floquet copies. This observation justifies an expansion of the Hamiltonian around the maximum of the spectrum at $\mathbf{k} = 0$. The dispersion is quadratic in leading order, and we find

$$H_0 = -3JJ_0\left(A_0\right)\left[1 - \frac{1}{4}\left(k_x^2 + k_y^2\right)\right]\sigma_x, \tag{5.17}$$

where σ_x is a Pauli matrix in the sublattice pseudospin space, and we have omitted the higher order terms. We now introduce the magnetic field by minimal Peierls substitution, and then the standard ladder operators a and $a^\dagger$ to find

$$H_0 = -3JJ_0\left(A_0\right)\left[1 - \frac{1}{2l_B^2}(a^\dagger a + \tfrac{1}{2})\right]\sigma_x, \tag{5.18}$$

where $l_B = \sqrt{\hbar/eB}$ is the magnetic length in terms of the magnetic field B. (We recall that the lattice spacing has been set to unity.) The term H_1, mixing two copies of the butterfly spectrum, is obtained by a similar calculation,

$$H_1 = JJ_1\left(A_0\right)\frac{3}{2}\left[\frac{\sqrt{2}}{l_B}a^\dagger\sigma_x + \frac{1}{2l_B^2}aa\sigma_y\right]. \tag{5.19}$$

The eigenstates $\psi_{n,\pm}$ of H_0 have the same structure as the eigenstates of σ_x,

$$\psi_{n,\pm} = \frac{1}{\sqrt{2}}\begin{pmatrix} |n\rangle \\ \mp|n\rangle \end{pmatrix}, \tag{5.20}$$

and their energies are

$$E_{n,\pm} = \pm 3JJ_0\left(A_0\right)\left[1 - \frac{1}{2l_B^2}(n + \tfrac{1}{2})\right]. \tag{5.21}$$

These results are compatible with Ref. [161], which discusses the zero-field case.

One observes that for each Floquet copy, which we label by r in the following, there are two sequences of Landau levels: one where the zeroth Landau level is at the top of the spectrum, and one where it is at the bottom of the spectrum, labeled by $+$ and $-$, respectively. In H_1, the term proportional to σ_y couples $\psi_{n,+,r}$ with $\psi_{n',-,r+1}$ and $\psi_{n,-,r}$ with $\psi_{n',+,r+1}$. The former pair constitutes states very close in energy (energy difference $\Delta E \ll \hbar\omega$) whereas the latter pair are distant states ($\Delta E \approx 2\hbar\omega$). The term proportional to σ_x couples $\psi_{n,\pm,r}$ with $\psi_{n',\pm,r+1}$, whose energy difference is $\Delta E \approx \hbar\omega$. From perturbation theory, it follows that the energy shift due to the mixing term scales as $1/\Delta E$. Consequently, hybridization between the states $\psi_{n,+,r}$ and

$\psi_{n',-,r+1}$ is significant, whereas the couplings between the other pairs have negligible effects.

The strong mixing between $\psi_{n,+,r}$ and $\psi_{n',-,r+1}$ is due to the matrix element proportional to aa in Eq. (5.19). Thus, hybridization occurs between these states if $n' = n - 2$. In Figs. 5.2(c) and 5.2(d), we indeed observe that avoided crossings occur between the Landau levels labeled 0 (blue) and 2 (red), between 1 (blue) and 3 (red), etc. The top two Landau levels of the lower copy ($n = 0, 1$, labeled in red) do not have a partner; they do not hybridize with any of the bands of the upper copy (labeled in blue).

5.3 Numerical results

We now go beyond the low-flux regime and study the full Hofstadter butterfly. We present numerical results for both high frequencies, when the periodicity of the spectrum is much larger than the bandwidth, and lower frequencies, where overlaps are observed.

5.3.1 High-frequency regime

In Fig. 5.3, we plot the energy levels as a function of the flux per plaquette ϕ, for several values of the amplitude at a frequency of $\omega = 12J/\hbar$, such that the periodicity of the spectrum $\hbar\omega$ is larger than the bandwidth $\sim 6J$. Thus, there are only resonances within one Floquet copy of the spectrum.

The colors of the gaps correspond to the associated topological invariants, which are obtained by using the Středa formula [167]

$$\sigma_{\mathrm{H}} = 2\frac{e^2}{h}\frac{\partial N}{\partial \phi}, \tag{5.22}$$

which provides the Hall conductivity σ_{H}, in terms of the integrated density of states N and the conductance quantum e^2/h. We have checked and confirmed that the resulting values of σ_{H} from Eq. (5.22) are identical to those obtained by counting the number of chiral edge states in a ribbon-geometry calculation of the dispersion. Identical results can be obtained from explicit calculation of the Chern numbers [162, 168], however at a higher computational expense. Although the topological invariant of Floquet systems is not the same as for static systems [158], in the high-frequency

regime the Středa formula still yields the correct conductivity values because there is still a trivial gap between different copies of the original spectrum.

For $\phi = 0$ (no magnetic field), circularly polarized light opens up a topological gap in the honeycomb system, and realizes a dynamical Haldane model [142, 156, 169–171]. Since the spectrum is continuous as a function of ϕ, this gap must persist for non-zero ϕ. From Fig. 5.3, we see indeed that it connects with the large gap above $E = 0$, which also has topological invariant $+1$. If we create a gap with opposite winding number (by reversing the polarization of the light), the gap that opens up at $\phi = 0$ would connect to the lower large gap with invariant -1. At other fractional fluxes, such as $\phi = 1/2, 1/3, 1/4$, non-trivial gaps also open at $E = 0$ with the same chirality and with the topological invariant equal to the denominator of the rational flux.

As we increase the amplitude of the light A_0, we change the effective couplings $JJ_n(A_0)$ [see Eq. (5.15)] in the Floquet Hamiltonian, which induces additional topological phase transitions. These will happen by the closing and opening of a gap that already exists without driving [172]. An example can be observed at $\phi = 1/3$, where the large gap around $E \approx -1$ with invariant -1 becomes smaller for $A_0 = 1.3$, closes around $A_0 \approx 1.5$ and is reopened at $A_0 = 1.7$.

The gap closing occurs at three points in the Brillouin zone and the topological invariant changes from -1 to $+2$ (see colors in Fig. 5.3), consistent with the number of gap closing points. Because the system still has magnetic-translation symmetry, the topological invariant must satisfy the Diophantine equation [151, 173]

$$p\,c + q\,d = 1, \tag{5.23}$$

for flux $\phi = p/q$, where c is the topological invariant and d is integer. This means that the topological invariant can only change in multiples of q, which indeed agrees with our observation at the third gap for flux $\phi = 1/3$.

5.3.2 Higher photon resonances

As we lower ω, and $\hbar\omega$ becomes comparable to the bandwidth ($\lesssim 6J$), bands from the next copy will start interacting with each other (this regime in the case of $\phi = 0$ has been studied in Ref. [157]). We plot the spectrum for $A_0 = 1$ and various frequencies in Fig. 5.4. In Fig. 5.4(a) ($\hbar\omega = 5.6J$) there

is still a gap between the first and second copy of bands. In Fig. 5.4(b), the bands are at the verge of crossing, and in Fig. 5.4(c) ($\hbar\omega \ll 6J$) there is an overlap between the two copies. The mixing of the energy bands gives rise to an intricate spectrum, and also causes many topological phase transitions. One example is the gap that appears at $E \approx \hbar\omega/2$ around $\phi = 1/2$ in Fig. 5.4(c). Since the different copies are now starting to overlap, the periodicity of the spectrum makes it difficult to define a reference value for the filling (integrated density of states N) and the Středa formula no longer *a priori* provides the correct topological invariant. As we decrease ω even further, an almost flat band appears for small ϕ [see Fig. 5.4(d)], where the gap below (above) has Hall conductivity $+1(+2)$. In this regime, it is possible to clearly distinguish between two gaps with a different number of edge states (the one above has two, the gap below one), where the gap above the flat state has been created by the Floquet driving. This could facilitate experiments, since the narrow and flat band persists for a wide range of flux.

5.4 Conclusion

By irradiating a honeycomb lattice subjected to a perpendicular magnetic field with circularly polarized light, its Hofstadter butterfly exhibits an even richer structure than its static counterpart. In particular, we can follow the formation of wing-like structures in the spectrum at low flux and low frequencies. The highest two Landau levels of the spectrum do not mix with the overlapping copy, while the other levels do, as captured by our effective analytical model.

To realize these features experimentally, the Floquet perturbation and the flux per unit cell need to be large. The Floquet perturbations enter through Bessel functions as factors of (reintroducing the lattice constant c) $J_n(A_0 c)$, which shows that a larger lattice constant would increase the Floquet strength as well as the flux per unit cell. This makes honeycomb structures with large lattice constants a natural place to realize this system. Such structures can be for example lattices of nanocrystals [174, 175] or optical lattices [176]. In optical lattices, one can also implement shaking protocols [141, 177]. A circular shaking protocol will induce a vector potential of the same form as Eq. (5.4) [161, 178]. The amplitude, however, will grow linearly with the frequency ω, while for light $A_0 \sim eE/\hbar\omega$. As the

required frequencies are quite large, this will aid in an experimental realization. In such a setup $\hbar\omega \approx 2.7J$ can be realized, which would be sufficient to observe the newly formed wings.

The structures observed at the process of opening the wings are reminiscent of generic hybridized dispersions. For example, in semiconductor quantum wells (e.g., HgCdTe/HgTe) [155, 179, 180] , gaps open between Landau levels in the valence band. In that case, the "warping terms", which make the dispersion non-isotropic, induce a coupling between Landau levels with indices n and $n \pm 4$. The mechanism for the formation of these gaps is thus analogous to the one governing the wing formation in the present Floquet model. This analogy suggests a potential application of Floquet systems as simulator of band structures of generic condensed matter systems. In particular, such simulations could provide more insight into hybridization in complicated Landau-level spectra.

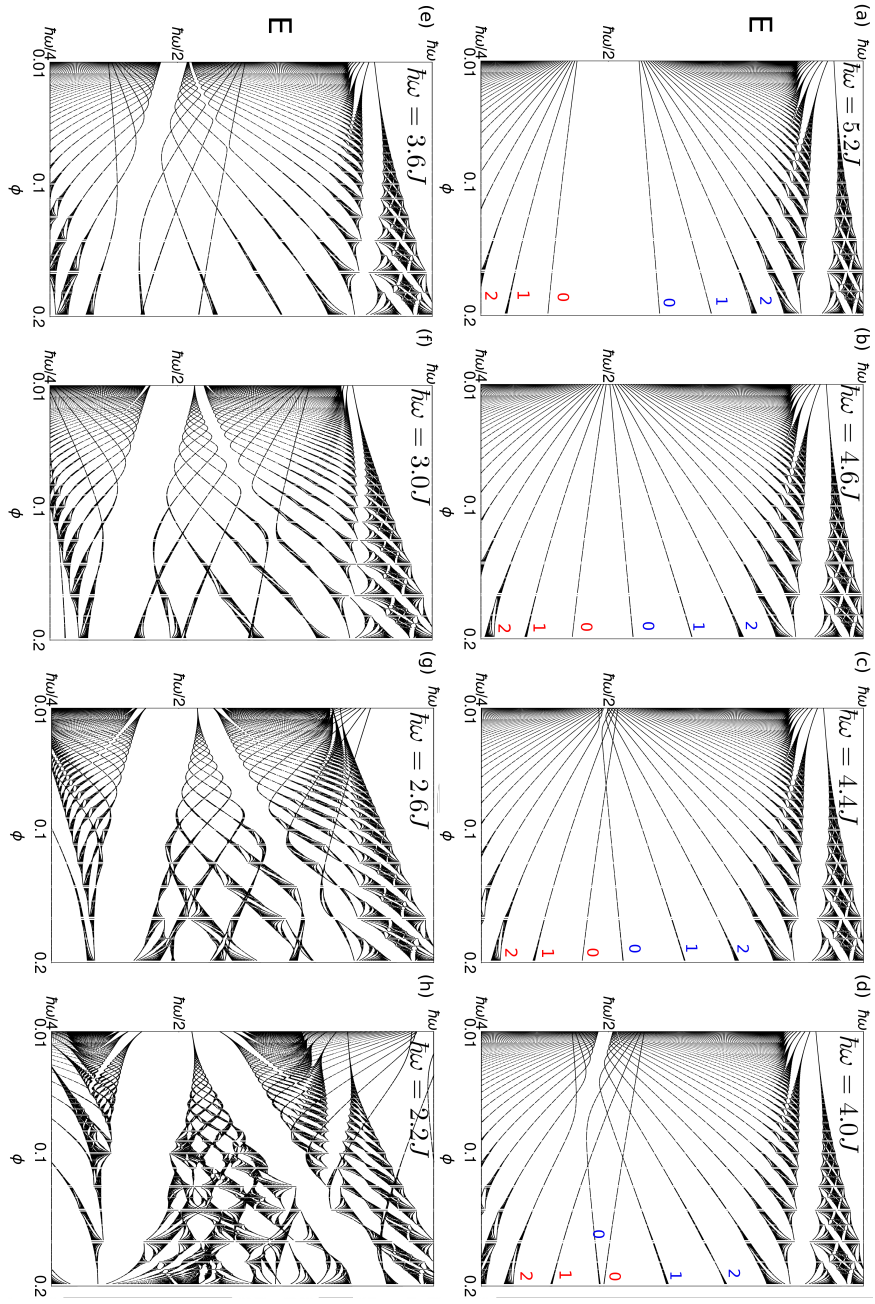

Figure 5.2: Spectra for small fluxes ϕ, in the Landau-level regime, plotted for various values of ω, with $A_0 = 1$. In the first four plots we label the first three Landau levels of the upper (blue) and lower (red) copy.

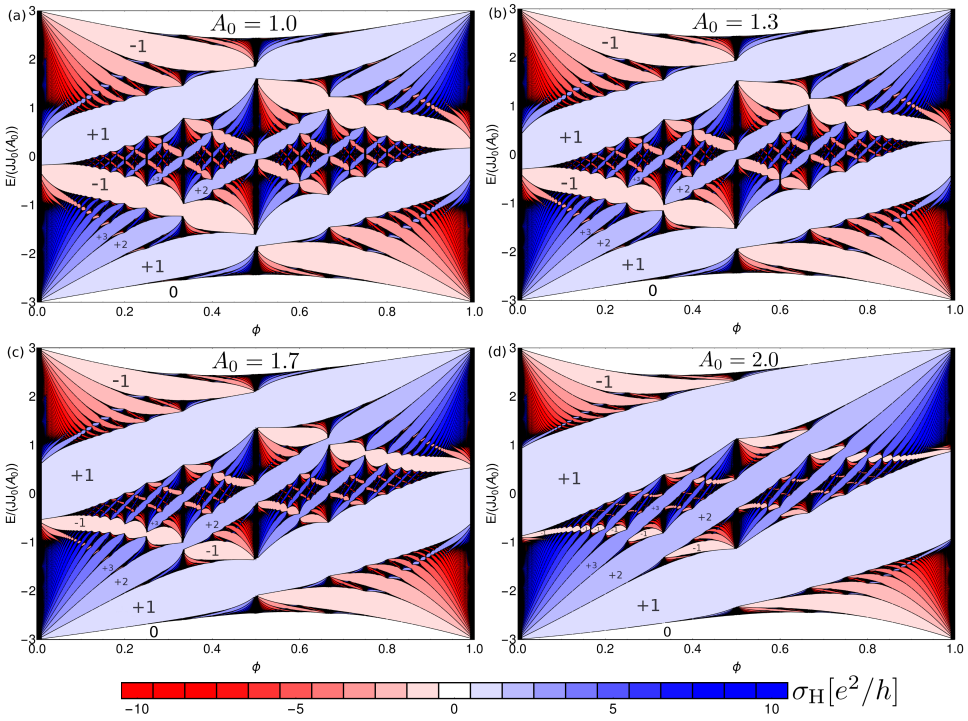

Figure 5.3: Full spectrum plotted for $\hbar\omega = 12J$ and various values of A_0. The colors of the gaps correspond to the number of left (red) or right (blue) moving edge states.

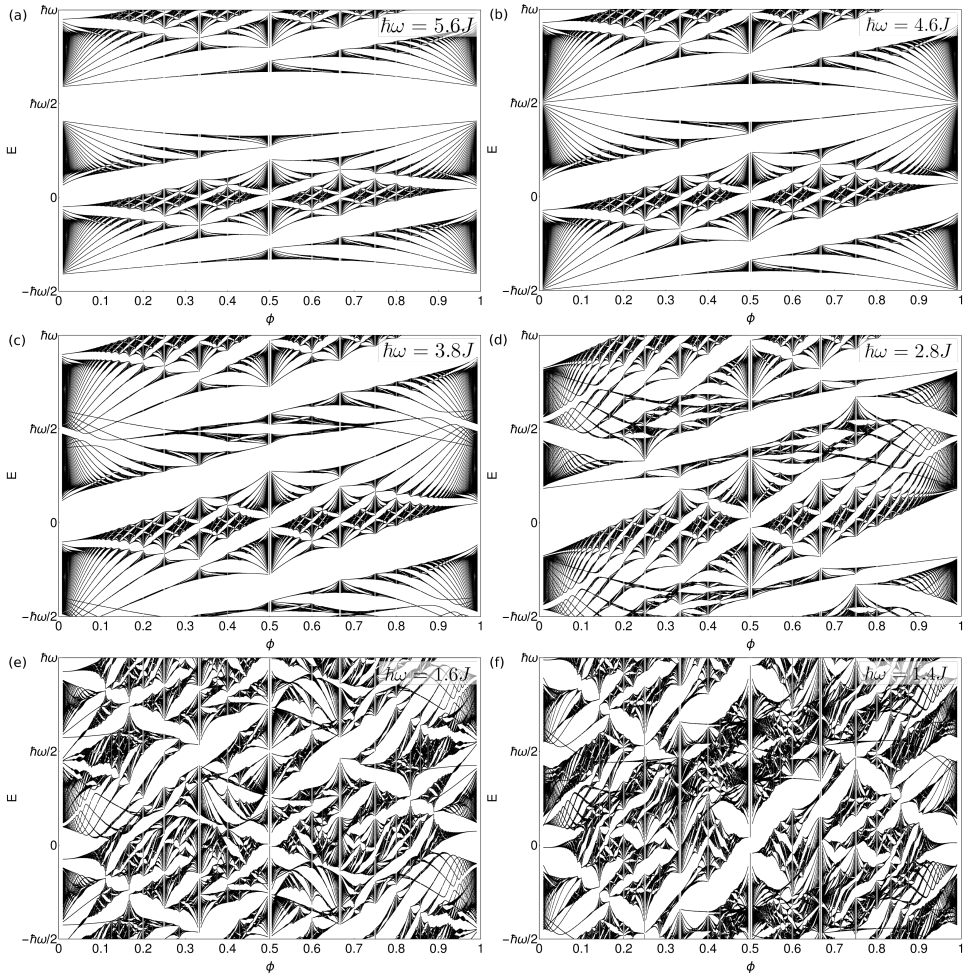

Figure 5.4: Full spectra plotted for various values of the frequency and $A_0 = 1$.

6 Conclusions

In this thesis, we have seen the effects of crystalline topology in a wide variety of contexts. We started with spinless systems, where this topology is completely determined by symmetry eigenvalues. With time-reversal symmetry, eigenvalues no longer reveal the full topology of the system, and in particular one cannot determine the corner charges from eigenvalues anymore. Here, we had to resort to different methods to identify the topological invariants that determine the corner charges.

In Chapter 2, we have proposed a way of realizing a higher-order topological insulator by layering a two-dimensional material such as graphene or silicene. If these layers are alternately p- and n-doped, and the construction respects inversion symmetry, applying a magnetic field drives the system into a higher-order topological insulating phase. This coupled layer construction provides both an intuitive model for the appearance of chiral hinge states, as well as a possible material platform to realize such phases.

In Chapter 3, two-dimensional systems with time-reversal and two-fold rotation symmetry were considered. With time-reversal symmetry, conventional symmetry indicators fail to classify all topological phases. We have presented a novel $\mathbb{Z}_2$ invariant, that together with the partial polarization is able to classify all atomic insulating phases. In addition, we have also identified additional novel fragile topological phases, both with two and four occupied bands.

In Chapter 4, we have examined the topological phases of quantum spin Hall systems with an additional two-fold rotation symmetry. We found that indeed the rotational symmetry provides an extra $\mathbb{Z}_2$ invariant, which we then exploited to construct a hybrid-order topological insulator. This insulator is both a weak and a second-order topological insulator, and features protected surface Dirac cones on all surfaces. The Dirac cones on the side surfaces are protected by translation and time-reversal symmetry, while the cones on the top and bottom surfaces are protected by $\mathcal{C}_2$ and time-reversal.

In Chapter 5, we have considered a honeycomb lattice subjected to a perpendicular magnetic field, and irradiated by circularly polarized light.

This system was studied using the Floquet formalism, where we can follow the hybridization of the Landau levels due to the polarized light.

We have only discussed a small number of space symmetry groups with time-reversal symmetry, especially in three-dimensions, and it would be interesting to explore the possible topological phases in other space groups. Another direction of research for the future would be to find an efficient way to check if materials realize the phases discussed in Chapters 3 and 4. This has recently been done taking into account only phases distinguishable by symmetry eigenvalues [86–88], and it would be interesting to extend this to find topological materials not diagnosable by symmetry eigenvalues.

Bibliography

[1] K. v. Klitzing, G. Dorda, and M. Pepper, Phys. Rev. Lett. **45**, 494 (1980).

[2] C. L. Kane and E. J. Mele, Phys. Rev. Lett. **95**, 226801 (2005).

[3] C. L. Kane and E. J. Mele, Phys. Rev. Lett. **95**, 146802 (2005).

[4] M. König, S. Wiedmann, C. Brüne, A. Roth, H. Buhmann, L. W. Molenkamp, X.-L. Qi, and S.-C. Zhang, Science **318**, 766 (2007).

[5] B. Bradlyn, L. Elcoro, J. Cano, M. G. Vergniory, Z. Wang, C. Felser, M. I. Aroyo, and B. A. Bernevig, Nature **547**, 298 (2017).

[6] H. C. Po, H. Watanabe, and A. Vishwanath, Phys. Rev. Lett. **121**, 126402 (2018).

[7] B. Bradlyn, Z. Wang, J. Cano, and B. A. Bernevig, Phys. Rev. B **99**, 045140 (2019).

[8] G. van Miert and C. Ortix, Phys. Rev. B **98**, 081110 (2018).

[9] F. Schindler, A. M. Cook, M. G. Vergniory, Z. Wang, S. S. Parkin, B. A. Bernevig, and T. Neupert, Sci. Adv. **4**, eaat0346 (2018).

[10] H. C. Po, A. Vishwanath, and H. Watanabe, Nature Communications **8**, 50 (2017).

[11] M. Z. Hasan and C. L. Kane, Rev. Mod. Phys. **82**, 3045 (2010).

[12] X.-L. Qi and S.-C. Zhang, Rev. Mod. Phys. **83**, 1057 (2011).

[13] L. Fu, Phys. Rev. Lett. **106**, 106802 (2011).

[14] T. H. Hsieh, H. Lin, J. Liu, W. Duan, A. Bansil, and L. Fu, Nat. Comm. **3**, 982 (2012).

[15] H. Nielsen and M. Ninomiya, Physics Letters B **105**, 219 (1981).

[16] C. Fang and L. Fu, Sci. Adv. **5**, eaat2374 (2019).

[17] W. A. Benalcazar, B. A. Bernevig, and T. L. Hughes, Science **357**, 61 (2017).

[18] W. A. Benalcazar, B. A. Bernevig, and T. L. Hughes, Phys. Rev. B **96**, 245115 (2017).

[19] F. Schindler, Z. Wang, M. G. Vergniory, A. M. Cook, A. Murani, S. Sengupta, A. Y. Kasumov, R. Deblock, S. Jeon, I. Drozdov, *et al.*, Nat. Phys. **14**, 918 (2018).

[20] M. Geier, L. Trifunovic, M. Hoskam, and P. W. Brouwer, Phys. Rev. B **97**, 205135 (2018).

[21] Y. Xu, R. Xue, and S. Wan, ArXiv e-prints (2017), arXiv:1711.09202 [cond-mat.str-el] .

[22] C. W. Peterson, W. A. Benalcazar, T. L. Hughes, and G. Bahl, Nature **555**, 346 (2018).

[23] M. Serra-Garcia, V. Peri, R. Süsstrunk, O. R. Bilal, T. Larsen, L. G. Villanueva, and S. D. Huber, Nature **555**, 342 (2018).

[24] S. Imhof, C. Berger, F. Bayer, J. Brehm, L. W. Molenkamp, T. Kiessling, F. Schindler, C. H. Lee, M. Greiter, T. Neupert, *et al.*, Nat. Phys. **14**, 925 (2018).

[25] E. Khalaf, Phys. Rev. B **97**, 205136 (2018).

[26] M. Ezawa, Phys. Rev. Lett. **120**, 026801 (2018).

[27] J. Langbehn, Y. Peng, L. Trifunovic, F. von Oppen, and P. W. Brouwer, Phys. Rev. Lett. **119**, 246401 (2017).

[28] M. Sitte, A. Rosch, E. Altman, and L. Fritz, Phys. Rev. Lett. **108**, 126807 (2012).

[29] Z. Song, Z. Fang, and C. Fang, Phys. Rev. Lett. **119**, 246402 (2017).

[30] M. Ezawa, Phys. Rev. B **97**, 155305 (2018).

[31] M. Ezawa, Phys. Rev. B **97**, 241402 (2018).

[32] A. Lau, K. Koepernik, J. van den Brink, and C. Ortix, Phys. Rev. Lett. **119**, 076801 (2017).

[33] A. C. Neto, F. Guinea, N. M. Peres, K. S. Novoselov, and A. K. Geim, Rev. Mod. Phys. **81**, 109 (2009).

[34] I. Fulga, N. Avraham, H. Beidenkopf, and A. Stern, Phys. Rev. B **94**, 125405 (2016).

[35] F. D. M. Haldane, Phys. Rev. Lett. **61**, 2015 (1988).

[36] D. R. Hofstadter, Phys. Rev. B **14**, 2239 (1976).

[37] B. A. Bernevig, T. L. Hughes, S. Raghu, and D. P. Arovas, Phys. Rev. Lett. **99**, 146804 (2007).

[38] J. C. Teo, L. Fu, and C. Kane, Phys. Rev. B **78**, 045426 (2008).

[39] M. Rice and E. Mele, Phys. Rev. Lett. **49**, 1455 (1982).

[40] D. Xiao, M.-C. Chang, and Q. Niu, Rev. Mod. Phys. **82**, 1959 (2010).

[41] L. Fu and C. L. Kane, Phys. Rev. B **76**, 045302 (2007).

[42] R. Jackiw and C. Rebbi, Phys. Rev. D **13**, 3398 (1976).

[43] L. Cano-Cortés, C. Ortix, and J. van den Brink, Phys. Rev. Lett. **111**, 146801 (2013).

[44] C. Kamal, A. Chakrabarti, A. Banerjee, and S. Deb, J. Phys.: Condens. Matter **25**, 085508 (2013).

[45] A. Rudenko, S. Yuan, and M. Katsnelson, Phys. Rev. B **92**, 085419 (2015).

[46] S. K. Das, B. Yan, J. van den Brink, and I. C. Fulga, Phys. Rev. B **99**, 165418 (2019).

[47] D. J. Thouless, M. Kohmoto, M. P. Nightingale, and M. den Nijs, Phys. Rev. Lett. **49**, 405 (1982).

[48] B. I. Halperin, Phys. Rev. B **25**, 2185 (1982).

[49] M. Kohmoto, Ann. Phys. (N.Y.) **160**, 343 (1985).

[50] B. A. Bernevig, T. L. Hughes, and S.-C. Zhang, Science **314**, 1757 (2006).

[51] H. Zhang, C.-X. Liu, X.-L. Qi, X. Dai, Z. Fang, and S.-C. Zhang, Nat. Phys. **5**, 438 (2009).

[52] C. Brüne, C. Liu, E. Novik, E. Hankiewicz, H. Buhmann, Y. Chen, X. Qi, Z. Shen, S. Zhang, and L. Molenkamp, Phys. Rev. Lett. **106**, 126803 (2011).

[53] B. Rasche, A. Isaeva, M. Ruck, S. Borisenko, V. Zabolotnyy, B. Büchner, K. Koepernik, C. Ortix, M. Richter, and J. Van Den Brink, Nat. Mat. **12**, 422 (2013).

[54] V. Mourik, K. Zuo, S. M. Frolov, S. Plissard, E. P. Bakkers, and L. P. Kouwenhoven, Science **336**, 1003 (2012).

[55] R. M. Lutchyn, J. D. Sau, and S. D. Sarma, Phys. Rev. Lett. **105**, 077001 (2010).

[56] L. Fu and C. L. Kane, Phys. Rev. Lett. **100**, 096407 (2008).

[57] C. Beenakker, Ann. Rev. Cond. Mat. Phys. **4**, 113 (2013).

[58] J. Alicea, Rep. Prog. in Phys. **75**, 076501 (2012).

[59] N. Armitage, E. Mele, and A. Vishwanath, Rev. Mod. Phys. **90**, 015001 (2018).

[60] S.-M. Huang, S.-Y. Xu, I. Belopolski, C.-C. Lee, G. Chang, B. Wang, N. Alidoust, G. Bian, M. Neupane, C. Zhang, *et al.*, Nat. Comm. **6**, 7373 (2015).

[61] B. Lv, H. Weng, B. Fu, X. Wang, H. Miao, J. Ma, P. Richard, X. Huang, L. Zhao, G. Chen, *et al.*, Phys. Rev. X **5**, 031013 (2015).

[62] S.-Y. Xu, I. Belopolski, N. Alidoust, M. Neupane, G. Bian, C. Zhang, R. Sankar, G. Chang, Z. Yuan, C.-C. Lee, *et al.*, Science **349**, 613 (2015).

[63] E. Haubold, K. Koepernik, D. Efremov, S. Khim, A. Fedorov, Y. Kushnirenko, J. van den Brink, S. Wurmehl, B. Büchner, T. Kim, *et al.*, Phys. Rev. B **95**, 241108 (2017).

[64] X. Wan, A. M. Turner, A. Vishwanath, and S. Y. Savrasov, Phys. Rev. B **83**, 205101 (2011).

[65] A. A. Burkov and L. Balents, Phys. Rev. Lett. **107**, 127205 (2011).

[66] A. A. Zyuzin, S. Wu, and A. A. Burkov, Phys. Rev. B **85**, 165110 (2012).

[67] A. Lau and C. Ortix, Phys. Rev. Lett. **122**, 186801 (2019).

[68] T. Ojanen, Phys. Rev. B **87**, 245112 (2013).

[69] A. A. Soluyanov, D. Gresch, Z. Wang, Q. Wu, M. Troyer, X. Dai, and B. A. Bernevig, Nature **527**, 495 (2015).

[70] A. Altland and M. R. Zirnbauer, Phys. Rev. B **55**, 1142 (1997).

[71] A. P. Schnyder, S. Ryu, A. Furusaki, and A. W. Ludwig, Phys. Rev. B **78**, 195125 (2008).

[72] A. Kitaev, in *AIP Conference Proceedings*, Vol. 1134 (AIP, 2009) pp. 22–30.

[73] J. Liu, T. H. Hsieh, P. Wei, W. Duan, J. Moodera, and L. Fu, Nat. Mat. **13**, 178 (2014).

[74] T. H. Hsieh, J. Liu, and L. Fu, Phys. Rev. B **90**, 081112 (2014).

[75] K. Shiozaki, M. Sato, and K. Gomi, arXiv preprint arXiv:1802.06694 (2018).

[76] W. A. Benalcazar, B. A. Bernevig, and T. L. Hughes, Physical Review B **96**, 245115 (2017).

[77] E. Khalaf, Phys. Rev. B **97**, 205136 (2018).

[78] M. Ezawa, Phys. Rev. B **97**, 155305 (2018).

[79] S. Imhof, C. Berger, F. Bayer, J. Brehm, L. W. Molenkamp, T. Kiessling, F. Schindler, C. H. Lee, M. Greiter, T. Neupert, *et al.*, Nat. Phys. **14**, 925 (2018).

[80] C.-H. Hsu, P. Stano, J. Klinovaja, and D. Loss, Phys. Rev. Lett. **121**, 196801 (2018).

[81] S. H. Kooi, G. Van Miert, and C. Ortix, Phys. Rev. B **98**, 245102 (2018).

[82] A. A. Soluyanov and D. Vanderbilt, Phys. Rev. B **83**, 035108 (2011).

[83] R. Yu, X. L. Qi, A. Bernevig, Z. Fang, and X. Dai, Phys. Rev. B **84**, 075119 (2011).

[84] J. Kruthoff, J. de Boer, J. van Wezel, C. L. Kane, and R.-J. Slager, Phys. Rev. X **7**, 041069 (2017).

[85] Z. Song, T. Zhang, Z. Fang, and C. Fang, Nat. Comm. **9**, 3530 (2018).

[86] T. Zhang, Y. Jiang, Z. Song, H. Huang, Y. He, Z. Fang, H. Weng, and C. Fang, Nature **566**, 475 (2019).

[87] M. Vergniory, L. Elcoro, C. Felser, N. Regnault, B. A. Bernevig, and Z. Wang, Nature **566**, 480 (2019).

[88] F. Tang, H. C. Po, A. Vishwanath, and X. Wan, Nature **566**, 486 (2019).

[89] Z. Song, L. Elcoro, N. Regnault, and B. A. Bernevig, arXiv e-prints , arXiv:1905.03262 (2019).

[90] B. J. Wieder and B. A. Bernevig, arXiv preprint arXiv:1810.02373 (2018).

[91] Y. Hwang, J. Ahn, and B.-J. Yang, arXiv preprint arXiv:1905.08128 (2019).

[92] Y. Cao, V. Fatemi, S. Fang, K. Watanabe, T. Taniguchi, E. Kaxiras, and P. Jarillo-Herrero, Nature **556**, 43 (2018).

[93] Y. Cao, V. Fatemi, A. Demir, S. Fang, S. L. Tomarken, J. Y. Luo, J. D. Sanchez-Yamagishi, K. Watanabe, T. Taniguchi, E. Kaxiras, *et al.*, Nature **556**, 80 (2018).

[94] J. Ahn, S. Park, and B.-J. Yang, Phys. Rev. X **9**, 021013 (2019).

[95] H. C. Po, L. Zou, T. Senthil, and A. Vishwanath, Phys. Rev. B **99**, 195455 (2019).

[96] A. Bouhon, A. M. Black-Schaffer, and R.-J. Slager, arXiv preprint arXiv:1804.09719 (2018).

[97] J. Zak, Phys. Rev. B **26**, 3010 (1982).

[98] A. Lau, J. van den Brink, and C. Ortix, Phys. Rev. B **94**, 165164 (2016).

[99] G. van Miert and C. Ortix, Phys. Rev. B **96**, 235130 (2017).

[100] L. Fu and C. L. Kane, Phys. Rev. B **74**, 195312 (2006).

[101] A. Alexandradinata, X. Dai, and B. A. Bernevig, Phys. Rev. B **89**, 155114 (2014).

[102] P. G. Harper, Proceedings of the Physical Society. Section A **68**, 874 (1955).

[103] S. Aubry and G. André, Ann. Isr. Phys. Soc. **3**, 133 (1980).

[104] S. Ganeshan, K. Sun, and S. Das Sarma, Phys. Rev. Lett. **110**, 180403 (2013).

[105] J. Kruthoff, J. de Boer, and J. van Wezel, arXiv e-prints , arXiv:1711.04769 (2017).

[106] G. van Miert and C. Ortix, Phys. Rev. B **97**, 201111 (2018).

[107] J. Cano, B. Bradlyn, Z. Wang, L. Elcoro, M. G. Vergniory, C. Felser, M. I. Aroyo, and B. A. Bernevig, Phys. Rev. Lett. **120**, 266401 (2018).

[108] T. Bzdušek and M. Sigrist, Phys. Rev. B **96**, 155105 (2017).

[109] J. Ahn, D. Kim, Y. Kim, and B.-J. Yang, Phys. Rev. Lett. **121**, 106403 (2018).

[110] S. Franca, J. van den Brink, and I. C. Fulga, Phys. Rev. B **98**, 201114 (2018).

[111] M. Eschbach, M. Lanius, C. Niu, E. Młyńczak, P. Gospodarič, J. Kellner, P. Schüffelgen, M. Gehlmann, S. Döring, E. Neumann, *et al.*, Nature Comm. **8**, 14976 (2017).

[112] N. Avraham, A. Norris, Y. Sun, Y. Qi, L. Pan, A. Isaeva, A. Zeugner, C. Felser, B. Yan, and H. Beidenkopf, arXiv:1708.09062 (2017).

[113] I. Rusinov, T. Menshchikova, A. Isaeva, S. Eremeev, Y. M. Koroteev, M. Vergniory, P. Echenique, and E. V. Chulkov, Sci. Rep. **6**, 20734 (2016).

[114] J. I. Facio, S. K. Das, Y. Zhang, K. Koepernik, J. van den Brink, and I. C. Fulga, Phys. Rev. Materials **3**, 074202 (2019).

[115] N. Bultinck, B. A. Bernevig, and M. P. Zaletel, Phys. Rev. B **99**, 125149 (2019).

[116] S. A. A. Ghorashi, X. Hu, T. L. Hughes, and E. Rossi, Phys. Rev. B **100**, 020509 (2019).

[117] S. A. A. Ghorashi, T. L. Hughes, and E. Rossi, arXiv preprint arXiv:1909.10536 (2019).

[118] Z. Song, L. Elcoro, N. Regnault, and B. A. Bernevig, arXiv e-prints , arXiv:1905.03262 (2019).

[119] S. H. Kooi, G. van Miert, and C. Ortix, Phys. Rev. B **100**, 115160 (2019).

[120] L. Fu and C. L. Kane, Phys. Rev. B **76**, 045302 (2007).

[121] J. Kruthoff, J. de Boer, and J. van Wezel, Phys. Rev. B **100**, 075116 (2019).

[122] L. Fidkowski, T. Jackson, and I. Klich, Phys. Rev. Lett. **107**, 036601 (2011).

[123] C.-H. Hsu, X. Zhou, Q. Ma, N. Gedik, A. Bansil, V. M. Pereira, H. Lin, L. Fu, S.-Y. Xu, and T.-R. Chang, 2D Mat. **6**, 031004 (2019).

[124] T. Zhang, C. Yue, T. Zhang, S. Nie, Z. Wang, C. Fang, H. Weng, and Z. Fang, Phys. Rev. Research **1**, 012001 (2019).

[125] A. Lau, C. Ortix, and J. van den Brink, Phys. Rev. B **91**, 085106 (2015).

[126] T. L. Hughes, E. Prodan, and B. A. Bernevig, Physical Review B **83**, 245132 (2011).

[127] D. R. Hofstadter, Phys. Rev. B **14**, 2239 (1976).

[128] M. Yankowitz, J. Xue, D. Cormode, J. D. Sanchez-Yamagishi, K. Watanabe, T. Taniguchi, P. Jarillo-Herrero, P. Jacquod, and B. J. LeRoy, Nature Phys. **8**, 382 (2012).

[129] J. Xue, J. Sanchez-Yamagishi, D. Bulmash, P. Jacquod, A. Deshpande, K. Watanabe, T. Taniguchi, P. Jarillo-Herrero, and B. J. LeRoy, Nature Mater. **10**, 282 (2011).

[130] L. Ponomarenko, R. Gorbachev, G. Yu, D. Elias, R. Jalil, A. Patel, A. Mishchenko, A. Mayorov, C. Woods, J. Wallbank, *et al.*, Nature **497**, 594 (2013).

[131] C. Dean, L. Wang, P. Maher, C. Forsythe, F. Ghahari, Y. Gao, J. Katoch, M. Ishigami, P. Moon, M. Koshino, *et al.*, Nature **497**, 598 (2013).

[132] M. Hafezi, E. A. Demler, M. D. Lukin, and J. M. Taylor, Nature Phys. **7**, 907 (2011).

[133] D. Jaksch and P. Zoller, New J. Phys. **5**, 56 (2003).

[134] J. Dalibard, F. Gerbier, G. Juzeliūnas, and P. Öhberg, Rev. Mod. Phys. **83**, 1523 (2011).

[135] N. Goldman, G. Juzeliūnas, P. Öhberg, and I. B. Spielman, Rep. Prog. Phys. **77**, 126401 (2014).

[136] H. Miyake, G. A. Siviloglou, C. J. Kennedy, W. C. Burton, and W. Ketterle, Phys. Rev. Lett. **111**, 185302 (2013).

[137] M. Aidelsburger, M. Atala, M. Lohse, J. T. Barreiro, B. Paredes, and I. Bloch, Phys. Rev. Lett. **111**, 185301 (2013).

[138] A. Eckardt, Rev. Mod. Phys. **89**, 011004 (2017).

[139] P. Titum, E. Berg, M. S. Rudner, G. Refael, and N. H. Lindner, Phys. Rev. X **6**, 021013 (2016).

[140] N. H. Lindner, G. Refael, and V. Galitski, Nature Phys. **7**, 490 (2011).

[141] W. Zheng and H. Zhai, Phys. Rev. A **89**, 061603 (2014).

[142] A. Quelle and C. Morais Smith, Phys. Rev. B **90**, 195137 (2014).

[143] P. Delplace, Á. Gómez-León, and G. Platero, Phys. Rev. B **88**, 245422 (2013).

[144] S. Koghee, L.-K. Lim, M. Goerbig, and C. Morais Smith, Phys. Rev. A **85**, 023637 (2012).

[145] M. Benito, A. Gómez-León, V. Bastidas, T. Brandes, and G. Platero, Phys. Rev. B **90**, 205127 (2014).

[146] M. C. Rechtsman, J. M. Zeuner, Y. Plotnik, Y. Lumer, D. Podolsky, F. Dreisow, S. Nolte, M. Segev, and A. Szameit, Nature **496**, 196 (2013).

[147] Y. Wang, H. Steinberg, P. Jarillo-Herrero, and N. Gedik, Science **342**, 453 (2013).

[148] N. Fläschner, B. Rem, M. Tarnowski, D. Vogel, D.-S. Lühmann, K. Sengstock, and C. Weitenberg, Science **352**, 1091 (2016).

[149] J. Wang and J. Gong, Phys. Rev. A **77**, 031405 (2008).

[150] D. Y. Ho and J. Gong, Phys. Rev. B **90**, 195419 (2014).

[151] M. Lababidi, I. I. Satija, and E. Zhao, Phys. Rev. Lett. **112**, 026805 (2014).

[152] Z. Zhou, I. I. Satija, and E. Zhao, Phys. Rev. B **90**, 205108 (2014).

[153] K.-H. Ding, L.-K. Lim, G. Su, and Z.-Y. Weng, Phys. Rev. B **97**, 035123 (2018).

[154] N. Goldman, J. Dalibard, M. Aidelsburger, and N. Cooper, Phys. Rev. A **91**, 033632 (2015).

[155] A. Gómez-León and G. Platero, Phys. Rev. Lett. **110**, 200403 (2013).

[156] G. Jotzu, M. Messer, R. Desbuquois, M. Lebrat, T. Uehlinger, D. Greif, and T. Esslinger, Nature **515**, 237 (2014).

[157] T. Mikami, S. Kitamura, K. Yasuda, N. Tsuji, T. Oka, and H. Aoki, Phys. Rev. B **93**, 144307 (2016).

[158] M. S. Rudner, N. H. Lindner, E. Berg, and M. Levin, Phys. Rev. X **3**, 031005 (2013).

[159] T. Kitagawa, E. Berg, M. Rudner, and E. Demler, Phys. Rev. B **82**, 235114 (2010).

[160] F. Nathan and M. S. Rudner, New J. Phys. **17**, 125014 (2015).

[161] A. Quelle, M. Goerbig, and C. Morais Smith, New J. Phys. **18**, 015006 (2016).

[162] M. Wackerl and J. Schliemann, arXiv:1802.01369 .

[163] T. Grozdanov and M. Raković, Phys. Rev. A **38**, 1739 (1988).

[164] A. López, A. Scholz, B. Santos, and J. Schliemann, Phys. Rev. B **91**, 125105 (2015).

[165] A. Eckardt and E. Anisimovas, New J. Phys. **17**, 093039 (2015).

[166] S. Rahav, I. Gilary, and S. Fishman, Phys. Rev. A **68**, 013820 (2003).

[167] P. Streda, J. Phys. C **15**, L717 (1982).

[168] T. Fukui, Y. Hatsugai, and H. Suzuki, J. Phys. Soc. Jpn. **74**, 1674 (2005).

[169] F. D. M. Haldane, Phys. Rev. Lett. **61**, 2015 (1988).

[170] T. Oka and H. Aoki, Phys. Rev. B **79**, 081406 (2009).

[171] T. Kitagawa, T. Oka, A. Brataas, L. Fu, and E. Demler, Phys. Rev. B **84**, 235108 (2011).

[172] W. Beugeling, N. Goldman, and C. Morais Smith, Phys. Rev. B **86**, 075118 (2012).

[173] I. Dana, Y. Avron, and J. Zak, J. Phys. C **18**, L679 (1985).

[174] E. Kalesaki, C. Delerue, C. Morais Smith, W. Beugeling, G. Allan, and D. Vanmaekelbergh, Phys. Rev. X **4**, 011010 (2014).

[175] W. Beugeling, E. Kalesaki, C. Delerue, Y.-M. Niquet, D. Vanmaekelbergh, and C. Morais Smith, Nature Commun. **6**, 6316 (2015).

[176] P. Soltan-Panahi, J. Struck, P. Hauke, A. Bick, W. Plenkers, G. Meineke, C. Becker, P. Windpassinger, M. Lewenstein, and K. Sengstock, Nature Phys. **7**, 434 (2011).

[177] N. Goldman, J. Budich, and P. Zoller, Nature Phys. **12**, 639 (2016).

[178] A. Quelle, C. Weitenberg, K. Sengstock, and C. Morais Smith, New J. Phys. **19**, 113010 (2017).

[179] A. Pfeuffer-Jeschke, Ph.D. thesis (2000), Würzburg University.

[180] E. G. Novik, A. Pfeuffer-Jeschke, T. Jungwirth, V. Latussek, C. R. Becker, G. Landwehr, H. Buhmann, and L. W. Molenkamp, Phys. Rev. B **72**, 035321 (2005).

Samenvatting

Dit proefschrift gaat voornamelijk over isolerende kristallen. Kristallen zijn materialen waar de atomen in een regelmatig patroon gerangschikt zijn, waaromheen zich elektronen bevinden, en in een isolator bevinden de elektronen zich in een configuratie waarin er geen elektrische geleiding kan plaatsvinden. Dit is bijvoorbeeld het geval als de elektronen zeer sterk zijn gebonden aan de atomen.

Het lijkt op het eerste gezicht niet zo interessant om de elektronische eigenschappen van deze materialen te bestuderen, aangezien er geen elektrische geleiding mogelijk is. Er bestaat echter een speciale klasse isolatoren, genaamd topologische isolatoren. Deze materialen zijn isolerend in het interieur van het materiaal, maar geleiden wel op de rand.

De eerste topologische isolator werd in 1980 ontdekt door Klaus von Klitzing [1]. Hij bekeek een zeer dunne halfgeleider, en plaatste dit in een sterk magnetisch veld. Hierdoor werd het materiaal isolerend, maar zijn experiment liet zien dat er wel geleiding aan de rand van het materiaal mogelijk was. Dit is een zogenaamde kwantum Hall isolator, waar opmerkelijk genoeg de geleiding maar één kant op mogelijk is (zie Figuur 1).

Deze geleidende randtoestanden zijn niet slechts een randeffect. Dat wil zeggen dat een topologische isolator anders is dan een isolator waar een geleidend materiaal op de rand is geplakt, zoals het geval is bij een plastic dobbelsteen ingepakt in aluminiumfolie. Zou men deze dobbelsteen doormidden snijden, dan zijn niet meer alle oppervlakken geleidend. Bij een topologische isolator zit dat anders; zou men deze in tweeën splitsen dan ontstaan op elke rand weer geleidende toestanden (zie Figuur 1).

De reden dat dit een topologische isolator wordt genoemd, is dat de randtoestanden niet kunnen verdwijnen door kleine vervormingen. Topologie is een wiskundige discipline die zich bezig houdt met eigenschappen die onveranderd blijven door zulke kleine vervormingen, en men kan laten zien dat het systeem een kwantum Hall isolator blijft zolang men geen kleine vervorming introduceert die het systeem geleidend maken. Dat wil zeggen dat de precieze vorm van het materiaal, de exacte sterkte van het magneetveld,

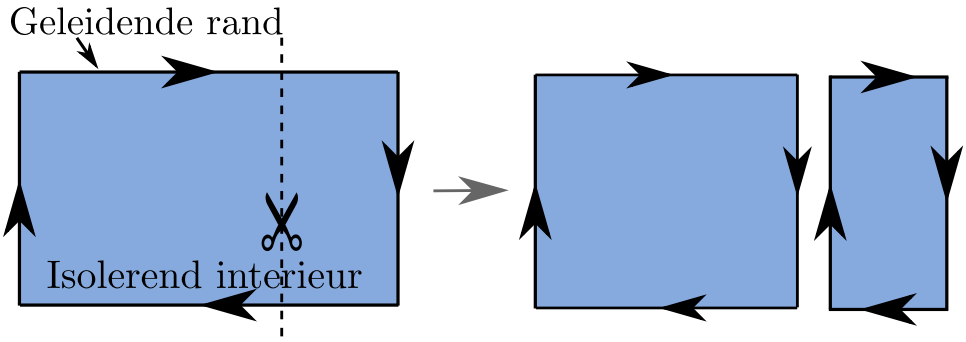

Figure 1: Schematische weergave van een kwantum Hall isolator. Het interieur is een isolator, maar op de rand zit een geleidende toestand. Zou men het materiaal in tweeën knippen, dan ontstaan twee verschillende stukjes materiaal die allebei weer geleidende randtoestanden hebben.

of een deukje hier en daar niet uitmaken.

In deze doctoraalscriptie worden vooral kristallijne (topologische) isolatoren beschouwd, en specifieker isolatoren die beschermd worden door een rotatiesymmetrie. De atomen van deze materialen vormen een rooster dat twee-, drie-, vier- of zesvoudige rotatiesymmetrie heeft (zie Figuur 2). Als deze symmetrie gebroken wordt, zijn eventuele geleidende randtoestanden niet langer beschermd. Naast geleidende randtoestanden kan rotatiesymmetrie ook nog iets anders beschermen: een gekwantiseerde hoeklading. De totale lading in de rode gebieden in Figuur 2 moet door de symmetrie een geheel getal zijn. Ook de waarde van de hoeklading is geen randeffect, en kan worden voorspeld als men weet in welke configuratie het interieur van het kristal zich bevind.

Dit is een gevolg van de interieur-rand correspondentie, die stelt dat de aanwezigheid van beschermde toestanden op de rand, en de waarde van de hoeklading kan worden gerelateerd aan de configuratie waarin het interieur zich bevind. Een belangrijke vraag, die we in dit proefschrift voor bepaalde gevallen beantwoorden, is hoe het bestaan van beschermde randtoestanden of hoeklading kan worden afgeleid uit het interieur van het systeem.

In hoofdstuk 2 beschrijven we een manier om een hogere orde topologische isolator te realiseren, beschermd door inversiesymmetrie. Dit is een driedimensionale isolator waarbij het interieur en de oppervlakten isolerend zijn, maar er wel geleiding kan plaatsvinden langs de ribben van het materiaal.

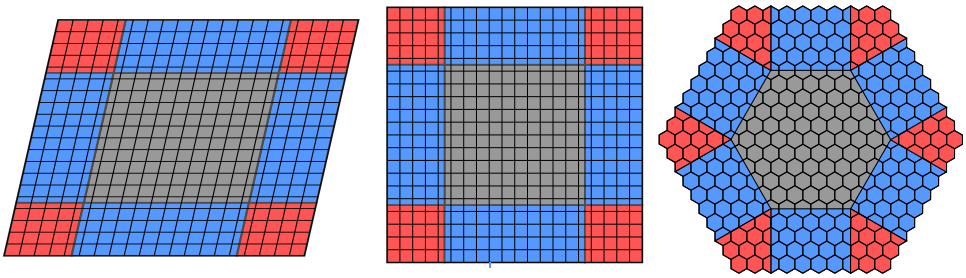

Figure 2: Schematische weergave van drie kristallen met van links naar rechts tweevoudige, viervoudige en zesvoudige rotatiesymmetrie. De hoekgebieden zijn rood gekleurd. De lading in deze gebiden is gekwantiseerd en beschermd door de rotatiesymmetrie.

Onze constructie bestaat uit het op elkaar stapelen van verschillende lagen grafeen, een tweedimensionaal materiaal bestaande uit koolstofatomen in een honingraat rooster. Deze lagen grafeen worden om en om p- danwel n-gedoopt, en vervolgens wordt er een magnetisch veld aangezet. Op deze manier ontstaan er geleidende toestanden op de ribben van het materiaal, beschermd door inversie symmetrie. Deze constructie is een concrete manier om een hogere orde topologische isolator te realiseren.

In hoofdstuk 3 beschouwen we tweedimensionale kristallen met tweevoudige rotatiesymmetrie en tijdomkeersymmetrie. We ontwikkelen een methode om alle topologisch verschillende isolatoren te onderscheiden met deze symmetrieën. Bestaande methodes om deze verschillende fases te onderscheiden, gebaseerd op eigenwaardes, zijn hier niet toereikend. In plaats hiervan beschouwen we de genestelde partiële polarisatie van het Wilson loop spectrum. Verder identificeren we een nieuwe fragiele topologische isolator.

In hoofdstuk 4 laten we zien dat tweevoudige rotatiesymmetrie en tijdomkeer symmetrie een hybride-orde topologische isolator kunnen beschermen. In deze driedimensionale topologische isolator zijn alle oppervlakken geleidend, maar niet door dezelfde symmetrieën beschermd. Verder laten we zien dat deze topologische isolator niet met bestaande methodes kan worden gedetecteerd, en geven we een formulering voor de topologische invariant die deze fase beschermt.

In hoofdstuk 5 beschouwen we grafeen in een sterk magneetveld, waar circulair gepolariseerd licht op wordt geschenen. Dit systeem wordt bestudeerd

met het zogenaamde Floquet formalisme. Hiermee wordt het energiespectrum van het systeem berekend voor verschillende sterktes en frequenties van het circulair gepolariseerde licht.

In de toekomst zou het interessant zijn om de methodes om verschillende isolatoren te onderscheiden, zoals beschreven in de hoofdstukken 3 en 4, toe te passen op de data van een groot aantal materialen. Op deze manier kan worden bekeken of er materialen zijn die op een natuurlijke manier de fases die hier beschreven zijn realiseren. Dit is recentelijk gedaan met methodes gebaseerd op symmetrie eigenwaardes [86–88], maar deze zijn niet in staat om bijvoorbeeld de fragiele topologische isolator uit hoofdstuk 3 of de hybride-orde topologische isolator uit hoofdstuk 4 te detecteren.

Dankwoord

Een proefschrift komt niet zonder slag of stoot tot stand, en voor het feit dat de lezer er toch eentje vasthoud ben ik dank verschuldigd aan een aantal mensen.

Allereerst wil ik Cristiane bedanken voor haar hulp in het verkrijgen van deze PhD positie. Carmine wil ik bedanken voor de kans om samen aan deze projecten te werken, en voor de vele inhoudelijke discussies, waarvoor ik altijd binnen kon lopen. Deze hielpen mij immer verder als ik vast zat. Guido wil ik bedanken voor zijn geduld in het uitleggen van talloze natuurkundige concepten, voor onze lange discussies over natuurkunde (en andere zaken), en voor het mij altijd weer motiveren om dingen nog beter te begrijpen. Rembert wil ik bedanken voor zijn rol als mijn independent counselor.

Daarnaast wil ik alle collega's bij het ITF bedanken voor de lunches, seminars en discussies, in het bijzonder Rafaelle, Niccolo, Camilo, Erik, Nick, Etienne, Jurriaan en Benedikt, en mijn kantoorgenoten Tycho en Gerwin. Ruward en Sander bedank ik voor de vele discussies over wetenschap en het PhD leven, en voor het zijn van mijn paranymfen.

Ook bedank ik graag Arja en Leo voor hun steun en betrokkenheid. Roelien en Willem bedank ik voor alle kansen die ze mij geboden hebben en voor het feit dat ze mij al 28 jaar in alles steunen. Tot slot bedank ik Nikki voor haar eindeloze geduld, het meedenken, en voor het feit dat ze er altijd voor mij is.

Over de auteur

Sander Hein Kooi is geboren op 10 maart 1992 te Groningen. In 2010 behaalde hij zijn vwo diploma aan het Zernike college in Haren. Hierna is hij natuur- en sterrenkunde gaan studeren in Utrecht waar hij in 2014 de bachelor afrondde. In deze periode studeerde hij tevens een semester in Berlijn en volgde het Decartes College. In 2016 rondde hij de master Theoretical Physics aan de Universiteit Utrecht *cum laude* af. In ditzelfde jaar is hij begonnen als PhD student aan de Universiteit Utrecht, onder begeleiding van prof. dr. C. de Morais Smith and prof. C. Ortix.